Title

Isomer Population Control in Solid-Density Targets using Compact Laser-Plasma Accelerators

Author

Jacob, Robert Edward

Publication Date

2024

Peer reviewed|Thesis/dissertation

Isomer Population Control in Solid-Density Targets using Compact Laser-Plasma Accelerators

By

Robert Edward Jacob

A dissertation submitted in partial satisfaction of the

requirements for the degree of

Doctor of Philosophy

in

Engineering-Nuclear Engineering

in the

Graduate Division

of the

University of California, Berkeley

Committee in charge:

Professor Carl Schroeder, Co-chair
Professor Lee Bernstein, Co-chair
Professor David Attwood

Spring 2024

Isomer Population Control in Solid-Density Targets using Compact Laser-Plasma Accelerators

Abstract

Isomer Population Control in Solid-Density Targets using Compact Laser-Plasma Accelerators

By

Robert Edward Jacob

Doctor of Philosophy in Engineering-Nuclear Engineering

University of California, Berkeley

Professor Carl Schroeder, Co-chair

Professor Lee Bernstein, Co-chair

Nuclear isomers impact a broad range of scientific and technical fields, from radio-medicine to stellar nucleosynthesis. Direct manipulation of isomer populations can enable a powerful new technique for mitigating spent-nuclear fuel, as well as enable new approaches to nuclear batteries. This work introduces a novel technique for the direct manipulation of isomer populations utilizing the enhanced nuclear level density (NLD) at high excitation energies, known as the nuclear quasicontinuum. Following excitation into the quasicontinuum, additional coupling of spin can occur through real or virtual photon transfer mediated by nuclear-plasma interactions (NPIs). Laser-plasma accelerators (LPAs) provide energetic, ultra-short pulse electron beams. This work discusses an experimental proof-of-concept study of manipulating isomer populations in Bromine nuclei using LPA-sourced < 100 fs electron beams. A comparison of bremsstrahlung photon and electron irradiation cases is evaluated to determine the presence of electron-nuclear interaction contributions to isomer populations. Additionally, the potential for LPAs to be used as sensitive probes of NLD models and photon strength functions in an effort to characterize the nuclear quasicontinuum is explored.

Contents

Contents **i**

List of Figures **iii**

List of Tables **vi**

1 Introduction **1**
1.1 Driving interests in understanding isomer population manipulation 1
1.2 Physical sources of long isomer lifetimes 2
1.3 Manipulation of isomer populations 4
1.3.1 Efforts in photon driven excitation of isomer states 5
1.3.2 Indirect population of isomer states 6
1.4 The need for new methods of isomer population manipulation 6

2 The Nuclear Quasicontinuum and Nuclear-Plasma Interactions **8**
2.1 Characterizing non-discrete nuclear states at high excitation energies 8
2.2 Nuclear level density models 10
2.2.1 Fermi gas Model 11
2.2.1.1 Defining the level density parameter and spin distribution width 12
2.2.2 Constant Temperature Model 13
2.2.3 Back-shifted Fermi gas Model 14
2.2.4 Generalized Superfluid Model 15
2.2.5 Microscopic level density models 16
2.3 Gamma strength functions 16
2.3.1 Lorentzian models for gamma strength functions 18
2.3.1.1 Double and Pygmy resonances 19
2.3.2 Microscopic models for gamma strength functions 19
2.4 Nuclear-Plasma Interactions 20
2.4.1 Nuclear excitation by electronic transition 20
2.4.2 Nuclear excitation by electron capture 21
2.4.3 Inelastic electron scattering 22

2.4.4 Photo-excitation by Bremsstrahlung . . . 22
2.4.5 Modifications to isomer lifetime in plasmas . . . 23
2.5 Coupling nuclear-plasma interactions into the quasicontinuum . . . 24

3 Lasers, plasma, and laser-plasma accelerators 25
3.1 Gaussian laser pulse . . . 25
3.2 Plasma fundamentals . . . 29
3.2.1 Modelling plasma behavior . . . 30
3.2.2 Electromagnetic waves in a plasma . . . 33
3.2.3 Intense laser pulses in plasma . . . 33
3.3 Laser-plasma accelerators . . . 34
3.3.1 Linear plasma waves . . . 34
3.3.2 Non-linear plasma waves . . . 37
3.4 Hundred-Terawatt Thomson laser platform . . . 41

4 Isomer population in Bromine nuclei 48
4.1 Experimental motivation . . . 48
4.2 Experimental design . . . 48
4.3 Experimental analysis . . . 53
4.3.1 Identification of isomer signals . . . 53
4.3.2 Calculation of populated nuclei . . . 55
4.3.3 TALYS calculations for photo-excitation . . . 57
4.3.4 Comparison of electron and photon irradiation cases . . . 59
4.4 Discussion . . . 61

Conclusion 65

Bibliography 65

List of Figures

1.1 Schematic for decay of ^{242}Am into ^{238}Pu with half-lives indicated [6]. Here, $\beta-$ refers to beta decay, α refers to alpha decay, and EC refers to the electron capture decay process. 2
1.2 Level scheme of ^{242}Am nucleus near the ground state, with the red arrows indicating excitation out of the ^{242m}Am state into the next available state at 52.7 keV [6]. 5

2.1 Schematic abbreviated level scheme for ^{242}Am, showing the ^{242m}Am isomer excited into the quasicontinuum, followed by decay into the ground state [6]. 10

3.1 Gaussian electric field radial dependence plotted at multiple z for w_0 =20 μm and λ=800 nm. 26
3.2 Intensity distribution resulting from a Gaussian electric field radial dependence plotted at multiple z for w_0 =20 μm and λ=800 nm. 27
3.3 Electric field envelope plotted against the carrier frequency oscillations for a Gaussian laser pulse with $\omega_0 = 2.36$ rad/fs and $\Delta t_{FWHM} = 40$ fs. 28
3.4 Linear plasma wave behavior plotted as function of the co-moving variable $k_{pe}\xi$ for $a_0 = 0.5$, with E_z/E_0, δn, and a^2 shown. 40
3.5 Quasi-linear plasma wave behavior plotted as function of the co-moving variable $k_{pe}\xi$ for $a_0 = 1.0$, with E_z/E_0, δn, and a^2 shown. 40
3.6 Non-linear plasma wave behavior plotted as function of the co-moving variable $k_{pe}\xi$ for $a_0 = 2.0$, with E_z/E_0, δn, and a^2 shown. 41
3.7 Overhead generalized description of the HTT laser system. Laser seeding and amplification occur in the room on the right side of image, with the target chamber on the left. 42
3.8 Schematic description of the HTT laser amplifier chain. Detailed are the three independent laser arms, with adjustable on-target arrival times. The listed current/future components were accurate at the time of the experiment, but are not representative of the system at the time of publication. 43
3.9 Histogram of 2500+ successive shots measuring the amplified drive laser energy. 44
3.10 Scan data showing the laser profile near focus, with representative CCD images shown at the top. The beam at focus is 20 μm, for a calculated intensity of $\approx 10^{19}$ W/cm^2. 45

3.11 Scan data showing the laser temporal FWHM as a function of compressor grating spacing, with representative FROG traces at the top. For both instruments, a FWHM pulse duration of 40 fs is measured, with an offset indicative of measurement geometry. 46
3.12 Long-term consecutive LPA electron beam spectrum data showing consistency over 1000 shots at 1 Hz. 47

4.1 Abbreviated nuclear level scheme for ^{79}Br, with lifetimes, energies, and spin states given. The solid blue arrow represents a direction photo-excitation from the ground state into the isomer, while the dashed red arrows represent excitation into the quasicontinuum followed by de-excitation into the isomer state [14]. . . 49
4.2 Schematic representation of the photon irradiation experimental configuration. The laser, shown in red, is focused in the gas jet, driving the LPA. The resulting electron beam, blue, co-propagates towards the magnet assembly. The 0.46 T dispersion magnet allows for geometric selection of the bremsstrahlung energy endpoints, while the 0.75 T secondary magnet bends the remaining electrons away from the detector, into a plastic shield not pictured. The LANEX screen located between the magnets is removable, providing a diagnostic tool for the electron beam energy. 51
4.3 Schematic representation of the electron irradiation experimental configuration. The laser, red, is focused in the gas jet, driving the LPA. The resulting electron beam, blue, co-propagates towards the magnet assembly. The 0.46 T dispersion magnet allows for geometric selection of the electron energies which strike the target. The LANEX screen located downstream of the dispersion magnet is removable, providing a diagnostic tool for the electron beam energy. 52
4.4 Electron energy spectrum showing the measured electron spectrum. The inset plot is an example CCD image with the center-line energy axis provided. As the screen was placed at 40° angle relative to the laser axis, the energy distribution across the image is warped and requires complex analysis. This angle offset is the cause of the diagonal shadow of the bremsstrahlung converter bar. 53
4.5 Shot-accumulated 2D histogram for the 20 seconds following each shot. The ^{79m}Br decay signal can be seen at 207.6 keV, which can be seen to decay away over the 20 second counting period. The ^{80m}Br decay signal can be seen as a constant background near 85.8 keV, as result of the significantly longer half-life. Note the curved detector response following rapid biasing after each shot. 54
4.6 Post-irradiation continuous 2D histogram for many hours. The ^{80m}Br decay signal can be seen near 85.8 keV, which can be seen to decay away with the characteristic 4.42 hour half-life. 54

4.7 Example process for the calculation of total isomer population N_0. The left plot shows the time-selection from the 2D histogram to generate the y-axis projection shown in the top right. The isomer signal peak for ^{79m}Br is circled in red, and magnified on the bottom right. The number of beige-green bins, m, is iterated through to calculate the peak counts, light blue, above the background signal, orange. In Equation 4.1 the total bin value is referred to as C_i and the background signal is BG_i. 56
4.8 Grid of TALYS default NLDs and γSFs used to calculate isomer activation ratios for the photo-excitation case using the stainless steel bremsstrahlung converter. 58
4.9 Shifted $\rho(E, J)$ distributions at 30 MeV in ^{79}Br. 59
4.10 Simulated spectra at the $LaBr_3$ active target comparing the internally generated bremsstrahlung from the electron beam, bremsstrahlung from the stainless steel bar, and the internal electron scattering spectrum. All calculated with FLUKA for an electron beam centered at 35 MeV with a flat width of 2 MeV. 60
4.11 Simulated electron energy deposition for an electron beam centered at 35 MeV with a flat width of 2 MeV in the $LaBr_3$ active target. Color bar calibrated for eV/Br atom/pC of electron beam charge. 61

List of Tables

4.1 Activations/Shot for isomer decay peaks 57

Acknowledgments

I'd like to thank my advisor Dr. Carl Schroeder for his invaluable guidance and mentorship during the course of my graduate degree. Our discussions, both technical and non-technical, are always appreciated. Your enthusiasm for our work is infectious and helped me to grow my own love for science, but you also made sure to remind me of the importance of maintaining a healthy work-life balance. Despite being totally unaware of the awesome field of laser-plasma accelerators beforehand, you gave me an opportunity to join the BELLA center. I will be forever grateful for that opportunity, as my experience at Berkeley has been transformative for me as a student, a scientist, and as an individual.

Thank you to my advisor Dr. Lee Bernstein for giving me the opportunity to work on such an intellectually stimulating project in exploring nuclear physics with laser-plasma accelerators. Working together on this project instilled in me a deep fascination with applied nuclear physics, and I look forward eagerly to the work that lies ahead. Your technical expertise, general insight, and endless optimism are greatly appreciated, always providing motivation to keep pushing forward.

Many thanks to the staff of the BELLA Center, with which I've had the honor of working closely with. Thank you to Dr. Cameron Geddes for your mentorship, and for motivating an attitude of excellence in the laboratory. Thank you to Dr. Jeroen van Tilborg, your passion for experiments and knowledge of laser systems is inspiring. Thank you to Dr. Qiang Chen and Dr. Benjamin Greenwood for sharing your depth of knowledge and experience with me, and for making HTT a great place to do science. Thank you to Zak Eisentraut, Mark Kirkpatrick, and the BELLA engineering team for sharing your technical expertise, insight, and making good science possible.

A special thank you to Dr. Tobias Ostermayr and Dr. Hai-En Tsai for their mentorship early in my graduate career. By sharing your knowledge, experience, and wisdom, you prepared me for the difficulties of experimental science. Your determination and resolve in approaching complex problems is inspirational, and I strive to emulate that in my future endeavors. I fondly remember the long days in the lab we shared during experimental campaigns, where I learned the value of appreciating the brief moments of success following many hours of hard work.

Thank you to my dissertation and qualifications committees for their efforts in shepherding me through the graduate school process. The successful completion of this dissertation is due in part to your guidance, patience, and expertise.

Thank you to the MANE Department at Rensselaer Polytechnic Institute for providing me a strong undergraduate education. Thank you to Dr. Yaron Danon for convincing me to pursue a doctorate. I was initially quite hesitant due to the commitment, but I am very glad I took your advice.

Thank you to all of the friends who supported me along the way, for the laughs and for lending an ear when needed. Thank you Griffin Melnick, for sticking with me for the long haul. Across 9 years, from Troy, NY to the SF Bay Area, you've been a constant in my life and I am grateful for you friendship. Thank you to Curtis Berger and Kyle Jensen,

for making graduate school all the more enjoyable. Whether it be discussing experiments, science, our cats, playing games, struggling at the driving range, or anything else, I look forward to more time in your company.

Thank you to my parents Virginia and Karl, who both worked very hard to provide me the opportunities that led here. I couldn't have done it without your support, and I love you both. Thank you to my brother John, for your support and for being a great friend.

And finally, I must express my immeasurable love and gratitude for my fiancée Nicole, who has supported me throughout this entire journey. You've helped me navigate the most difficult times, and helped me celebrate the happiest moments. Your patience with me during this entire process is recognized and greatly appreciated. And now, I look forward with giddy anticipation to life with you and our feline boys, Pascal and Charles. Together, we can handle whatever comes our way.

The author gratefully acknowledges fruitful discussions with Ross Koningstein. This work was supported by the U.S. Department of Energy, National Nuclear Security Administration, Defense Nuclear Nonproliferation R&D (NA-22) and the Office of Science, Office of High Energy Physics, under Contract No. DEAC02-05CH11231, and by a generous philanthropic gift from Google LLC.

Chapter 1

Introduction

1.1 Driving interests in understanding isomer population manipulation

Nuclei can be excited to energies above their ground state. A small fraction of these nuclei exhibit lifetimes on the second, hour, day, and year timescales. Together, these metastable states known as nuclear isomers are characterized by a characteristic energy above the ground state, E, an orbital angular momentum component, J, parity, π, and a characteristic half-life, $\tau_{1/2}$. Isomers are utilized in a broad scope of applications. Various medical imaging techniques utilize isomers as controlled radiation sources, such as $^{99m}_{43}$Tc, which comprises roughly $\approx 85\%$ of nuclear medical procedures [1]. Other current uses for nuclear isomers include environmental monitoring and industrial radiation sources. Advances in science and technology allow for more applications of nuclear isomers and including but not limited to advanced radio-medicine, nuclear batteries for power storage, advanced radiation detectors, and quantum computing applications [2, 3].

The ability to directly manipulate isomer populations may provide a powerful tool for re-purposing a fraction of spent nuclear fuel. Formed by neutron capture in thermal reactors, ^{242m}Am acts as a gateway to much longer lived isotopes [4]. With its lifetime of $\tau_{1/2} \approx 141$ years, ^{242m}Am poses a challenge as it requires active storage monitoring for hundreds of years [5]. If the ^{242m}Am state could be depopulated into the ^{242}Am ground state, its β-decay into ^{242}Cm, followed by α-decay into ^{238}Pu, could be hastened significantly. This decay tree is illustrated in Figure 1.1. By transitioning from the ^{242m}Am state into the ^{242}Am ground state, the lifetime becomes $\tau_{1/2} = 16.01$ hours [6]. This transition would drastically reduce storage requirements, but more significantly it would create a source of ^{238}Pu, which is used as a source isotope in radio-isotope thermo-electric generators (RTGs) for providing electrical power during space operations. ^{238}Pu is an ideal candidate for these devices as an α-emitter with minimal neutron and gamma contributions, and a $\tau_{1/2} = 88.7$ years [7]. Currently, United States domestic production of ^{238}Pu at Oak Ridge National Laboratory's High Flux Neutron Generator is targeting 1.5 kg of isotope by 2026 [8]. Previously fielded RTGs have

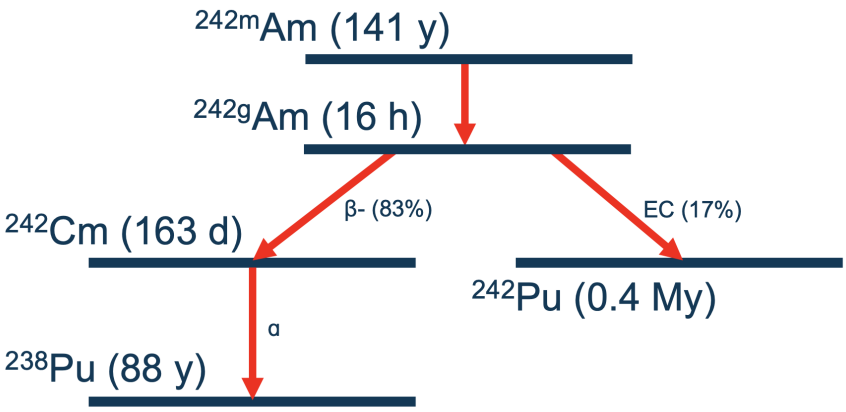

Figure 1.1: Schematic for decay of ^{242}Am into ^{238}Pu with half-lives indicated [6]. Here, $\beta-$ refers to beta decay, α refers to alpha decay, and EC refers to the electron capture decay process.

used several kilograms of fuel material per unit, so interest in enhanced production through isomer manipulation is present.

In the astrophysical setting isomers are thought to play an important role in stellar nucleosynthesis, especially around $A \approx 80$ [9, 10]. Recently, further work by Misch et al. has been performed in analyzing the importance of "astromers" in stellar reaction rates [11]. In this work the effect of long-lived isomers on the s-process is discussed as a function of system temperature, with isomeric states requiring treatment as separate species below a given "thermalization temperature". Additionally, the role of astromers in the r-process is explored, with results suggesting that disparities between ground state and isomer lifetimes may have significant consequences on radioactive heating [11]. This analysis highlights the importance of understanding isomer feeding pathways and the effects of isomer populations on heavy isotope formation in stellar environments.

1.2 Physical sources of long isomer lifetimes

These long-lived isomers are attributed to a multitude of nuclear structure effects. Of primary interest to this work are spin-isomers, where the isomeric state has a significant spin difference, ΔJ, relative to lower lying states. Similarly, K isomers result when de-excitation of the isomeric state requires a large change in the K quantum number, or the projection of the nucleus's rotation axis on its axis of symmetry. K isomers are seen in highly deformed, non-spherical nuclei. Another type, shape isomers, result when local energy minima in the nuclear potential exist at states of large nuclear deformation [12]. For the case of spin isomers it is instructive to undergo a qualitative analysis of transition rates through multipole electromagnetic radiation emission using the Weisskopf estimates, as evaluated by Krane [13].

Transition rates, λ, in units of s^{-1}, are given for electric transitions as a function of atomic mass, A, and the transition energy in MeV, E, in Equation 1.1. Multipole order is denoted with an integer on the left-hand side of the equation. For example, $\lambda(E1)$ refers to an electric dipole transition rate while $\lambda(E2)$ refers to an electric quadrupole transition.

$$\begin{aligned}\lambda(E1) &= 1 \times 10^{14} A^{2/3} E^3, \\ \lambda(E2) &= 7.3 \times 10^{7} A^{4/3} E^5, \\ \lambda(E3) &= 34 A^2 E^7, \\ \lambda(E4) &= 1.1 \times 10^{-5} A^{8/3} E^9.\end{aligned} \tag{1.1}$$

Similarly, transition rate estimates are presented in Equation 1.2 for magnetic transitions:

$$\begin{aligned}\lambda(M1) &= 5.6 \times 10^{13} E^3, \\ \lambda(M2) &= 3.5 \times 10^{7} A^{2/3} E^5, \\ \lambda(M3) &= 16 A^{4/3} E^7, \\ \lambda(M4) &= 4.5 \times 10^{-6} A^2 E^9.\end{aligned} \tag{1.2}$$

During a nuclear transition total angular momentum must be conserved, and can be represented as $I_i = L + I_f$, where L is the order of the multipole operator, and I_i and I_f are the angular momentum of the initial and final nuclear states, respectively. For de-excitation through gamma emission, it is taken that a multipole of order L will radiate a photon with $L\hbar$ angular momentum [13]. Additional attention must be paid to change in parity, $\Delta\pi$, between the initial and final states as this further restricts the type of transitions that can occur. The parity rules for both electric and magnetic dipole transitions are shown in Equation 1.3, which indicate that electric transitions are parity-preserving for even L and parity-changing for odd L order multipoles. The opposite is true for magnetic transition:

$$\begin{aligned}\pi(EL) &= -1^L, \\ \pi(ML) &= -1^{L+1}.\end{aligned} \tag{1.3}$$

Within this framework, a qualitative analysis of indicates that increasing L, or ΔJ, significantly reduces the transition rate between states, with electric transitions generally favored for a given L. Increasing E leads to increased transition rates, however L is the dominant factor in determining transition rates.

It is readily seen that long-lived spin-isomers can be attributed to the suppressed transition rates of higher order L multipoles, as lifetime is inversely proportional to the transition rate. An example relevant to this work is the ground state $3/2^+$ ^{79}Br nucleus and its next available level, the 207.64 keV, $9/2^+$ isomer $^{79\mathrm{m}}$Br [14]. For a nucleus in the $^{79\mathrm{m}}$Br state to de-excite to the ground state, a $\Delta J = 3$ transition with $\Delta\pi = 0$ must occur. Using the Weisskopf estimate for the most probable M3 transition, $\lambda(M3) \approx 0.088$, which corresponds to an estimated half-life of $\tau_{1/2} \approx 7.85$ seconds. This value is representative of the

experimentally observed $\tau_{1/2} = 4.85$ seconds. For this case, there is good agreement between Weisskopf estimates and experimental results. Weisskopf estimates represent single-particle transitions and do not account for collective behavior. Observed state lifetimes can differ significantly from those predicted by Weisskopf estimates: the well known K isomer in ^{180}Hf being a prime example [15].

1.3 Manipulation of isomer populations

Advanced applications of nuclear isomeric states require the ability to manipulate their populations directly, either populating or depopulating them. In the simplest case, direct population of an isomeric state could be achieved by photon capture on a nucleus, assuming the photon has the correct energy and angular momentum to populate the target isomeric state. Unfortunately, this is difficult to achieve in practice as a result of the uncertainty principle relating lifetime and state energy width, as shown in Equation 1.4 [16, 17],

$$\Delta E \Delta t \geq \frac{\hbar}{2}, \tag{1.4}$$

where ΔE is the energy width of a state, while Δt is the lifetime of the state. This relation describes a fundamental principle of nuclear states; it implies a long-lived state, with large Δt, must have a narrow energy width, or a small ΔE. Stated in reverse, a short-lived state must have a large energy width. It is in this relation that direct access of long-lived nuclear isomer states finds its first hurdle. By definition, an isomer must have a large Δt with an accompanying small ΔE, or access window to the state. This makes direct population of isomers with functionally long lifetimes prohibitively difficult.

An example relevant to this work is the direct population of the ^{79m}Br isomer, which has a measured half-life $\tau_{1/2} = 4.85$ seconds [14], with an accompanying ΔE of $\approx 10^{-17}$ eV per Equation 1.4 that is many orders of magnitude of precision below any currently known photon source. A more favorable case, such as the de-population of the ^{242m}Am isomer by excitation into the next available state followed by de-excitation via gamma emission to the ground state, is shown in Figure 1.2. The target level has a known lifetime of $\approx 10^{-9}$ seconds with a corresponding ΔE of $\approx 10^{-7}$ eV, which remains an unfeasible target for direct access using photon sources. Even without consideration for angular momentum, the relations imposed by Equation 1.4 mean that direct manipulation of isomer populations using photon irradiation is exceedingly difficult.

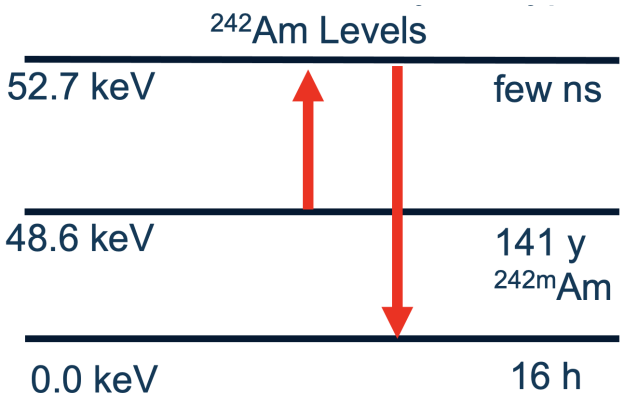

Figure 1.2: Level scheme of ^{242}Am nucleus near the ground state, with the red arrows indicating excitation out of the ^{242m}Am state into the next available state at 52.7 keV [6].

1.3.1 Efforts in photon driven excitation of isomer states

Direct photon excitation of isomer states is difficult to achieve due to energy width constraints and typical large spin differences between ground and isomer states. This has driven interest in indirect population of isomer states by accessing higher energy feeding bands, which could decay into the desired isomer state. There have been efforts to experimentally explore these non-resonant (γ, γ') reactions by Carroll et al. [18]. They suggest the nuclei studied may have enhanced (γ, γ') feeding into low-lying isomer states for incoming photons with energies between 3 and 4 MeV, with no conclusive evidence for additional strong feeding channels opening up above 6 MeV [18]. This non-resonant approach has yet to be proven as an effective tool for use in applications. Additionally, applied use of this approach requires specific knowledge of feeding levels in a given candidate nucleus, which provides a challenge in itself.

Other efforts seek to use optical frequency photons to populate isomer states. This approach is limited to nuclei which have very low-lying isomer states, as optical frequency photons are limited to few eV, as opposed to the more typical keV and MeV scales seen in nuclear excitation mechanisms. With its recently observed radiative decay [19], ^{229m}Th drives strong interest as a "nuclear clock" isomer. With a very low energy isomer predicted to exist near $\approx$ 7.8 eV, there have been efforts to excite this state directly using optical photons generated by an electron undulator [20]. Additional efforts have focused on using optical photons to excite atomic states, which can then resonantly couple into the nucleus and populate the isomer state through the inverse electronic bridge mechanism, however these experiments are inconclusive [21].

1.3.2 Indirect population of isomer states

Many of the techniques used in studying nuclear isomers rely on indirect access to isomeric states using particle beams to probe nuclear reaction pathways, with some fraction of the products populating isomer states. Studies performed using non-relativistic ($\approx$ 6 MeV/Nucleon) particle beams rely on multi-particle transfer and inelastic reactions in target nuclei which result in a large number of possible products, a fraction of which may represent an isomer state [15]. Fusion-evaporation reactions on heavier nuclei targets may populate an isomer state in the fused nucleus or emit particles, often neutrons, with the resulting nucleus populating an isomer state. Partial fusion reactions, also called projectile breakup reactions, use a similar process but rely on the beam nucleus to break up before the fusion reaction occurs, which allows for larger amounts of spin to be coupled into the resultant nuclei [12]. Inelastic scattering using non-relativistic heavy beam nuclei on heavy target nuclei is another technique used for studying very high spin states [12]. Additional work has been performed using relativistic beams ($\approx$ 1 GeV/Nucleon) coupled with magnetic separators for reaction fragments to discover isomer states in heavy nuclei [15].

Isomers can also be formed as a result of nuclear fission and the decay of its products. For medical applications, most ^{99m}Tc is sourced from ^{99}Mo formed by thermal fission reactions in ^{235}U fuel pellets. With a $\tau_{1/2}$ = 66 hours, ^{99}Mo decays into ^{99m}Tc. This production process also generates the medically significant isotopes ^{131}I and ^{133}Xe [22]. There are efforts exploring the ^{98}Mo$(n,\gamma)^{99}$Mo reaction using high-flux neutron sources for medical isotope production, however they have yet to be proven more effective than fission sources [23]. Work examining ^{100}Mo(γ,n)^{99}Mo reactions using laser-plasma accelerator sourced bremsstrahlung photons up to 1.7 GeV has also been performed [24].

1.4 The need for new methods of isomer population manipulation

Advanced applications for isomers, such as use in batteries, will require new techniques for manipulating isomer state populations. Per Tavares and Terranova [2], suitable candidates for nuclear isomer batteries include α, β, and γ emitters. In the cases of α and β emitters, the nuclei is transmuted and the previously populated isomer state is inaccessible. With proper shielding and design, γ emitting isomers provide an exciting source of potentially rechargeable nuclear batteries. For this application goal to be feasible, techniques for populating and depopulating such isomer states are required. Direct photon excitation into isomer states remains an unlikely approach, given the strict requirements for spin and energy of the incoming photon. Non-resonant photon excitation methods require advanced knowledge of nuclear feeding levels on a per nucleus basis and have yet to be demonstrated as a precise tool for driving applications. Fission sources and energetic particle beam approaches are insufficiently precise, as the inherent stochastic characteristics of these interactions require that potentially undesirable reaction pathways are present. Optical excitation methods, either di-

rectly or indirectly, may eventually be a powerful tool for nuclei with appropriately low-lying isomers, but are inherently limited in scope of application by their very low energies.

It is clear that alternative methods to isomer population manipulation should be explored. While present methods provide powerful research and discovery tools, precise access to isomer states represents a necessary step for the development of advanced applications for nuclear isomers. In this work, we introduce and discuss the concept of indirect isomer population manipulation through the nuclear quasicontinuum utilizing the enhanced energy-spin coupling provided by nuclear-plasma interactions (NPIs), as enabled by the ultra-short electron bunches generated by laser-plasma accelerators. Chapter II introduces the nuclear quasicontinuum, the theoretical models used to characterize it, and nuclear-plasma interactions. Chapter III introduces laser-plasma accelerators as a concept and will detail how these platforms enable unprecedented probing of the nuclear quasicontinuum. Additional content will detail the experimental platform that enables the operation of these laser-plasma accelerators. Chapter IV details experimental work performed with Bromine nuclei, and the analysis of those results. A conclusion contextualizes those results within a larger scope, and lays the groundwork for future efforts.

Chapter 2

The Nuclear Quasicontinuum and Nuclear-Plasma Interactions

2.1 Characterizing non-discrete nuclear states at high excitation energies

In searching for an alternative method of manipulating isomer populations in nuclei, it is necessary to understand the fundamental interactions that dictate how nuclei transition between states. In the quantum description of nuclei and their excited states, we can ascribe an observed state to the cumulative wave function of all constituent particles. In this framework, a transition between states in a nucleus represents a change in the cumulative wave function, or $\psi_i \rightarrow \psi_f$, where ψ_i is the initial state and ψ_f is the final state. It is instructive to model the transition rates between two states, ψ_i and ψ_f, in a generalized form. Fermi's golden rule provides this description,

$$T(E_\gamma, E_x) = [< f|V(E_i - E_f)|i >]^2 \times \rho(E_f), \tag{2.1}$$

where $T(E_\gamma, E_x)$ is the transition rate between states via a photon of E_γ to a state with an excitation energy above ground E_x. This E_x term is distinct from the difference between the initial and final energies, E_i and E_f, to include transitions between excited states. The transition between states is captured by the $V(E_i - E_f)$ term, which represents the nuclear matrix element of the transition operator [13]. This operator term is stronger for more similar states, with transitions between less similar states being suppressed. For our case of photon emission or capture, this behavior is demonstrated by the Weisskopf estimates presented in Chapter I, where larger spin differences between states exponentially decrease expected transition rates. In its full form, $[< f|V(E_i - E_f)|i >]^2$ provides the transition probability between states ψ_i and ψ_f as mediated by the transition operator. The right-hand term $\rho(E_f)$ represents the density of available states at the final energy. Examination of this equation suggests simply that transitions between similar states in regions of high state density are enhanced, while transitions between dissimilar states into regions of low state density are

suppressed. Transition rates are particularly sensitive to adjustments in the matrix operator V, as result of its second order contributions.

In working with discrete states in a nucleus, the framework provided by Fermi's golden rule may not be the best tool for calculating transition rates between states. However, known discrete levels in nuclei are limited to what can be experimentally measured. Missing states can be estimated for use in calculations, such as those performed by TALYS [25]. This approach is suitable in regions where discrete levels are expected, but as excitation energy increases the density of levels increases as well. This increasing density of states can make discrete modelling of states a cumbersome approach, and calls for new mathematical treatment. Per Guttormsen et al. [26], the density of available levels can range from $10^3 - 10^7$ for nuclei of $A \approx 50 - 180$ at the neutron separation energy, S_n. Further increasing with excitation energy, it is clear that discrete levels are not useful for modelling nuclear excitation and transitions.

In working with high energy excitation of nuclei, the concept of the nuclear quasicontinuum becomes a powerful tool. In this framework, the nuclear states are considered densely packed enough to be overlapping at a given energy, removing the need for discrete identification. Instead, two concepts are used to model transitions through the nuclear quasicontinuum. These are the nuclear level density (NLD) and gamma strength (γSF) functions. Nuclear level density models provide a continuous function describing the distribution of states as a function of excitation energy, spin, and parity in levels/MeV. Gamma strength functions attempt to model the probability of a transition occurring between any two states, through photon absorption or gamma decay. Together these concepts model the likelihood of transitions between potential states in the nuclear quasicontinuum as a function of energy, spin, and parity of the initial and final states. Additionally, the quasicontinuum allows for calculating nuclear reaction cross sections without knowledge of discrete states [25]. Sufficient characterization of the nuclear level densities and gamma-strength functions for a given nucleus allow for the potential of intentional excitation of the nucleus into regions of the quasicontinuum that may preferentially decay into a desired isomer state, or in the reverse case, provide a wide target for exciting an isomer state into the quasicontinuum so that it may decay into the ground state, as illustrated in Figure 2.1. This will be explored later in Chapter II.

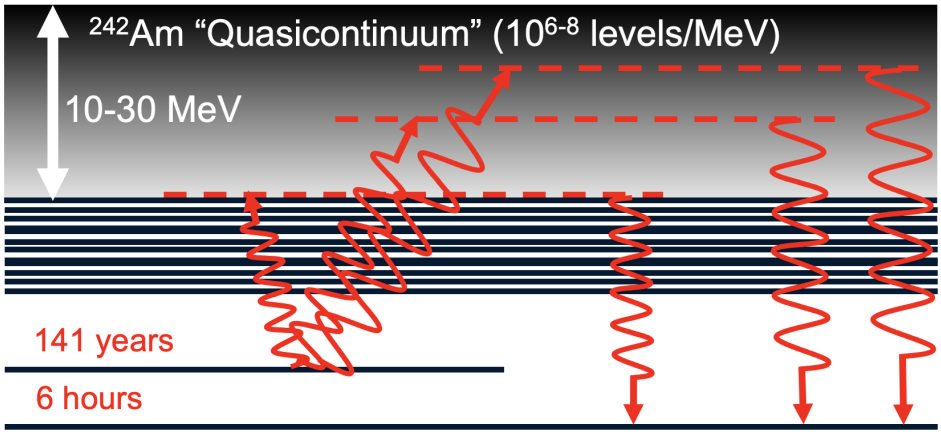

Figure 2.1: Schematic abbreviated level scheme for ^{242}Am, showing the ^{242m}Am isomer excited into the quasicontinuum, followed by decay into the ground state [6].

2.2 Nuclear level density models

The density of states term, $\rho(E_f)$, in Equation 2.1 can be cast as the nuclear level density component in modeling the nuclear quasicontinuum. It is necessary to provide NLD models for calculating transition rates. In this section, we will review the general conceptualization as well as the specific NLD models utilized in the calculations discussed later in this work. All calculations are performed with TALYS, a software package used to analyze and predict nuclear reactions using a combination of measured data and theoretical models [25]. In discussing prominent NLD models, it is necessary to establish a common definition for the mathematical treatment used in TALYS calculations [25]. Note, in this section Π is used to reference parity, while π is reserved for the mathematical constant. Per Koning et al. [27], it is useful to define the total level density around a given excitation energy, E_x, as;

$$\rho_{levels}(E_x) = \sum_J \sum_\pi \rho(E_x, J, \Pi), \tag{2.2}$$

where J is the spin and Π is the parity of a given level. This is directly related to the total state density to account for degeneracy in the magnetic quantum number, M, by:

$$\omega_{state}(E_x) = \sum_J \sum_\Pi (2J+1)\rho(E_x, J, \Pi), \tag{2.3}$$

which includes the necessary $(2J+1)$ factor. This work will discuss the six models utilized in TALYS, which includes three phenomenological models and three microscopic models. For nuclear level densities taken from phenomenological models the total level density is factorized as

$$\rho(E_x, J, \Pi) = P(E_x, J, \Pi) R(E_x, J) \rho_{levels}(E_x), \tag{2.4}$$

where $P(E_x, J, \Pi)$ is the parity distribution and $R(E_x, J)$ is the spin distribution. For all three phenomenological models and one microscopic model, an equipartition of $P(E_x, J, \Pi) = 1/2$ is assumed.

Common to all of the NLD models to be presented is an exponentially increasing level density with excitation energy. This is attributed to the combinatorial nature of excited states in nuclei. With an increased number of particles, the number of potential available states increases drastically [26]. These effects are more pronounced with increasing E_x as pairing and collective effects are suppressed. Of particular interest to this work are the enhanced NLDs at 10's of MeV. The implications of this will be discussed later in Chapter 2.

2.2.1 Fermi gas Model

The Fermi gas Model treats (FGM) the nucleus as being composed of two Fermi gasses, one of protons and the other of neutrons [28]. Within this framework, the nucleons inhabit single particle levels within the nuclear potential they create, up to the Fermi energy. If additional energy is added to the system nucleons will inhabit single particle levels above the Fermi energy, leaving vacancies below it. This approach assumes equally spaced levels, with no consideration for collective levels [25]. Following this framework, the total Fermi gas state density for a two-fermion system can be expressed as [27]

$$\omega_F^{total}(E_x) = \frac{\sqrt{\pi}}{12}\frac{\exp 2\sqrt{aU}}{a^{1/4}U^{5/4}}, \tag{2.5}$$

which contains the level density parameter a and an effective excitation energy U. Theoretically, a is represented as

$$a = \frac{\pi^2}{6}(g_p + g_n), \tag{2.6}$$

where g_p and g_n are the level spacing near the Fermi energy. Prior models calculated these values as proportional to $(2J+1)^{-1}$ [29], but more recent work assumes energy dependence and utilize experimentally determined values, where possible [25]. The expression for the effective excitation energy

$$U = E_x - \Delta, \tag{2.7}$$

contains the factor Δ which is adjustable parameter intended to provide a correction for breaking paired nucleons in odd-even nuclei and the observed effects this has on state distribution [30, 27]. Following the derivations presented by Ericson [31], assuming an equipartition in parity and an assumed spin distribution of the form

$$R_f(E_x, J) = \frac{2J+1}{2\sigma^2}\exp\left[-\frac{(J+1/2)^2}{2\sigma^2}\right], \tag{2.8}$$

an energy, parity, and spin dependent expression for the Fermi gas level density can be found in the form of Equation 2.4,

$$\rho_F(E_x, J, \Pi) = \frac{1}{2}\frac{2J+1}{2\sqrt{2\pi}\sigma^3}\exp\left[-\frac{(J+1/2)^2}{2\sigma^2}\right]\frac{\sqrt{\pi}}{12}\frac{2\sqrt{aU}}{a^{1/4}U^{5/4}}, \tag{2.9}$$

where the introduced factor σ^2 is the width of the angular momentum distribution for the level density. When summed across possible parity and spin states, Equation 2.9 assumes a form analogous to Equation 2.2,

$$\rho_F^{tot}(E_x) = \frac{1}{\sqrt{2\pi}\sigma}\frac{\sqrt{\pi}}{12}\frac{\exp\left(2\sqrt{aU}\right)}{a^{1/4}U^{5/4}}, \tag{2.10}$$

which can be related to the total density of states as presented in Equation 2.5 and takes the form,

$$\rho_F^{tot}(E_x) = \frac{\omega_F^{tot}(E_x)}{\sqrt{2\pi}\sigma}, \tag{2.11}$$

where nuclear level density is a function of three components. The level density parameter a, spin-distribution width σ^2, and the pairing correction term Δ provide the defining characteristics for the FGM. Together these terms allow for inclusion of shell-effects based on energy dependent phenomenological definitions of a and σ^2 [25].

2.2.1.1 Defining the level density parameter and spin distribution width

The parameters a and σ^2 are used within multiple NLD models and will be defined here for reference. The definition of a is

$$a(E_x) = \tilde{a}\left(1 + \delta W\frac{1-\exp\left(-\gamma U\right)}{U}\right), \tag{2.12}$$

following work done by Ignatyuk et al. establishing a as a function of excitation energy [32]. In this form, $\tilde{a}$ is the asymptotic level density parameter $\tilde{a} = a(E_x \to \infty)$, δW is the shell correction factor, and γ is a damping parameter. Together δW and γ determine the strength of shell effect modifications to the level density and how strongly they scale with increasing E_x on a per nuclei basis, respectively. In this form, $\tilde{a}$ can be enhanced or hindered with increasing E_x as the sign of δW can be determined individually for a given nuclei to match experimental results.

Lastly, the spin distribution width σ^2 is derived from the angular momentum states in single particle states projected onto a nucleus's symmetry axis, with an inclusion for energy dependence [33, 34]. The width is

$$\sigma_F^2(E_x) = I_0\frac{a}{\tilde{a}}\sqrt{\frac{U}{a}}, \tag{2.13}$$

where the spherical moment of inertia I_0 is defined as

$$I_0 = 2/5\frac{m_0R^2A}{(\hbar c)^2}, \tag{2.14}$$

with $R = 1.2A^{1/3}$ as the nuclear radius and m_0 the mass of the neutron. With this definition, Equation 2.13 can be simplified to

$$\sigma_F^2(E_x) = 0.01389 \frac{A^{5/3}}{\tilde{a}} \sqrt{aU}, \tag{2.15}$$

which defines the spin distribution as a function of atomic mass, excitation energy, and shell effects. Recalling Equation 2.7, this form of σ_F^2 is undefined for small E_x. Stricter definitions of σ_F^2 exist for low excitation energies ($< S_n$), but do not require review here as the focus of this work exceeds the energy thresholds in question [25].

2.2.2 Constant Temperature Model

Introduced by Gilbert and Cameron [35], the Constant Temperature Model (CTM) serves to provide a low E_x correction to the Fermi gas Model to better match experimentally observed neutron and proton resonance data. Following this approach, an exponential law of the form

$$N(E_x) = \exp\left(\frac{E_x - E_0}{T}\right) \tag{2.16}$$

represents the cumulative discrete levels in a nucleus, with T the nuclear temperature and E_0 an adjustable parameter for matching experimental results. Taking the derivative of this with respect to excitation energy yields the total level density,

$$\rho_{CTM}^{tot}(E_x) = \frac{1}{T} \exp\left(\frac{E_x - E_0}{T}\right), \tag{2.17}$$

in a form that allows for fitting to experimental data by adjusting T and E_0. For the implementation of this model in level density calculations, Equation 2.17 is utilized below some matching energy E_m, where at the FGM is implemented with Equation 2.10 [25, 35]. Per the matching condition

$$\rho_{CTM}^{tot}(E_m) = \rho_{FGM}^{tot}(E_m), \tag{2.18}$$

careful determination of E_m is required to ensure best fitting of T and E_0 to experimental data. Additional inclusion of pairing effects is achieved for the FGM contributions above E_m by utilizing a modified definition of the energy shift Δ in Equation 2.7. In the CTM implementation, the energy shift is defined as

$$\Delta^{CTM} = \chi \frac{12}{\sqrt{A}}, \tag{2.19}$$

with the pairing coefficient χ as defined below.

$$\chi = \begin{cases} 0, \text{ odd-odd} \\ 1, \text{ odd-even} \\ 2, \text{ even-even} \end{cases} \tag{2.20}$$

As noted by Gilbert and Cameron, the CTM model allows for pairing effects through the χ coefficient in the FGM regime, with the experimental coefficients T and E_0 allowing individual nuclei to be experimentally fit at low E_x. However, they note difficulty in achieving the E_m matching condition for certain light nuclei and nuclei near shell closures [35].

2.2.3 Back-shifted Fermi gas Model

In working to improve the Fermi gas Model for representing nuclei with inclusion for pairing effects, Dilg et al. [36] introduced an alternative definition for the effective excitation energy defined in Equation 2.7 as

$$U = E_x - \Delta^{BFM}, \tag{2.21}$$

where Δ^{BFM} is a pairing corrected energy shift defined as

$$\Delta^{BFM} = \chi \frac{12}{\sqrt{A}} + \delta, \tag{2.22}$$

with δ as an adjustable parameter and χ capturing pairing effects through the following definition [25].

$$\chi = \begin{cases} -1, \text{ odd-odd} \\ 0, \text{ odd-even} \\ 1, \text{ even-even} \end{cases} \tag{2.23}$$

The Fermi gas Model level density, as defined in Equation 2.10, diverges as $E_x \to 0$ preventing its use for low E_x. Work done by Grossjean and Feldmeier [37] and adjusted by Demetriou and Goriely [38] resulted in a modified Fermi gas Model of the nucleus that provides a continuous expression for level density at low E_x with pairing effects. As implemented in TALYS [25], this expression takes the form

$$\rho^{tot}_{BSFGM}(E_x) = \left(\frac{1}{\rho^{tot}_F(E_x)} + \frac{1}{\rho_0(t)} \right)^{-1}, \tag{2.24}$$

where

$$\rho_0 \left(\sqrt{\frac{U}{a}} \right) = \frac{\exp(1)}{24\sigma} 2a^2 \exp\left(a^2 \left(\sqrt{\frac{U}{a}} \right)^2 \right), \tag{2.25}$$

which includes the previously defined level density parameter a. In this form, the Back-shifted Fermi gas Model (BSFGM) provides an alternative to the CTM which preserves the general exponential shape of the Fermi gas Model at low E_x, with additional consideration of pairing effects.

2.2.4 Generalized Superfluid Model

The Generalized Superfluid Model (GSM) was formulated to intrinsically implement particle pairing correlations into NLD calculations, following the framework of Bardeen-Cooper-Schrieffer (BCS) theory [39, 40]. This framework introduces the transition temperature, T_c, below which a superfluid state is assumed with strong pairing correlations having significant effect on level densities. Above T_c the nucleus loses its superfluidity and is modelled using the Fermi gas model with a modified effective excitation energy U which includes the condensation energy, E_{cond}, that arises from the BCS theory [40, 25]. An extensive mathematical treatment of the GSM can be found by Ignatyuk [39] and in the TALYS manual [25], but will be omitted here in favor of highlighting key components. Of critical importance is the transition temperature,

$$T_c = 0.567\Delta_0, \tag{2.26}$$

where Δ_0 is the pairing correlation factor. Together these terms require a reduced T_c as the atomic mass number A increases.

$$\Delta_0 = \frac{12}{\sqrt{A}}. \tag{2.27}$$

Using these definitions, the transitional excitation energy U_c can be defined as

$$U_c = a_c T_c^2 + E_{cond}, \tag{2.28}$$

where a_c is the critical level density parameter, similar to that defined in Equation 2.12, and the condensation energy is defined as

$$E_{cond} = \frac{3}{2\pi^2} a_c \Delta_0^2, \tag{2.29}$$

which includes a second order dependence on the pairing correlation factor. Together, these terms suggest that pairing effects strongly effect level densities at low energies in smaller nuclei. With increasing A, these pairing effects are restricted to decreasing transition temperatures. The quicker transition to FGM behavior can be attributed to reduced pairing effects in large nuclei, as nucleons are farther apart on average. For $U \leq U_c$, the total level density expression takes the form of

$$\rho_{GSM}^{tot}(E_x) = \frac{1}{\sqrt{2\pi}\sigma} \frac{\exp(S)}{\sqrt{D}}, \tag{2.30}$$

where S is the thermodynamic entropy and D is the determinant taken from the saddle point approximation in applying BCS theory [39, 25]. For $U > U_c$, the total level density takes a form similar to Equation 2.10, with a modified definition of the effective excitation energy U using E_{cond} to wrap in pairing contributions and their scaling with A. Moretto et al. [41] analyzed experimentally measured low energy level densities in rare-earth nuclei and actinides, with results suggesting strong evidence for the theorized T_c factor from the BCS model properly capturing even-odd effects and the breakdown in pairing strength with increasing energies.

2.2.5 Microscopic level density models

In addition to the phenomenological models detailed above, there are microscopic level density models based on Hartfree-Fock calculations [42]. These calculations attempt a generalized fit for many measured nuclei with $A > 36$ using a Skyrme force model of the nuclear potential [43]. In this model the nuclear potential is simplified to an averaged potential of many nucleons, with individual nucleons populating levels within the averaged potential. Within TALYS there are three microscopic level density models available in the form of pre-tabulated values [25]. The first of these microscopic tables fit 1888 experimental nuclei using the Skyrme force and BCS theory for pairing correlations [42]. Further work was done to improve these calculations using a Hartree-Fock-Bogoliubov plus combinatorial method, which allows for inclusion of energy, spin, and parity dependence on level density, with enhancement from collective modes such as vibrational or rotational states [44]. These calculations were further improved upon using a Gogny force model in-place of the Skyrme force used previously [45]. This transition allows for better treatment of discrete levels at low energies and collective effects. Using this updated approach, Hilaire et al. [46] calculated level densities which account for energy dependent pairing, shell, and deformation in nuclei with improved implementation of collective state enhancements.

With NLDs tabulated for each nuclei, TALYS determines the level density used in a calculation with the equation

$$\rho(E, J, \Pi) = \exp\left(c_{HF}\sqrt{E_x - \delta}\right)\rho_{HFM}(E_x - \delta, J, \Pi), \tag{2.31}$$

where the resultant level density ρ can be modified from the table value, ρ_{HFM}, by two parameters δ and c_{HF} [25]. The pairing shift parameter δ provides an adjustable offset for the energy column in the ρ_{HFM} table. The constant c_{HF} provides an adjustable multiplicative factor, the effect of which inherently scales with E_x per Equation 2.31. Together these factors are intended to provide a tool for better fitting the microscopic NLD values to experimental values.

2.3 Gamma strength functions

In the general form, nuclear transition rates can be understood using Fermi's Golden Rule, shown in Equation 2.1. With the previous section discussing the nuclear level density term, $\rho(E_f)$, and the various phenomenological and microscopic models used in calculations, it is time to shift focus to the other term in Equation 2.1. In its full form, $[< f|V(E_i - E_f)|i >]^2$, the transition operator term represents the likelihood of a transition occurring between two states via the transition $V(E_i - E_f)$. Within bound nuclei, excited nuclei with insufficient energy for a nucleon to exceed the nuclear potential, this probability term is proportional to the gamma strength function [26]. The gamma strength function represents the averaged likelihood of a nucleus to absorb or emit a photon of a given energy, to or from a specified energy. This approach is especially useful in regions where discrete levels are unknown or

are largely unidentifiable, due to increased nuclear level densities, such as those observed in the nuclear quasicontinuum. For transitions out of higher energy states ($> S_n$) that exist within the quasicontinuum, low multipole $E1$ and $M1$ transitions are dominant [47]. For the purposes of this work in discussing the photo-excitation of nuclei and transition into isomeric states, the focus of discussion is on transitions involving photons, either excitation by photon absorption or de-excitation by photon emission. However, it is crucial to note that gamma strength functions also affect the likelihood of other outgoing channels such as (γ, n) reactions where photon absorption is necessary for the transition to occur.

Before introducing individual gamma strength function models, it is necessary to provide the generalized form in which they are used, as presented in theory and implemented within TALYS calculations [25]. The strength function is denoted as $f_{Xl}(E_\gamma)$, with X representing the multipole type and l the multipole order as introduced with the Weisskopf estimates for the single particle model of electromagnetic transitions in Chapter 1. In this presentation, the $f_{E1}(E_\gamma)$ strength function represents the most likely $E1$ transition from quasicontinuum states. This strength function is related to the transition cross section $\sigma_{Xl}(E_\gamma)$ for absorption of a photon with E_γ by

$$f_{Xl}(E_\gamma) = K_{Xl}\frac{\sigma_{Xl}(E_\gamma)}{E_\gamma^{2l-1}}, \tag{2.32}$$

where the transition cross section can be summed over multipole type and order to determine the total averaged photon absorption cross section given by Equation 2.33,

$$\sigma_\gamma(E_\gamma) = \sum_{Xl}\sigma_{Xl}(E_\gamma). \tag{2.33}$$

In this form, the total photon absorption cross section accounts for all potential spin and parity changes. The term K_{Xl} is a multipole order correction defined as

$$K_{Xl} = \frac{1}{(2l+1)\pi^2\hbar^2c^2}. \tag{2.34}$$

Historically, absorption of high energy photons was experimentally observed through (γ, n) reactions, which are assumed to dominate the cross section and thusly the gamma strength function [48, 25].

De-excitation through photon emission is conceptualized separately with its own formal definition of the downward strength function based on (n, γ) reactions populating excited states below S_n [25]. In utilizing the Hauser-Feshbach statistical model [49] for determining competition between decay pathways, TALYS relates the specific photon transmission coefficient T_{Xl} to the strength function via the expression

$$T_{Xl}(E_\gamma) = 2\pi f_{Xl}(E_\gamma)E_\gamma^{2l+1}, \tag{2.35}$$

where E_γ is the energy of the photon emitted during decay. In calculating the total photon transmission coefficient, a summation of all possible initial and final spin, parity, and energy

states is performed below S_n. The total photon transmission coefficient is

$$T_\gamma = \sum_J \sum_\Pi \sum_{Xl} \sum_{I'=|J-l|}^{|J+l|} \sum_{\Pi'} \int_0^{S_n} dE_\gamma T_{Xl}(E_\gamma) \rho(S_n - E_\gamma, I', \Pi') F(X, \Pi', l), \tag{2.36}$$

where J and Π are the initial state spin and parity, while I' and Π' are the final state spin and parity. The multipole selection rule function $F(X, \Pi', l)$ is valued at 1 only for transitions that satisfy the parity rules presented in Equation 1.3, and 0 for all other cases [25]. This lower energy portion of the gamma strength function is rooted in experimental observed (n, γ) reaction cross sections [49, 48].

The absorption and emission gamma strength functions are unified through the Brink-Axel Hypothesis, which suggests that photon emission or absorption strengths are independent of excitation energy, spin, and parity [50]. The general validity of the Brink-Axel Hypothesis is still a focus of contemporary research. Per Guttormsen et al. there are experimental validations for certain γ photon energies in heavier nuclei, but some experiments with lighter nuclei ($A < 100$) are not consistent with the Brink-Axel Hypothesis [50]. Recent experimental work with ^{238}Np nuclei suggest the gamma strength function maintains E_x independence through both the quasicontinuum and levels lying below S_n [51]. Similar conclusions were reached by Markova et al., probing Sn nuclei at 16 MeV [52]. This agreement becomes less clear in lighter nuclei, per Campo et al., with efforts to probe ^{64}Ni and ^{65}Ni nuclei below S_n showing general agreement with large fluctuations in feeding strengths to low lying levels [53].

2.3.1 Lorentzian models for gamma strength functions

There are a handful of phenomenological models used in calculating gamma strength functions, with the original models based on the concept of the Giant Dipole Resonance (GDR) as presented by Brink and Axel [54, 55]. The GDR is generally attributed to collective motion of nucleons, with the protons oscillating together through the neutron mass. This phenomenon has been well characterized for many nuclei, with the center of the resonance often lying between 15-20 MeV [56]. The resonant nature of this oscillator results in a gamma strength characterized with a Lorentzian form like that shown in Equation 2.37 [25].

$$f_{Xl}(E_\gamma) = K_{Xl} \frac{\sigma_{Xl} E_\gamma \Gamma_{Xl}^2}{(E_\gamma^2 - E_{Xl}^2)^2 + E_\gamma^2 \Gamma_{Xl}^2}. \tag{2.37}$$

In this form σ_{Xl} is the strength, E_{Xl} is the center energy, and Γ_{Xl} is the width of the GDR. Note that primary contributor to the total gamma strength $f_{tot}(E_\gamma)$ is the f_{E1} component. This Lorentzian model was later expanded upon by Kopecky and Uhl to include a nuclear temperature correction for low energy E1 excitations [47]. This modified Lorentzian is

$$f_{E1}(E_\gamma, T) = K_{E1} \left(\frac{E_\gamma \tilde{\Gamma}_{E1}(E_\gamma)}{(E_\gamma^2 - E_{Xl}^2)^2 + E_\gamma^2 \tilde{\Gamma}_{E1}(E_\gamma)^2} + \frac{0.7 \Gamma_{E1} 4\pi^2 T^2}{E_{E1}^5} \right) \sigma_{E1} \Gamma_{E1}, \tag{2.38}$$

with the energy-dependent damping width $\tilde{\Gamma}_{E1}(E_\gamma)$ defined in Equation 2.39 [25]:

$$\tilde{\Gamma}_{E1}(E_\gamma) = \Gamma_{E1}\frac{E_\gamma^2 + 4\pi^2 T^2}{E_{E1}^2}. \tag{2.39}$$

Both of these definitions invoke the nuclear temperature T as defined by Kopecky et al., which introduces a non-zero temperature dependent gamma strength enhancement at low E_x, and provides an adjustable parameter for fitting experimentally observed values [57]:

$$T = \sqrt{\frac{E_n + S_n - \Delta - E_\gamma}{a(S_n)}}. \tag{2.40}$$

Note the inclusion of the pairing correction term Δ and the level density parameter a, as defined in Section 2.2, provides adjustable parameters to emulate pairing and shell effects. With implementation of this temperature correction factor, better agreement between calculated values and experimental values was found in spherical nuclei [57]. There have been further modifications to the Lorentzian model of gamma strength functions. One such modification was introduced by Goriely, who implemented a modified low energy correction in an effort to better match data in heavy nuclei, for the purpose of exploring r-process nucleosynthesis [58].

2.3.1.1 Double and Pygmy resonances

For the case of deformed nuclei, the GDR often displays a double-humped behavior gamma strength function that can be modelled using the sum of 2 Lorentzian distributions as shown in Equation 2.41 [59, 25]:

$$f_{E1}(E_\gamma) = \sum_{i=1}^{2} f_{E1}^i(E_\gamma, \sigma_{E1}^i, E_{E1}^i, \Gamma_{E1}^i). \tag{2.41}$$

Following extensive experimental and theoretical efforts, the presence of an enhanced $E1$ gamma strength has been noted below S_n in many nuclei [60]. This enhancement can be attributed to the presence of a Pygmy resonance, and can be modelled in a manner similar to Equation 2.41 [25].

2.3.2 Microscopic models for gamma strength functions

Similarly to the NLD models discussed prior, there have been extensive efforts in developing microscopic models for gamma strength functions. The first extensive set of calculated gamma strength functions was presented by Goriely and Khan, using a Skyrme-Hartree-Fock BCS with quasi-particle random phase approximation (QRPA) model [61]. Following the development of the microscopic NLD models, Goriely et al. provided tabulated values for calculations utilizing the Bogoliubov force and temperature dependent frameworks [62]. There are alternative microscopic models available in TALYS [25], but the primary focus of the work discussed later in this document is the Brink-Axel Lorentzian model.

2.4 Nuclear-Plasma Interactions

In most cases atomic transitions and nuclear transitions are treated separately due to their different energy scales. With atomic levels largely limited to the eV-keV range, there are few cases for energetic overlap when considering that nuclear levels predominantly exist within the 10's of keV to many MeV energy range. However, there are some nuclei that have very low lying excited states, such as the ^{229m}Th isomer discussed in Chapter 1 and the 78.6 eV isomeric state in ^{235}U [19, 63]. The latter of these isomers drove interest in exploring atomic-nuclear interactions.

The theory of nuclear excitation by electronic transition (NEET) was introduced by Morita in 1973 within the context of finding a novel method for the chemical separation of ^{235}U nuclei from bulk Uranium [64]. The NEET mechanism requires that the electron cloud of the nucleus in question be partially ionized. It is in this requirement that the term nuclear-plasma interactions (NPIs) arises. In the simplest case, a single electron is ionized and higher-lying electron de-excites to fill the vacancy. This de-excitation requires the release of energy in the form of a real or virtual photon to carry the change in atomic binding energy, ΔE_B. The release of a real photon with the energy ΔE_B is referred to as x-ray emission. Alternatively, a virtual photon can couple into a less bound electron, resulting in Auger emission. In place of these interactions, Morita presents a third alternative in which the virtual photon couples into the nucleus via an electromagnetic interaction, resulting in the population of an excited state. Following analysis of the hybrid atomic-nuclear wave functions as mediated by Coulombic interactions between atomic electrons and the nucleus, the calculated probability of the NEET mechanism populating the isomeric state in ^{235}U was determined to be $\approx 2 \times 10^{-9}$. Morita notes this probability is well below that of x-ray emission and Auger emission, but should be observable in experiments [64].

Experimental results published by Izawa and Yamanaka in 1979 reported successful observation of the NEET interaction in ^{235}U following repeated exposure to a 1 J, 100 ns laser. The authors reported an integrated reactivity $< \sigma_{NEET} v > \approx 10^{-20}$ cm^3 s^{-1}, or an estimated 1 isomer excitation per ^{235}U nucleus per second [65, 63]. Experiments by Arutyunan et al. using an electron beam for plasma generations reported a significantly lower isomer population rate of $< 10^{-5}/^{235}$U/s [66]. Using a much less intense laser than Izawa and Yamanaka, Bounds and Dyer reported an isomer population rate of $< 10^{-7}/^{235}$U/s [67]. The inconsistencies in these reported values was explored by Harston and Chemin, who re-contextualized these experiments within the framework of four possible nuclear-plasma interactions [63].

2.4.1 Nuclear excitation by electronic transition

Introduced prior, NEET is time-inverse of the bound internal conversion (BIC) decay mechanism exhibited by some nuclei. Within this framework, the NEET interaction is resonant when the atomic ΔE_B is very close to the excitation energy of a given state. The

excitation energy coupled into a ground state nucleus is

$$E_x = E_0 + \Delta E_B, \tag{2.42}$$

where E_0 is the ground state energy. This formalism can be used for excitations out of a lower lying excited state, by replacing this E_0 term with the appropriate energy. The resonance condition is satisfied when

$$E_{state} - E_0 = \Delta E_B + \delta, \tag{2.43}$$

where E_{state} is the excitation energy of a given state, and δ is an energy mismatch term which accounts for atomic level broadening in perturbed environments, such as in a plasma [68]. As investigated by Morita, the ^{235}U nucleus has two pertinent examples [64]. A direct excitation of the ground state into the 26 minute isomer would require an energy of ≈ 30 eV, which corresponds to the 29.7 eV electronic transition between the $6_{d3/2}$ and $6_{p3/2}$ orbitals. However, it was determined later that this isomer has an $E_x = 76$ eV [69]. The other case, deemed more probable by Morita, is the excitation of the 13.1 keV excited state followed by de-excitation into the isomer state. This initial E_x is close to the atomic $3_{d3/2} \rightarrow 2_{p3/2}$ transition with $\Delta E_B = 13.44$ keV [64]. Outside of these matched transitions, predicted NEET contributions are minimal. Modernized calculations by Harston and Chemin for the idealized theoretical NEET interaction rates in ^{235}U indicate a strong dependence on the plasma temperature, with a broad range of $10^{-9} < \lambda_{NEET} < 1$ s^{-1} representing the extremes as affected by reasonably achievable plasma temperatures of 20 keV and 100 keV [63]. A reassessment of the theoretical approach to calculating NEET interaction rates was later performed by Harston, with comparison to existing experimental data for ^{189}Os, ^{197}Au, and ^{237}Np nuclei. They find numerical agreement with prior assessments that predict low NEET interaction rates, with a maximum probability in ^{189}Os of $\approx 3.6 \times 10^{-8}$ [68].

2.4.2 Nuclear excitation by electron capture

As NEET is the inverse BIC decay, a similar analog was introduced for internal conversion (IC) decay by Goldanskii and Namiot [70]. The process known as nuclear excitation by electron capture (NEEC) can occur when the atom captures a free electron and couples the remaining energy into exciting the nucleus. This excitation energy coupled into a ground state nucleus is

$$E_x = E_0 + (E^e_{free} - E^e_B), \tag{2.44}$$

where E^e_{free} is the free electron's energy and E^e_B is the energy of the bound electron. The resonant excitation condition for NEEC is then

$$E_{state} - E_0 = E^e_{free} - E^e_B + \delta, \tag{2.45}$$

where the free electron's energy provides a looser constraint than that presented in Equation 2.43. This NEEC mechanism was later explored by Cue et al. within the context of heavy

ion beams capturing electrons from solid targets [71]. They predicted a NEEC rate $\approx 1000\times$ that of the NEET rate seen in comparable environments. The inherently increased number of available electron capture resonances would intuitively suggest a stronger NEEC contribution than compared to NEET, which requires strict energetic overlap between atomic and nuclear transitions. However, Chemin and Harston later calculated estimated NEEC rates for ^{235}U nuclei and found that NEEC rates should be $\approx 10^{-11}$ s^{-1}, a value significantly lower than their calculated NEET rates in the same conditions [63]. They found that the orbitals which dominate electron capture in various charge states of U atoms within the plasma environment did not satisfy the necessary resonance conditions for exciting the nucleus. The relative contributions of the NEEC and NEET mechanisms can vary in other nuclei as nuclear and atomic levels can differ in satsifaction of the stringent NEET resonance condition. Experimental results published in 2018 claimed the first observation of the NEEC mechanism in ^{93}Mo, but the strength of the NEEC contribution was later brought into question following analysis of experimental uncertainties with respect to photon background [72, 73].

2.4.3 Inelastic electron scattering

Sufficiently high energy electrons can undergo inelastic electron scattering (IES) with the nucleus through an electromagnetic interaction. In these scattering events, energetic electrons often excite collective states in nuclei, with the potential for inducing particle emission when excitation energies exceed threshold [74]. The excitation energy imparted to a ground state nucleus, E_x, can be determined by

$$E_x = E_0 + (E_i^e - E_f^e), \tag{2.46}$$

where E_i^e is the electron's initial energy and E_f^e is the electron's final energy. This process is well studied, and comprehensive reviews are available [74, 75]. In analyzing the NEET results published by Arutyunyan et al. using an electron beam induced plasma on ^{235}U, Harston and Chemin estimated an effective reaction rate of $\lambda_{IES} \approx 10^{-16}$ s^{-1}, well below that estimated for either NEET or NEEC contributions [66, 63].

2.4.4 Photo-excitation by Bremsstrahlung

The nucleus can absorb a photon and be excited into excited states, as discussed in Chapter 1. Within the realm of nuclear-plasma interactions, the presence of plasma electrons generates a bremsstrahlung background which acts as a source for photo-excitation of excited states. The excitation energy imparted into a ground state nucleus is

$$E_x = E_0 + E_\gamma, \tag{2.47}$$

where E_γ is the energy of the photon. Harston and Chemin analyzed the contributions from bremsstrahlung photo-excitation in the Arutyunyan et al. electron beam experiments [66] and the Izawa and Yamanaka [65] laser-plasma experiments. They found that contributions

from photo-excitation were similar in magnitude to those from IES, with a calculated $< 10^{-17}$ s^{-1} in the laser experiment and $< 10^{-7}$ s^{-1} in the electron beam experiment [63].

2.4.5 Modifications to isomer lifetime in plasmas

The presence of NPIs has an interesting effect on the lifetimes of isomeric states in nuclei. The enhanced decay of isomer states as function of environmental plasma temperature was explored by Gosselin and Morel as mediated by NPI mechanisms [76]. Of particular note is the enhanced decay of isomer states in nuclei where a favorable spin level is present right above the isomer state. When this level has a spin state with a preferential decay to levels below the isomer, per the single particle estimates discussed in Chapter 1, a significant enhancement in the effective decay rate of the isomer is expected. One example nuclei is ^{93}Mo, for which they calculate an enhanced decay rate $\approx 10^5 - 10^7\times$ that of the unperturbed isomer decay in plasma with temperatures $> 1keV$ [76]. The population into this next available state is mediated by NEEC and photo-excitation, which are moderated by their time reversed processes IC decay and gamma decay, respectively. This work was later expanded to include the contributions from NEET interactions in ^{93}Mo nuclei by Gosselin et al. [77]. In this work, the inclusion of the NEET mechanism further enhanced the decay rate of the isomer state, especially at plasma temperatures < 1 keV.

This affect has notable implications for astrophysical processes, as well as high-energy density experiments in the laboratory environment. The implications of modified isomer lifetimes in astrophysical settings have been explored, with interest in impacts on stellar nucleosynthesis, especially around $A \approx 80$ [9, 10]. Work by Misch et al. analyzed the impacts of isomer decay enhancement in stellar reaction rates as function of plasma temperature [11]. Misch et al. determined the presence of thermalization temperatures in the s-process, below which isomers must be treated uniquely due to sufficiently long lifetimes. Above these thermalization temperatures, NPI enhanced decay rates of isomers make them effectively indistinguishable from their base nuclei. Their extension of this analysis to r-process stellar nucleosynthesis determined that disparate lifetimes between isomers and ground states in neutron-rich nuclei could have significant impact on radioactive heating, and that these effect must be considered as the thermalization temperatures for relevant nuclei were above those expected in relevant stellar conditions [11].

The effect of NPI enhanced decay rates may be observable in experiments using short pulse high-intensity lasers to drive high-energy density environments. Of particular note is the extension of these effects to inertial confinement fusion experiments (ICF), which regularly drive high density interactions with plasma temperatures > 1 keV [78].

2.5 Coupling nuclear-plasma interactions into the quasicontinuum

The works pertaining to NPIs discussed thus far focus on low-lying states in heavy nuclei. Within this scope, the availability of resonant NEEC or NEET interactions is limited by both the atomic levels and low nuclear level densities for low E_x. In moving beyond this scope, it is necessary to determine how potential NPI rates can be increased. With modifications to the atomic level distribution already affected by the ionization state requisite of the plasma environment, it is then necessary to look at modifying the nuclear level density contribution to the resonance conditions.

As discussed earlier, nuclear level densities increase exponentially with E_x. The enhanced level density at high E_x presents a region which should provide significant enhancements to NEEC and NEET interaction rates. In the framework presented by this work, nuclei excited to high E_x find themselves surrounded with many states of similar energy and differing spin. If a nucleus can be excited and subjected to a plasma-like environment within the ns-fs lifetime of quasicontinuous states, a window for enhanced NPI rates exists [79]. This provides a novel concept for the induced population or depopulation of isomer states in nuclei. Optimized manipulation of isomer population in given nuclei following this scheme has several fundamental requirements. First, nuclear level density and gamma strength functions must be well characterized. Second, an understanding of the NEET and NEEC rates must be developed using these enhanced nuclear level densities with a complex analysis of the excitation and de-excitation pathways, as dictated by the gamma strength function. Third, a source for exciting and inducing these reactions in the laboratory environment must be determined. Chapter 3 of this work focuses on introducing and establishing laser-plasma accelerators as a novel source for experimental observation of NPIs. These sources can provide multi-MeV, < 100 fs electron or photon bunches at high repetition-rates, which we suggest can provide the necessary conditions for probing NPIs, nuclear level densities, and gamma strength functions in the nuclear quasicontinuum.

Chapter 3

Lasers, plasma, and laser-plasma accelerators

3.1 Gaussian laser pulse

In the laser-plasma accelerator (LPA) scheme, an intense laser pulse is required for driving plasma density structures. Typically, the ideal laser pulse is modelled as Gaussian in space and time. Adapting derivations presented by Träger et al. [80], the radially dependent electric field of a cylindrically symmetric, Gaussian laser pulse of wavelength λ which propagates along the z-axis is

$$E(r) = E_0 \exp\left(-\frac{r^2}{w^2(z)}\right), \tag{3.1}$$

where r is the radial distance from the center of the laser pulse and w the waist size defined as

$$w^2(z) = w_0^2\left[1 + \left(\frac{\lambda z}{\pi w_0^2}\right)^2\right], \tag{3.2}$$

with w_0 is the characteristic minimum waist at $z = 0$. The root mean square (RMS) of the laser intensity distribution is $w(z)/2$ for this Gaussian description with the standard deviation $\sigma = w/2$, given $I \propto |E|^2$. The longitudinal electric field evolution is

$$E(r,z) = E_0 \frac{w_0}{w(z)}\left(\frac{\sqrt{2}r}{w(z)}\right)^m L_l^m\left(\frac{2r^2}{w^2(z)}\right) \times e^{im\varphi} \exp\left[i\left(\Phi(z) + \frac{kr^2}{2R(z)}\right)\right], \tag{3.3}$$

where $k = 2\pi/\lambda$ is the wave number and L_l^m is the Laguerre polynomial dictated by the indices m and l, which can be adjusted to represent different spatial modes of the laser. The remaining expressions for $\Phi(z)$ and $R(z)$ are defined as

$$\Phi(z) = -(2l + m + 1)\tan^{-1}\left(\frac{z - z_0}{z_R}\right), \tag{3.4}$$

$$R(z) = z\left(1 + \frac{z_R^2}{z^2}\right), \tag{3.5}$$

where the Rayleigh range, z_R, is invoked. The Rayleigh range, defined as $z_R = \pi w_0^2/\lambda$ represents a beam evolution parameter which determines the distance from focus at which radial size of the beam has increased by a factor of $\sqrt{2}$ [80]. Together these expressions form a generalized definition for a Gaussian laser pulse. For the ideal case of a fundamental Gaussian mode with $l = m = 0$, assuming $z_0 = 0$, the electric field can be simplified to

$$E(r,z) = E_0 \frac{w_0}{w(z)} \exp\left(\frac{-r^2}{w^2(z)}\right) \exp\left(i\left[kz - \tan^{-1}\left(\frac{z}{z_R}\right) + \frac{kr^2}{2R(z)}\right]\right), \tag{3.6}$$

which contains information of the electric field's magnitude and phase evolution. The electric field as a function of r and integer steps of z_R is plotted in Figure 3.1. Moving out of focus with increasing z, the electric field amplitude decreases and widens radially r. The physical consequences of this are apparent when examining the resulting intensity distribution, as $I \propto |E|^2$, shown in Figure 3.2. At focus, the intensity is maximized and decreases rapidly with increasing r. At $z = z_R$, the peak intensity is halved, and is flatter along r.

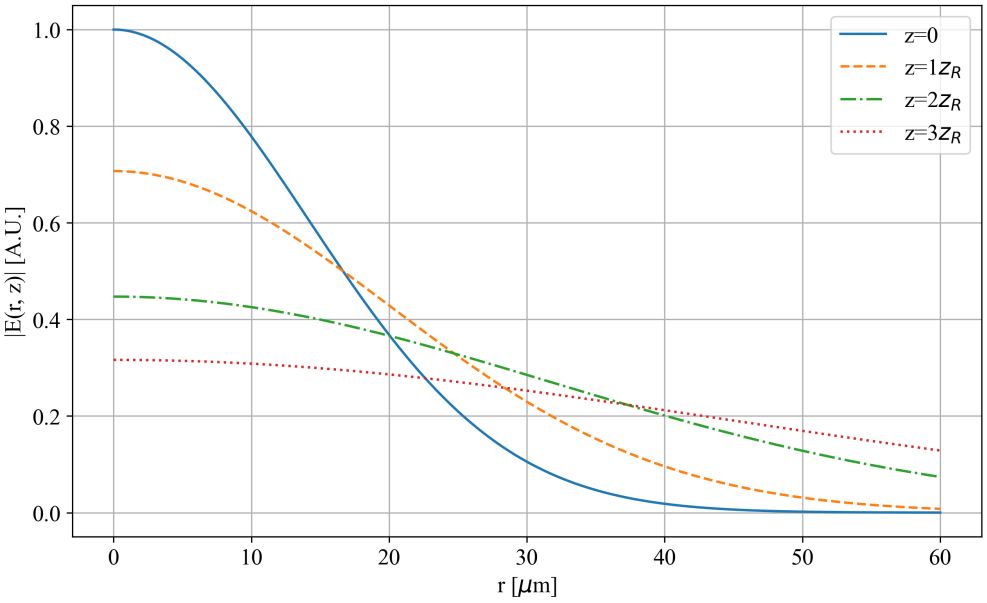

Figure 3.1: Gaussian electric field radial dependence plotted at multiple z for w_0 =20 μm and λ=800 nm.

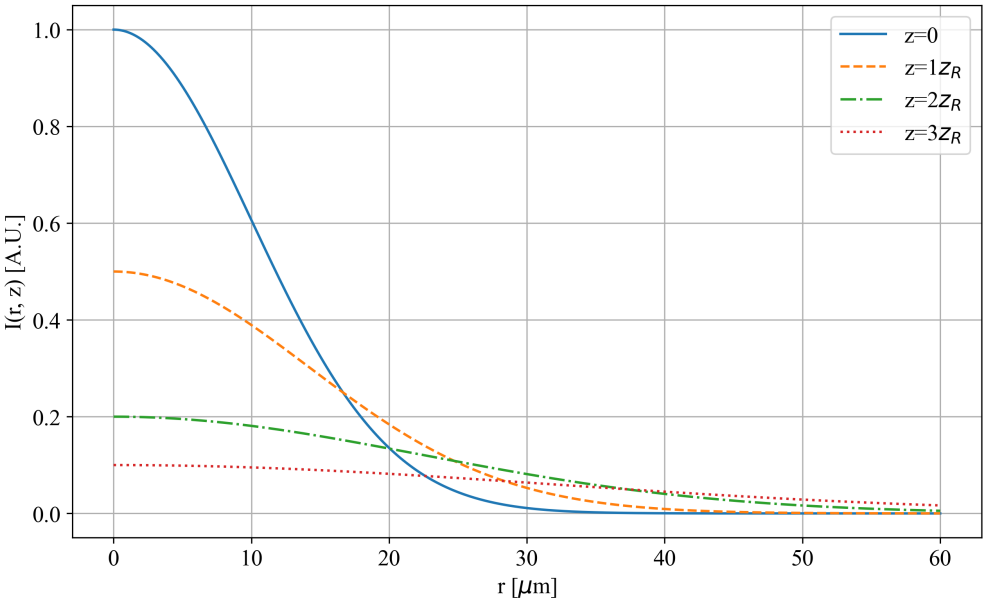

Figure 3.2: Intensity distribution resulting from a Gaussian electric field radial dependence plotted at multiple z for w_0 =20 μm and λ=800 nm.

Equation 3.6 is a useful expression for understanding the electric field evolution for a single wavelength, however, ultra-short laser pulses require broad spectral distributions. In a form similar to the uncertainty principle presented in Equation 1.4 relating nuclear state lifetimes and state energy widths, the relation for a coherent wave packet assuming a Gaussian shape with optical frequency full-width half maximum $\Delta\nu$ and FWHM temporal duration $\Delta\tau$ is

$$\Delta\nu\Delta\tau \geq 0.441, \tag{3.7}$$

which defines the bandwidth limits for ultrashort laser pulses [80]. For a 40 femtosecond Gaussian laser pulse centered at 800 nm, commonly used for driving LPAs, Equation 3.7 suggests a minimum bandwidth FWHM of 11.03 THz, or a wavelength FWHM of 23.5 nm. With this in mind, it is necessary to then to model the laser envelope, independent of specific wavelengths. The electric field strength of the laser envelope can be modelled as

$$E(t) = A(t)\cos\left(\Phi_0 + \omega_0 t\right), \tag{3.8}$$

where $A(t)$ is the envelope function multiplied by a harmonic wave function of the carrier frequency ω_0, which can be assigned to the center wavelength of the pulse [80]. The Φ_0 term is referred to as the carrier-envelope phase, and it determines the relationship between the peak electric field of the envelope and that of the carrier frequency oscillation. For $A(t)$ which vary slowly relative to the oscillation time of the carrier frequency, this phase term is less relevant. For the systems discussed in this work, laser pulses with a FWHM duration of

$\Delta t_{FWHM} \approx 40$ fs centered at 800 nm, the oscillation time of 2.67 fs is small relative to the total pulse duration. For a Gaussian pulse the temporal intensity evolution is related to the electric field envelope function by

$$I(t) = \frac{1}{2} nc\epsilon_0 A(t)^2, \tag{3.9}$$

where n is the index of refraction, c is the speed of light, and ϵ_0 is the vacuum permittivity. Assuming a Gaussian intensity function of the form

$$I(t) = I_0 \exp\left(-2\frac{(t-t_0)^2}{\sigma^2}\right), \tag{3.10}$$

where σ is the standard deviation of the electric field proportional to Δt_{FWHM} by

$$\Delta t_{FWHM} = 2\sqrt{2\ln(2)}\sigma, \tag{3.11}$$

the envelope electric field in Equation 3.8 can be computed. The normalized electric field envelope is plotted with the carrier frequency oscillations in Figure 3.3 for a laser pulse with $\Delta t_{FWHM} = 40$ fs and carrier wavelength of 800 nm.

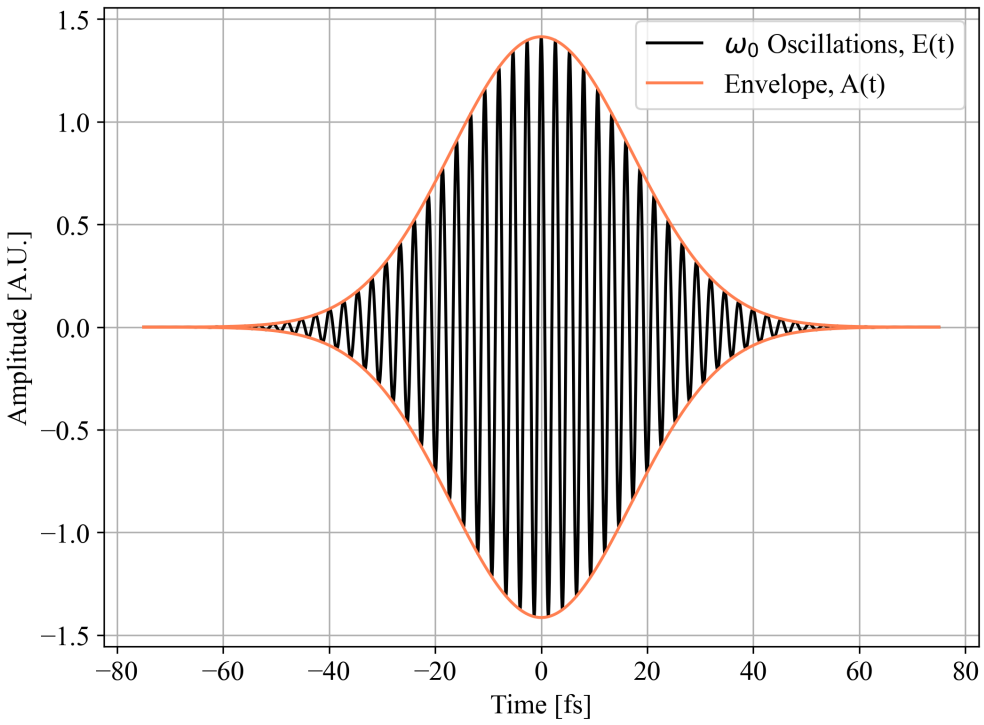

Figure 3.3: Electric field envelope plotted against the carrier frequency oscillations for a Gaussian laser pulse with $\omega_0 = 2.36$ rad/fs and $\Delta t_{FWHM} = 40$ fs.

In discussing intense laser pulses in the context of laser-plasma interactions, it is useful to introduce a normalized coefficient for comparison [81]. The peak laser strength parameter a_0 is defined for a linearly polarized field as

$$a_0 = \frac{e\vec{A}}{m_e c^2} \simeq \frac{e\vec{E}}{\omega m_e c}, \tag{3.12}$$

which results in a unit-less value accounting for the laser field strength and frequency. Here the laser vector potential $\vec{A}$ is introduced as an alternative method for representing the electric field defined as $\vec{E} = -\partial\vec{A}/\partial ct$ [81]. The physical interpretation of this parameter is simple, taken as the ratio of an electron's transverse momentum, as driven by the laser field, to its rest mass energy. For $a_0 \approx 1$ or greater, the electron motion is relativistic and requires treatment as such. In keeping with Gaussian laser pulses, a_0 is related to the peak laser intensity, I_0, by

$$a_0^2 \approx 7.3 \cdot 10^{-19} (\lambda[\mu m])^2 I_0 \left[\frac{W}{cm^2}\right], \tag{3.13}$$

with a dependence on laser wavelength.

3.2 Plasma fundamentals

Before discussing the mechanisms behind laser-plasma accelerators, it is necessary to discuss the fundamental characteristics of plasma. Consisting of charged particles whose behavior is dictated by collective electromagnetic interactions, the plasma state requires that the potential energy between two adjacent particles is significantly less than their kinetic energy. This constraint is necessary such that collective effects dominate over single particle interactions. For example, in a system of ionized Hydrogen atoms, the electrons must remain energetic enough to, on average, remain unbound to the positively charged nuclei. If the electron population's energy is insufficient to remain unbound, then neutral gas atoms will form and the collective electromagnetic effects that define the plasma state cannot occur.

Following discussions by Kruer and Fitzpatrick [82, 83], a system of charged particles will consist of a superposition of the electric fields generated between all particles. For the purpose of modelling such systems, this is prohibitively expensive. It is then necessary to characterize the distance at which the influence of a single charged particle is effectively shielded from the bulk, due to the response of other, nearby charged particles. Consider a positive charge q placed into a uniform plasma environment consisting of static ions and mobile electrons. In solving for the electrostatic potential of the charge q in the presence of mobile electrons, the range at which this potential is mitigated can be found. This range is called the Debye length and is defined as

$$\lambda_D = \sqrt{\frac{k_b T_e}{4\pi n e^2}}, \tag{3.14}$$

where n is the density of mobile electrons, e is the elementary charge, and k_b is Boltzmann's constant. This definition also invokes the electron temperature T_e, which refers to the thermodynamic temperature that defines the Maxwell-Boltzmann distributions often utilized in plasma physics. Note the use of CGS units which will remain consistent through Sections 3.2 and 3.3, which simplifies handling of the discussed equations. Equation 3.14 can be recast in the form of

$$\lambda_D = \frac{v_{Te}}{\omega_{pe}}, \tag{3.15}$$

where v_{Te} is the electron mean thermal defined as $v_{Te} = \sqrt{k_b T_e / m_e}$, and ω_p is the plasma frequency. The plasma frequency is fundamental parameter for plasma, and is defined as

$$\omega_p = \sqrt{\frac{4\pi n_i Z_i^2 e^2}{m_i}}, \tag{3.16}$$

where m_i is the mass, n_i is the density, and Z_i is the charge state of species i in the plasma. These dependencies require that different species will behave on different time scales. For the case of electrons, this expression becomes

$$\omega_{pe} = \sqrt{\frac{4\pi n e^2}{m_e}}, \tag{3.17}$$

where m_e is the mass of the electron. The electron plasma frequency often corresponds to the fastest collective behavior in a plasma system, mediated by the low-mass electrons. The plasma period, reciprocal of the electron plasma frequency, is defined as

$$\tau_{pe} = \frac{2\pi}{\omega_{pe}}. \tag{3.18}$$

Together, τ_{pe} and λ_D are the minimum temporal and spatial parameters for which interactions can be attributed to plasma behavior. Examples of plasma behavior which satisfy these conditions can occur in response to internally generated electromagnetic fields, thermalizing collisions between both like and dissimilar species, and influence from external electromagnetic fields [82, 83]. From these equations it can be noted that understanding a plasma system requires characterizing the plasma temperature and density, as together these properties dictate the fundamental interactions that occur within the plasma.

3.2.1 Modelling plasma behavior

In beginning to model bulk plasma behavior, tracking all individual particles is a logical, if not difficult, starting point. As presented by Kruer [82], the Vlasov equation details the evolution of the particle distribution in phase space, $f_i(\vec{x}, \vec{p}, t)$, for species i. This distribution

encompasses the evolution of the phase space density. Assuming no destruction or introduction of particles in the plasma, applying the continuity equation and relativistic equations of motion for charged particles yields the Vlasov equation,

$$\frac{\partial f_i}{\partial t} + \frac{\vec{p}c}{\gamma} \cdot \nabla_{\vec{x}} f_i + \frac{d\vec{p}}{dt} \cdot \nabla_{\vec{p}} f_s = 0, \tag{3.19}$$

with

$$\frac{d\vec{p}}{dt} = \frac{q_s}{m_s c} \left[\vec{E}(\vec{x}) + \frac{\vec{p}}{\gamma} \times \vec{B}(\vec{x}) \right], \tag{3.20}$$

where $f_i(\vec{x}, \vec{p}, t)$ evolves with time as the result of the plasma's momentum, spatial distribution, and responses to electric, $\vec{E}$, and magnetic, $\vec{B}$, fields. Here $\vec{p} = \gamma\vec{v}/c$ is the relativistic momentum for velocity $\vec{v}$ and Lorentz factor $\gamma = (1 + p^2)^{1/2}$. When coupled with Maxwell's equations, the Vlasov equation allows one to track the temporal evolution of a smooth $f_i(\vec{x}, \vec{p}, t)$ distribution function, detailing the collective behavior of a collionless plasma. Full evolution of the 6D phase space distribution is not necessary for understanding many behaviors observed in plasma, leading to the need for alternative approaches. One such approach requires taking moments of the Vlasov equation with respect to momentum, in an effort to construct a fluid model for each species in a plasma. The first two moments are

$$n_i = \int f_i d\vec{p}, \tag{3.21}$$

$$n_i \vec{u}_i = \int \vec{p} f_i d\vec{p}, \tag{3.22}$$

where n is the number density and $\vec{u}_i$ is the fluid momentum. In the regime of laser-plasma accelerators, where the mean electron plasma momentum is relativistic with a temperature spread on the order of the ionization potential in gas, ≈ 10 eV, a cold plasma approximation is useful in providing closure for the moments of the Vlasov equation. In this approximation, the plasma phase space distribution can be treated as

$$f_i\left(\vec{x}, \vec{p}, t\right) = n_i(\vec{x}) \delta(\vec{p} - \vec{u}_i), \tag{3.23}$$

which treats the plasma electron distribution as singly energetic. Note that a warm, relativistic plasma model can be utilized, and has been developed by Schroeder and Esarey [84]. Taking the moments of the Vlasov equation using this distribution yields the cold plasma fluid equations. The first result of this process is the fluid continuity equation,

$$\frac{\partial n}{\partial ct} + \nabla \cdot \frac{n\vec{u}}{\gamma} = 0 \tag{3.24}$$

where $\gamma = (1 + u^2)^{1/2}$ is the Lorentz factor for the fluid momentum. This equation details the temporal evolution of the density of the bulk fluid, n, as a function of the relativistic fluid momentum. Note, the species indicator i has been dropped, as the focus is placed on

the plasma electron fluid most relevant to laser-plasma accelerator dynamics. The second result is the fluid momentum equation,

$$\frac{\partial \vec{u}}{\partial ct} + \frac{\vec{u}}{\gamma}\nabla_x \cdot \vec{u} = \frac{q}{mc^2}\left[\vec{E}(\vec{x}) + \frac{\vec{u}}{\gamma} \times \vec{B}(\vec{x})\right] \tag{3.25}$$

which details the temporal evolution of the fluid accounting for bulk flow and electromagnetic fields.

As a result of the cold plasma distribution assumed in Equation 3.23, a plasma-pressure term is missing from Equation 3.25, which invokes the next moment of the Vlasov equation. Truncation of these successive moment dependencies is necessary, and can be treated with assumptions on the thermal behavior of the plasma fluid. In treating the pressure term, there are two limits to evaluate. Consider a wave-like phenomena with a characteristic frequency ω and wave number k. In the case where $\omega/k << v_{Ti}$, in which the phenomena to be evaluated moves much slower than the thermal velocity of the species i. In this limit, the plasma thermalizes at a rate much faster than propagation of the wave, meaning temperature difference effects can be neglected. The isothermal equation of state,

$$p_i = n_i T_i, \tag{3.26}$$

provides a valid solution for the pressure term in this limit, as it states that the pressure in a plasma species i is directly a function of its density and constant temperature. Or simply, the pressure term in Equation 3.25 becomes directly proportional to changes in the density distribution of the plasma. The second limit evaluates the opposite case where $\omega/k >> v_{Ti}$, in which the wave propagates through the plasma faster than the plasma can thermalize. The adiabatic equation of state,

$$p_i = K n_i^{\varrho}, \tag{3.27}$$

where K is a constant, and $\varrho = (2+N)/N$ with N the number of degrees of freedom in the system. For the laser-plasma interactions discussed later, the $\omega/k << v_{Ti}$ limit is never valid, as the plasma waves have a phase velocity of approximately c. For these interactions where the frequency of electron thermal collisions is significantly lower than ω_{pe}, a 1D adiabatic compression of the plasma electron density is assumed, as thermal motion cannot couple the plasma wave motion into other dimensions. Physically, the electron velocity driven by the plasma wave is much greater than thermal motion, and the plasma-pressure term can be neglected, which truncates the moments required. This cold plasma assumption is critical in obtaining closure of the fluid equations.

Together, the Vlasov equation or the fluid equations, supplemented by Maxwell's equations, provide a description of plasma behavior each through distinct lens. The Vlasov equation provides a particle phase space distribution model of plasma behavior. This approach is necessary for analyzing behaviors resulting from phase space distribution perturbations, and cases where kinetic interactions are of interest. However, this approach is computationally expensive and unnecessarily detailed for bulk plasma behavior. In the other case, the fluid model treats each species of the plasma as a bulk fluid, and provides insight into

collective phenomena without detailed consideration for kinetic effects. This fluid approach will provide the framework for discussing laser-plasma interactions in the next section.

3.2.2 Electromagnetic waves in a plasma

The response of the bulk plasma to the presence of an external electric field is critical to understanding the behavior of a laser pulse propagating through plasma. From derivations presented by Kruer [82], the simplest case is that of a non-magnetized, neutral plasma in the presence of an oscillatory electric field

$$\vec{E}(\vec{x},t) = \vec{E}(\vec{x})\exp(-i\omega t), \tag{3.28}$$

with $\omega > \omega_{pe}$ assumed. This assumption allows for treatment of the ions as a stationary background, due to the mass dependency in Equation 3.16. The motion of the electron fluid in the presence of oscillatory electric field can be analyzed using Maxwell's equations, yielding the dispersion relation

$$\omega^2 = \omega_{pe}^2 + c^2k^2, \tag{3.29}$$

which reveals a critical condition for the propagation of $\vec{E}(\vec{x},t)$ in a plasma. For $\omega > \omega_{pe}$, the wave number k remains real, indicating that the electromagnetic wave can pass through the plasma. In this case, the electron fluid cannot move quickly enough to hamper the wave. However, for $\omega < \omega_{pe}$, k becomes imaginary, indicating that the wave will reflect or attenuate. In this scenario, the electron fluid can move quick enough to shield the wave and hinder its propagation. Recalling Equation 3.17, the critical density, n_{crit}, can be solved for a given wavelength of light by setting $\omega^2 = \omega_{pe}^2$. The resulting expression,

$$n_{crit} = \frac{1}{\lambda^2}(2\pi c)^2\frac{\epsilon_0 m_e}{e^2} \approx \frac{1.12\cdot 10^{21}}{\lambda[\mu m]^2}\left[\frac{\#}{cm^3}\right], \tag{3.30}$$

is useful for determining the critical density for a given wavelength of light. For a laser with $\lambda = 800$ nm, $n_{crit} \approx 1.75\cdot 10^{21}$ cm^{-3}.

3.2.3 Intense laser pulses in plasma

Moving beyond the simple case presented above, it is crucial to consider the response of a plasma to the presence of an intense, spatially dependent laser pulse. Following Kruer [82], the response of an electron fluid to spatially varying electric field, $\vec{E}(\vec{x},t) = \vec{E}\sin(\omega t)$ for $\omega > \omega_{pe}$, can be examined using a nonrelativistic fluid momentum equation. By averaging over rapid oscillations in the electric field and accounting for up to 2nd order contributions from $\vec{E}$, the force equation becomes

$$m_e\frac{\partial \vec{u^s}}{\partial t} = -e\vec{E^s} - \frac{e^2}{4m_e\omega^2}\nabla\vec{E}^2(\vec{x}), \tag{3.31}$$

in which two distinct terms arise. This treatment of averaged motion is the envelope approximation. The first term, $e\vec{E}^s$, is simple oscillatory motion of the electrons over in the electric field which cancels out due to sinusoidal nature of the electric field oscillations. Dropping this leaves the second term known as the ponderomotive force, highlighted in Equation 3.32, which acts to push the electron fluid away from gradients of increasing intensity.

$$\vec{F}_{pond} = -\frac{e^2}{4m_e\omega^2}\nabla\vec{E}^2(\vec{x}). \tag{3.32}$$

This expression can be restated in a form conducive for interpretation of applications involving high-intensity lasers. By inserting the laser strength parameter as defined in Equation 3.12, the ponderomotive force can be read as

$$F_{pond} = -\frac{m_e c^2}{4}\nabla a^2. \tag{3.33}$$

These expressions give the linear limit ($a_0 << 1$) for the ponderomotive force, and represent the fundamental interaction which enables laser-plasma acceleration schemes [82, 81]. A more rigorous derivation can be performed using the relativistic cold plasma model in Equation 3.25, which yields

$$\left(\frac{\partial^2}{\partial t^2} + \omega_{pe}^2\right)\frac{\delta n}{n_0} = \frac{c^2}{2}\nabla^2 a^2, \tag{3.34}$$

$$\left(\frac{\partial^2}{\partial t^2} + \omega_{pe}^2\right)\frac{\vec{E}}{E_0} = -\frac{\omega_{pe}c}{2}\nabla a^2, \tag{3.35}$$

where the electron plasma density perturbation, δn, and resultant electric field, $\vec{E}$, are driven by the ponderomotive force.

3.3 Laser-plasma accelerators

3.3.1 Linear plasma waves

Originally proposed by Tajima and Dawson in 1979, the laser-plasma accelerator (LPA) concept has since seen significant development in both theory and experiment [85]. This initial work suggests utilizing high intensity lasers to drive electron density perturbations in a plasma. These perturbations result in the formation of strong electric fields, theoretically many times stronger than those sustained by traditional accelerator cavities [81]. With 100 MeV/m formerly a significant technical target for RF cavity accelerators, and recent experimental cavities reaching up to 200 MeV/m, the observed $\approx$ 100 GeV/m accelerating fields in LPAs represents an exciting new regime for accelerator physics [86, 87, 81]. Derived by Dawson [88], the cold nonrelativistic plasma wave-breaking field limit,

$$E_0\left[\frac{V}{m}\right] = \frac{cm_e\omega_{pe}}{e} \simeq 96\sqrt{n_0[cm^{-3}]}, \tag{3.36}$$

where n_0 is the unperturbed electron plasma density, gives insight into the strong accelerating fields that LPAs can generate. Physically, this can be derived by examining the electric field produced by two infinite sheets of charged particles with charge density n_0 separated by the plasma skin depth, c/ω_{pe}. With one sheet consisting of positive immobile ions and the other electrons, an electric field representative of that supported by electron plasma waves is generated. Using Poisson's equation in 1D, $E = 4\pi e n_0 c/\omega_{pe}$ is found, and can be rearranged to yield Equation 3.36. For a readily achievable $n_0 \approx 10^{18}$ cm^{-3}, accelerating gradients near 100 GeV/m are expected. These fields are formed following electron density perturbations driven by the ponderomotive force. Using the fluid equations these density perturbations, $\delta n/n_0 = (n-n_0)/n_0$, can be modelled in the $a_0^2 << 1$ limit with the following set of equations,

$$\left(\frac{\partial^2}{\partial t^2} + \omega_{pe}^2\right)\frac{\delta n}{n_0} = \frac{c^2}{2}\nabla^2 a^2, \tag{3.37}$$

$$\left(\frac{\partial^2}{\partial t^2} + \omega_{pe}^2\right)\phi = \frac{\omega_{pe}^2 a^2}{2}, \tag{3.38}$$

where $\phi = e\Phi/m_e c^2$ is normalized electrostatic potential in the wake formed by the laser pulse and n is the perturbed electron density [81, 89, 90]. Examination of Equation 3.37 is instructive, as the time evolution of the density perturbation on the left-hand side is directly driven by the ponderomotive force term on the right-hand side. Note the laser strength parameter a has dropped the a_0 subscript, as the time evolution term in Equations 3.37 and 3.38 requires consideration of the evolving laser strength parameter with temporal envelope of the laser. Assuming $|\delta n/n_0 << 1|$, the 3D electric field and density perturbations can be solved in the form

$$\frac{\delta n}{n_0} = \frac{c^2}{2\omega_{pe}}\int_0^t dt' \sin\left(\omega_{pe}(t-t')\right)\nabla^2 a^2(\vec{r},t'), \tag{3.39}$$

$$\frac{\vec{E}}{E_0} = -\frac{c}{2}\int_0^t dt' \sin\left(\omega_{pe}(t-t')\right)\nabla a^2(\vec{r},t'), \tag{3.40}$$

which is valid for $E/E_0 << 1$. Examination of these equations reveal that, perhaps intuitively, wakefield formation is most effective when the laser intensity profile evolves on a scale length which is roughly matched to the characteristic plasma wave length, $\lambda_{pe} = 2\pi c/\omega_{pe}$ [81]. An electron beam can be injected, or background electrons can become "trapped" in this wake structure, and accelerated by the longitudinal electric fields along the propagation path of the laser pulse.

In addition to the longitudinal electric fields that are formed, there are axial electric fields, E_r, and rotational magnetic fields, B_θ that are related to the longitudinal fields by the Panofsky-Wenzel Theorem [91, 81]. These fields are related by the expression

$$\frac{\partial E_z}{\partial r} = \frac{\partial\left(E_r - B_\theta\right)}{\partial\left(z-ct\right)}, \tag{3.41}$$

which will be revisited shortly. To understand the behavior of the behavior of these systems, apply a Gaussian laser pulse with

$$a^2 = a_0^2 \exp\left(-2\frac{r^2}{r_0^2}\right) \sin^2\left(\frac{k_{pe}}{2}(z - v_g t)\right), \tag{3.42}$$

to Equations 3.39 and 3.40 where z is the longitudinal coordinate, r is the radial coordinate, r_0 is characteristic radial width of the laser, $v_g = c(1 - \omega_{pe}^2/\omega^2)^{1/2} \approx c$ is the group velocity of the laser pulse in the plasma in the 1D linear limit, and $k_{pe} = 2\pi/\lambda_{pe}$. Introducing the co-moving coordinate frame, $\zeta = z - v_g t$, the solutions to these equations are [81]

$$\frac{\delta n}{n_0} = -\frac{\pi}{4} a_0^2 \left(1 + \frac{8}{k_{pe}^2 r_0^2}\left(1 - 2\frac{r^2}{r_0^2}\right)\right) \exp\left(-2\frac{r^2}{r_0^2}\right) \sin\left(k_{pe}\zeta\right), \tag{3.43}$$

$$\frac{E_z}{E_0} = -\frac{\pi}{4} a_0^2 \exp\left(-2\frac{r^2}{r_0^2}\right) \cos\left(k_{pe}\zeta\right). \tag{3.44}$$

Additionally, an expression for ϕ can be calculated by the relation $-\partial_\zeta \phi = E_z/E_0$, which yields

$$\phi = \frac{\pi}{4k_{pe}} a_0^2 \exp\left(-2\frac{r^2}{r_0^2}\right) \sin\left(k_{pe}\zeta\right). \tag{3.45}$$

Sinusoidal fluctuations in electron density and the longitudinal electric field are observed, with an inherent $\pi/2$ phase shift. The plasma waves propagate in the direction of the laser pulse with a phase velocity v_p roughly matched to the laser pulse, which travels through the plasma with a group velocity $v_g \approx c$. This behavior is shown in Figure 3.4, and compared to non-linear wakefield behavior. For the same laser pulse, the transverse wakefield component, $W_r = E_r - B_\theta$, is [92, 91, 81]

$$\frac{W_r(r,\zeta)}{E_0} \approx a_0^2 \frac{\pi}{4} \frac{4r}{k_{pe} r_0^2} \exp\left(-2\frac{r^2}{r_0^2}\right) \sin\left(k_{pe}\zeta\right), \tag{3.46}$$

which introduces a $\pi/2$ shift relative to the longitudinal accelerating field. This shift leads to a $\pi/2$ phase region where trapped relativistic electrons are accelerated and focused.

One key limiting factor for the acceleration of trapped electron bunches is the result of de-phasing between the electron bunch and the plasma wave. Trapped electrons can accelerate to a velocity which outpaces the phase velocity of the wakefield. When this occurs the electron can witness an electric field of the opposite polarity, leading to slowing and potentially broadening the energy spread of the electron bunch. The de-phasing length, L_D, can be approximated in the 1D linear limit as

$$(1 - \frac{v_g}{c}) k_{pe} L_D = \frac{\pi}{2}, \tag{3.47}$$

$$L_D \approx \frac{\lambda_{pe}^3}{2\lambda}, \tag{3.48}$$

which upon examination using the definition of ω_{pe} in Equation 3.17, reveals a scaling factor with electron density of $L_D \propto n_0^{-3/2}$ [81]. Higher density plasma will result in shorter dephasing lengths. This ultimately needs to be balanced with the wakefield longitudinal electric field strength, which scales as $E_0 \propto n_0^{1/2}$, with higher density plasma allowing for stronger electric fields. The net energy gain of an electron can be found by integrating Equation 3.44 over the accelerating and focusing phase of $\pi/2$ for $r = 0$. After invoking the definitions of E_0 and k_{pe}, this expression becomes

$$\Delta\gamma = \frac{\pi}{4} a_0^2, \tag{3.49}$$

where $\sin(k_{pe}\pi/2) = 1$. In the linear plasma wave limit, increasing a_0 leads to increased electron energy gain.

One of the unique characteristics of LPAs is the inherently short beam durations which are created. This arises from the plasma nature of the scheme. For a wake of the characteristic length λ_{pe}, the temporal duration of an electron bunch accelerated within the wake,

$$\tau_b < \frac{\lambda_{pe}}{c}, \tag{3.50}$$

is inherently ultra-short. For a plasma with $n_0 \approx 10^{18}$ cm^{-3}, bunches with $\tau_b < 100$ fs are expected. The ultra-short nature of these pulses enables probing of short-lived nuclear states, and provides the opportunity for exploring nuclear-plasma interactions in nuclei excited to the quasicontinuum.

3.3.2 Non-linear plasma waves

For cases where $a_0^2 \geq 1$, the electron motion is relativistic, leading to modifications in expected wakefield behavior. In this non-linear regime, the cold plasma wave-breaking limit can be exceeded, resulting in $E > E_0$. Modelling 1D behavior of non-linear plasma waves in the presence of static ions can be accomplished using cold relativistic plasma fluid equations, [81, 93, 94]. The continuity and momentum equations are given as

$$\frac{\partial n}{\partial t} + c\frac{\partial n\beta}{\partial z} = 0, \tag{3.51}$$

$$\frac{d(\gamma\beta)}{dt} = c\frac{\partial \phi}{\partial z} - \frac{c}{2\gamma}\frac{\partial a^2}{\partial z}, \tag{3.52}$$

which provide a generalized function for non-linear plasma waves along the longitudinal z-axis. In using these equations, a set of relativistic factors are useful.

$$\begin{aligned} \beta &= \frac{v_z}{c}, \\ \beta_\perp &= \frac{v_\perp}{c} = \frac{a}{\gamma}, \\ \gamma &= \frac{1}{\sqrt{(1-\beta^2-\beta_\perp^2)}}. \end{aligned} \tag{3.53}$$

This set of equations defines the longitudinal and transverse velocity normalizations, β and $\beta_\perp$, respectively, with $\beta_\perp = a/\gamma$ describing the quiver motion of the electron in the laser field. The Lorentz factor is defined such that it accounts for both longitudinal and transverse momentum. The cold fluid equations can be shifted into a co-moving frame with the variables $\xi = z - v_p t$ and $\tau = t$ in the form [94]

$$\frac{\partial \left(n(\beta_p - \beta)\right)}{\partial \xi} = \frac{\partial (n/c)}{\partial \tau}, \tag{3.54}$$

$$\frac{\partial \left(\gamma(1 - \beta_p \beta) - \phi\right)}{\partial \xi} = -\frac{1}{c}\frac{\partial (\gamma\beta)}{\partial \tau}, \tag{3.55}$$

where $\beta_p = v_p/c$ is the normalized phase velocity in the shifted frame. These are complemented by Poisson's equation in the form

$$\frac{\partial^2 \phi}{\partial \xi^2} = k_{pe}^2 \left(\frac{n}{n_0} - 1\right). \tag{3.56}$$

Here the evolution of the electric potential is directly related to the density fluctuations of the electron plasma.

In analyzing 1D non-linear plasma wave evolution, the quasi-static approximation can be applied to simplify the forms of Equations 3.54 and 3.55. Extending upon envelope approximation, this approximation is valid when the laser pulse duration is treated as much shorter than the timescale on which the laser envelope is modified due to the presence of the plasma electrons. This approach allows the electrons to respond to a "static" laser envelope. Additionally, the laser spot size must be much greater than the characteristic length of the plasma waves, λ_{pe}. In this framework, assuming $\gamma_p^2 >> 1$ where γ_p is the Lorentz factor for the phase velocity of the plasma wave, the Poisson equation and plasma electrons can be treated as a set of observable quantities n, u_z, β_z evolving around ξ [94, 93, 81]. The Poisson equation in this form is given as

$$\frac{\partial^2 \phi}{\partial \xi^2} = \frac{k_p^2}{2}\left(\frac{(1 + a^2)}{(1 + \phi)^2} - 1\right), \tag{3.57}$$

which details the evolution of the wakefield potential as a result of the plasma responding to the passing laser envelope a. The longitudinal electric field, E_z, is related to the potential by

$$E_z = -E_0 \frac{\partial \phi}{\partial \xi} \tag{3.58}$$

The electron density, n, fluid longitudinal velocity u_z, and β_z are given in the following set of equations as

$$\frac{n}{n_0} = \frac{1 + a^2 + (1 + \phi)^2}{2(1 + \phi)^2}, \tag{3.59}$$

$$u_z = \frac{1 + a^2 - (1+\phi)^2}{2(1+\phi)^2}, \tag{3.60}$$

$$\beta_z = \frac{1 + a^2 - (1+\phi)^2}{1 + a^2 + (1+\phi)^2}, \tag{3.61}$$

which details the behavior of plasma electrons as influenced by the passing laser pulse. These equations are discussed later with numerical solutions for multiple a_0.

Another key characteristic of non-linear plasma waves is the elongation of the plasma wavelength, increasing relative to the fundamental λ_{pe}. This elongated wavelength, λ_{Npe}, is broken into two regimes,

$$\lambda_{Npe} = \lambda_{pe} \begin{cases} 1 + \frac{3}{16}\left(\frac{E_{max}}{E_0}\right)^2 & \text{if } \frac{E_{max}}{E_0} << 1 \\ \frac{2}{\pi}\left(\frac{E_{max}}{E_0} + \frac{E_0}{E_{max}}\right) & \text{if } \frac{E_{max}}{E_0} >> 1, \end{cases} \tag{3.62}$$

where E_{max} is the peak electric field sustained by the non-linear plasma wave [81]. In the non-linear regime the longitudinal electric fields generated can exceed E_0 by many factors. This cold relativistic wave-breaking field limit is given as

$$E_{WB} = E_0\sqrt{2(\gamma_p - 1)}, \tag{3.63}$$

where $\gamma_p = \left(1 - v_p^2/c^2\right)^{-1/2}$. E_{WB} represents a limit on the electric field strengths which can be sustained by the electron density perturbations. As $E \to E_{WB}$, $\beta \to \beta_p$ and $n/n_0 \to \infty$ leading to a breakdown in the cold fluid models [81].

In understanding the effects of a_0 on wakefield formation, this system of equations has been solved numerically and plotted in the following figures for $a_0 = 0.5, 1, 2$. All of these cases use a laser intensity envelope defined as

$$a^2 = a_0^2 \exp\left(-2k_{pe}^2\xi^2\right), \tag{3.64}$$

which is Gaussian in ξ. A radial dependence is omitted, compliant with the 1D formulation presented. In all plots, a normalized electron density perturbation of $\delta n = n/n_0 - 1$ is shown. The laser pulse is centered at $k_{pe}\xi = 0$, moving rightward. The linear regime for $a_0 = 0.5$ is shown in Figure 3.4, with the expected sinusoidal characteristic shapes for the electron plasma density perturbation and the resultant E_z are seen for $\xi < 0$, with a $\pi/2$ phase shift. The quasi-linear regime for $a_0 = 1.0$ is shown in Figure 3.5. Elongation of the plasma wavelength and distortion of the sinusoidal behavior can be seen in comparison with the $a_0 = 0.5$ case. This distortion is clear in Figure 3.6, plotted for $a_0 = 2.0$, where the plasma wavelength is significantly elongated and the density perturbations display a periodic "spiked" behavior. This modified density distribution accompanies the characteristic "sawtooth" behavior in E_z attributed to non-linear plasma waves [81].

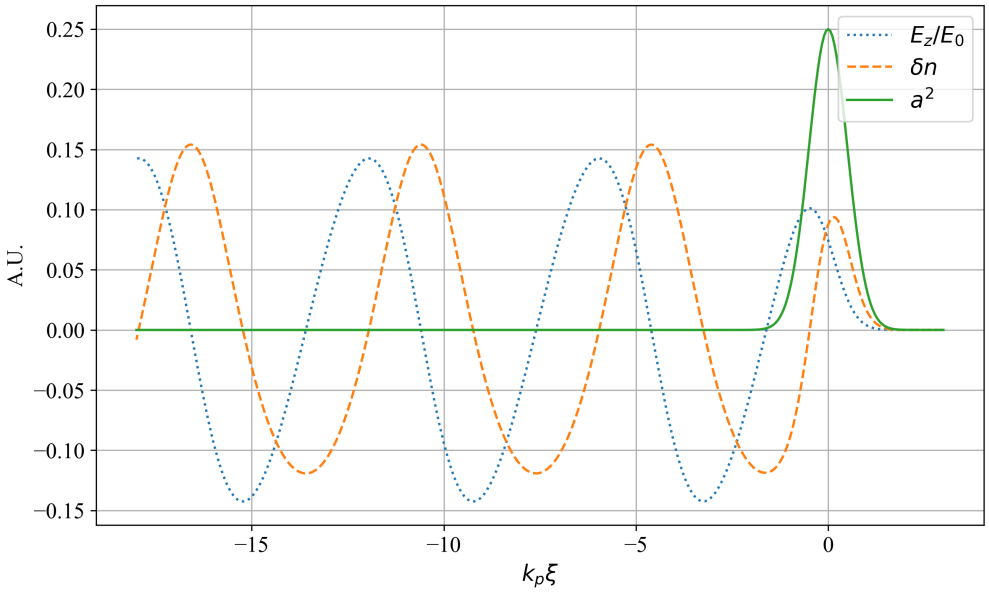

Figure 3.4: Linear plasma wave behavior plotted as function of the co-moving variable $k_{pe}\xi$ for $a_0 = 0.5$, with E_z/E_0, δn, and a^2 shown.

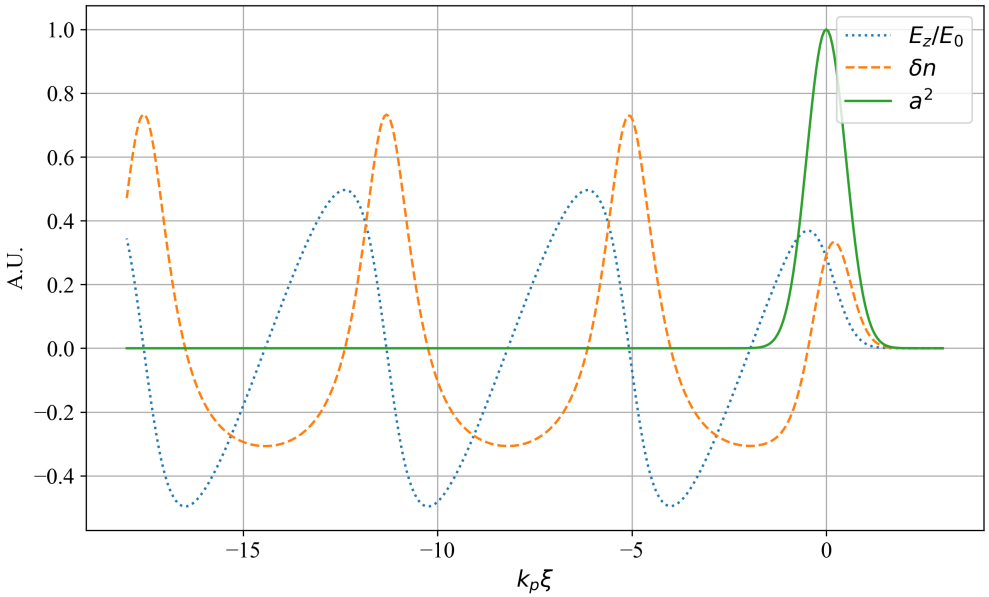

Figure 3.5: Quasi-linear plasma wave behavior plotted as function of the co-moving variable $k_{pe}\xi$ for $a_0 = 1.0$, with E_z/E_0, δn, and a^2 shown.

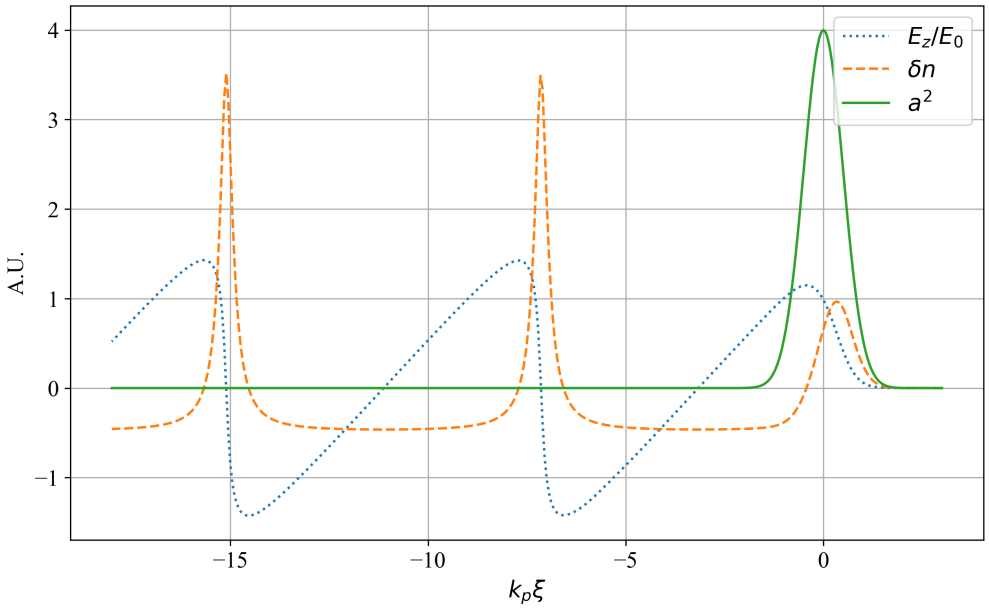

Figure 3.6: Non-linear plasma wave behavior plotted as function of the co-moving variable $k_{pe}\xi$ for $a_0 = 2.0$, with E_z/E_0, δn, and a^2 shown.

3.4 Hundred-Terawatt Thomson laser platform

The experimental work detailed in Chapter 4 was performed using a laser-plasma accelerator at Lawrence Berkeley National Laboratory's BELLA center. The Hundred-Terawatt Thomson (HTT) laser platform is detailed in this section. Designed for dual-arm synchronized femtosecond laser Thomson scattering experiments, the HTT platform is equipped with a ≤ 5 Hz, ≤ 4 J LPA drive laser synchronized with a second ≤ 5 Hz, ≤ 1 J scattering laser arm. An additional third laser arm can be used as a plasma density probe. An overhead view of the entire system is given in Figure 3.7. The system utilizes an 800 nm front end, which is amplified using liquid-cooled Ti:Sapphire multi-pass amplifiers pumped with a dedicated 532 nm, 16 J pump laser. The laser amplification chain is detailed in Figure 3.8. A drive laser energy spread FWHM of $< 3.3\%$ is achieved, with a sample measurement shown in Figure 3.9 for 2500+ consecutive shots. The net drive laser energy can be tuned by adjusting the energy of the pump laser. The laser focus quality is well characterized, with Figure 3.10 detailing beam profile evolution through focus. The pulse duration at the target is adjustable, controlled by the compressor grating spacing following amplification. A scan of pulse duration is shown in Figure 3.11, as measured by Frequency-Resolved Optical Gating (FROG) and a Single-Shot Auto-correlator (SSA). The offset in shortest pulse locations as a function of grating spacing is a result of the measurement geometry. System long term stability is well characterized, and can be observed in the LPA electron beam. A stacked

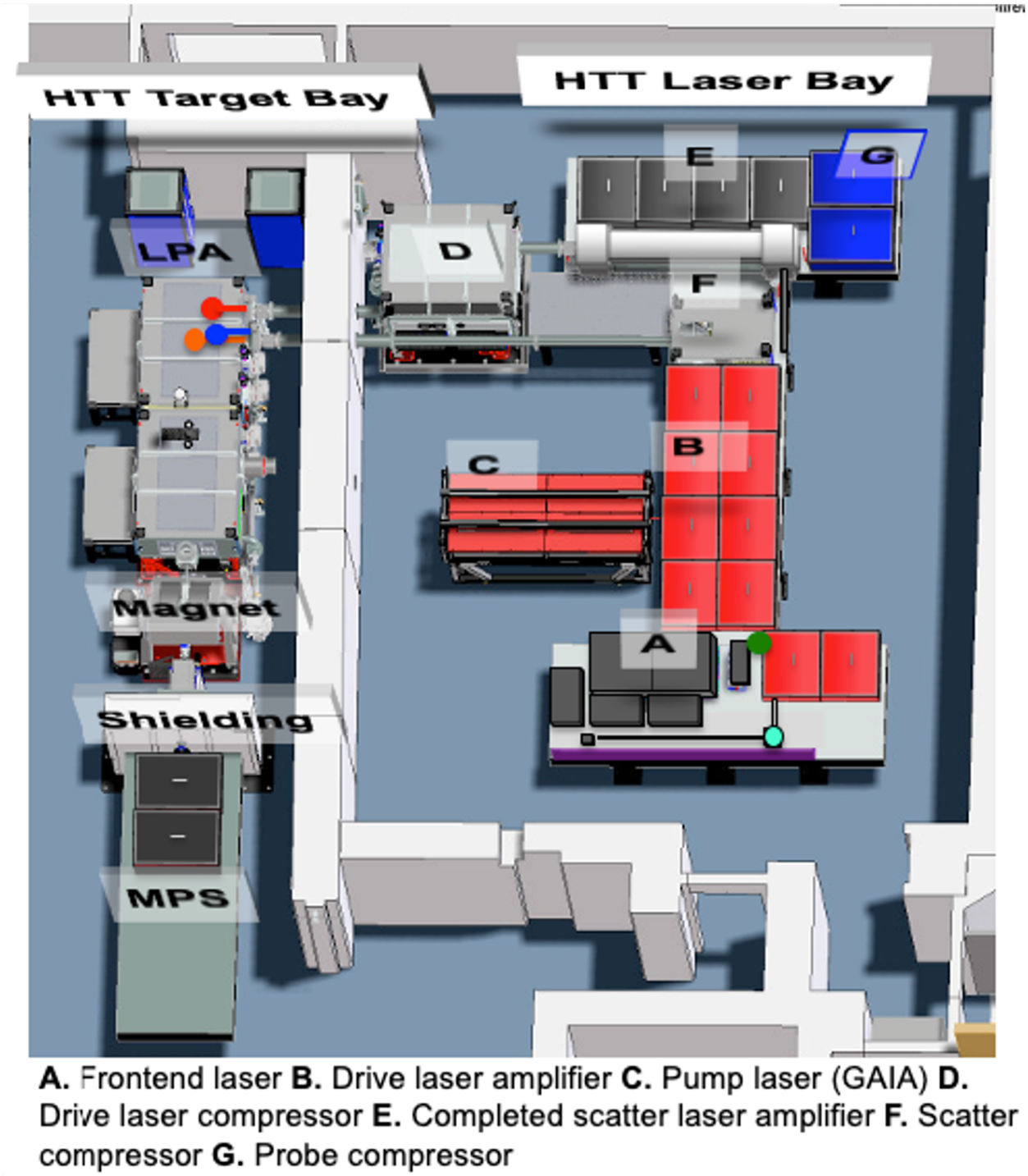

Figure 3.7: Overhead generalized description of the HTT laser system. Laser seeding and amplification occur in the room on the right side of image, with the target chamber on the left.

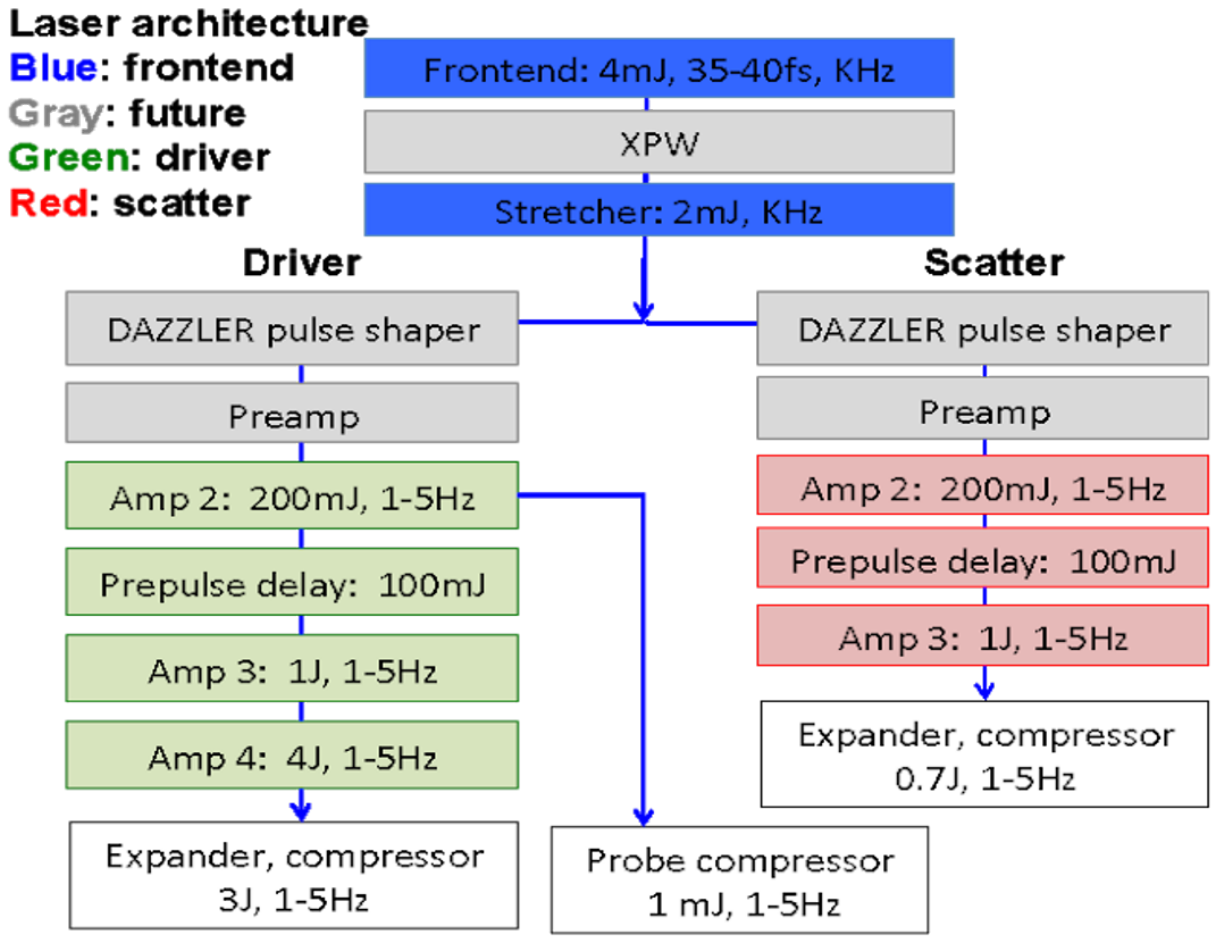

Figure 3.8: Schematic description of the HTT laser amplifier chain. Detailed are the three independent laser arms, with adjustable on-target arrival times. The listed current/future components were accurate at the time of the experiment, but are not representative of the system at the time of publication.

spectrum plot showing electron beam stability over 1000 shots at 1 Hz is shown in Figure 3.12.

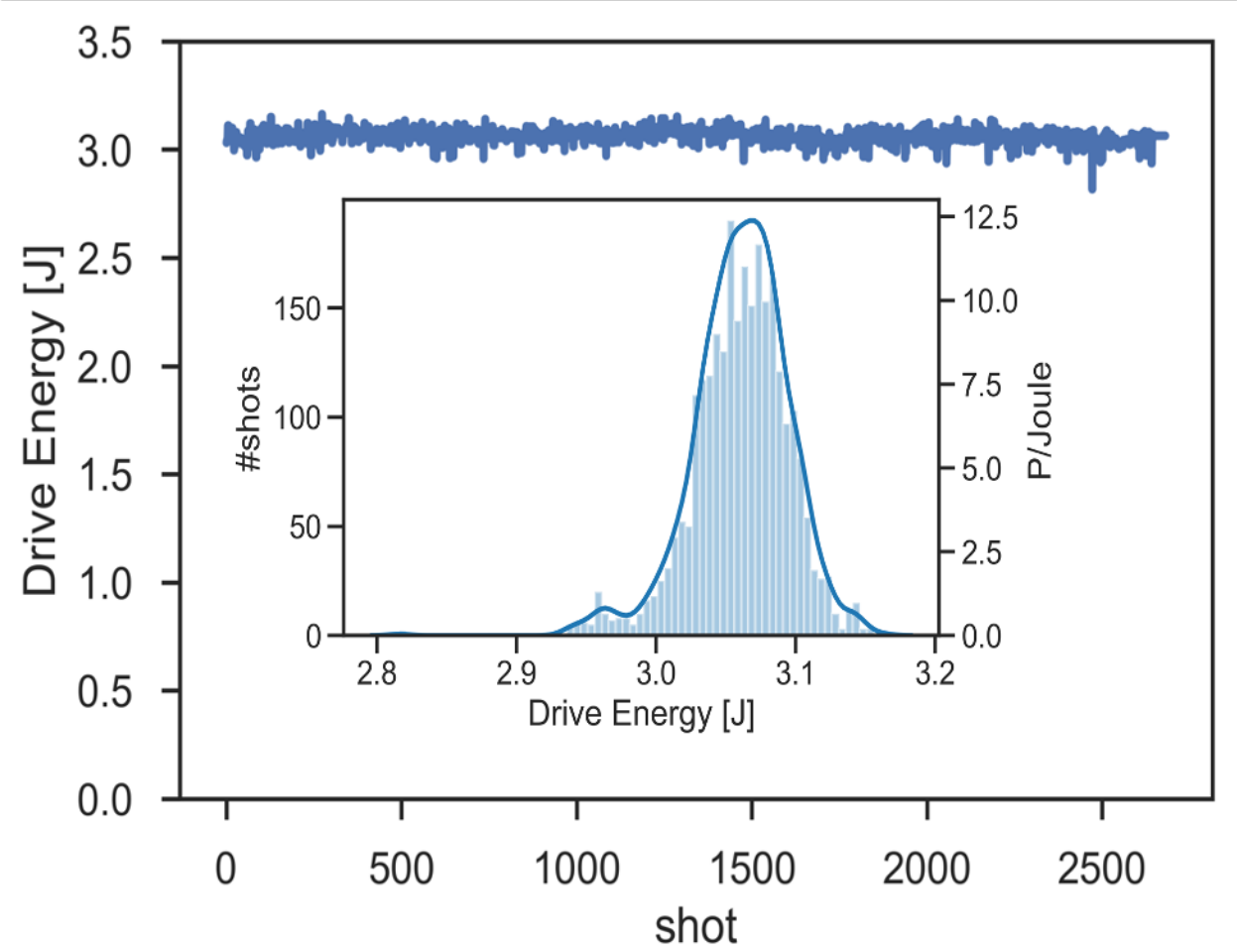

Figure 3.9: Histogram of 2500+ successive shots measuring the amplified drive laser energy.

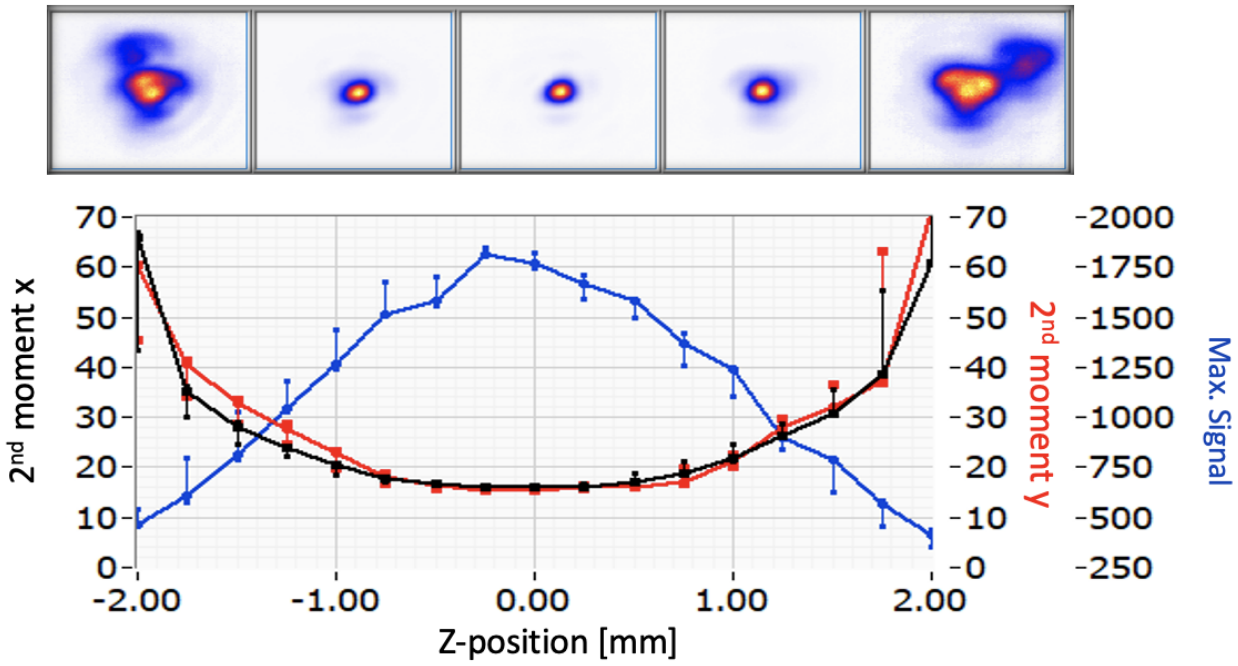

Figure 3.10: Scan data showing the laser profile near focus, with representative CCD images shown at the top. The beam at focus is 20 μm, for a calculated intensity of $\approx 10^{19}$ W/cm^2.

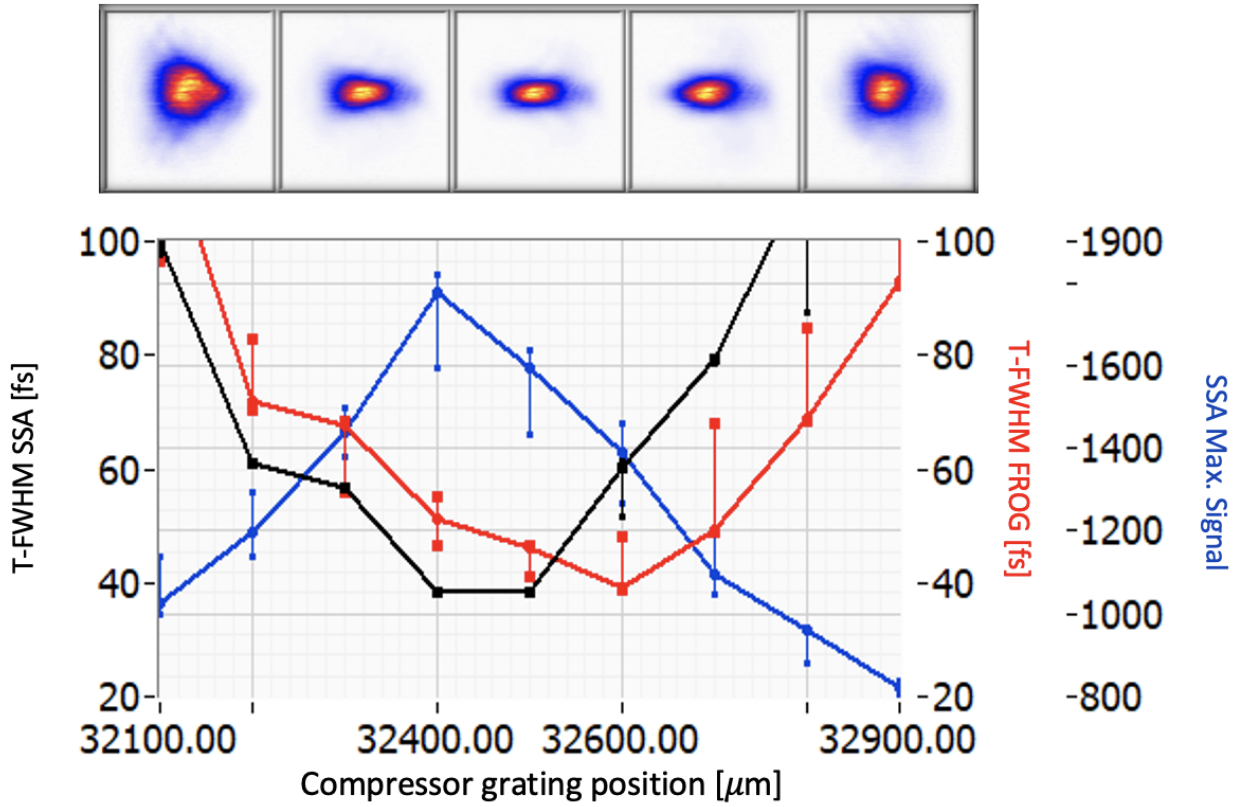

Figure 3.11: Scan data showing the laser temporal FWHM as a function of compressor grating spacing, with representative FROG traces at the top. For both instruments, a FWHM pulse duration of 40 fs is measured, with an offset indicative of measurement geometry.

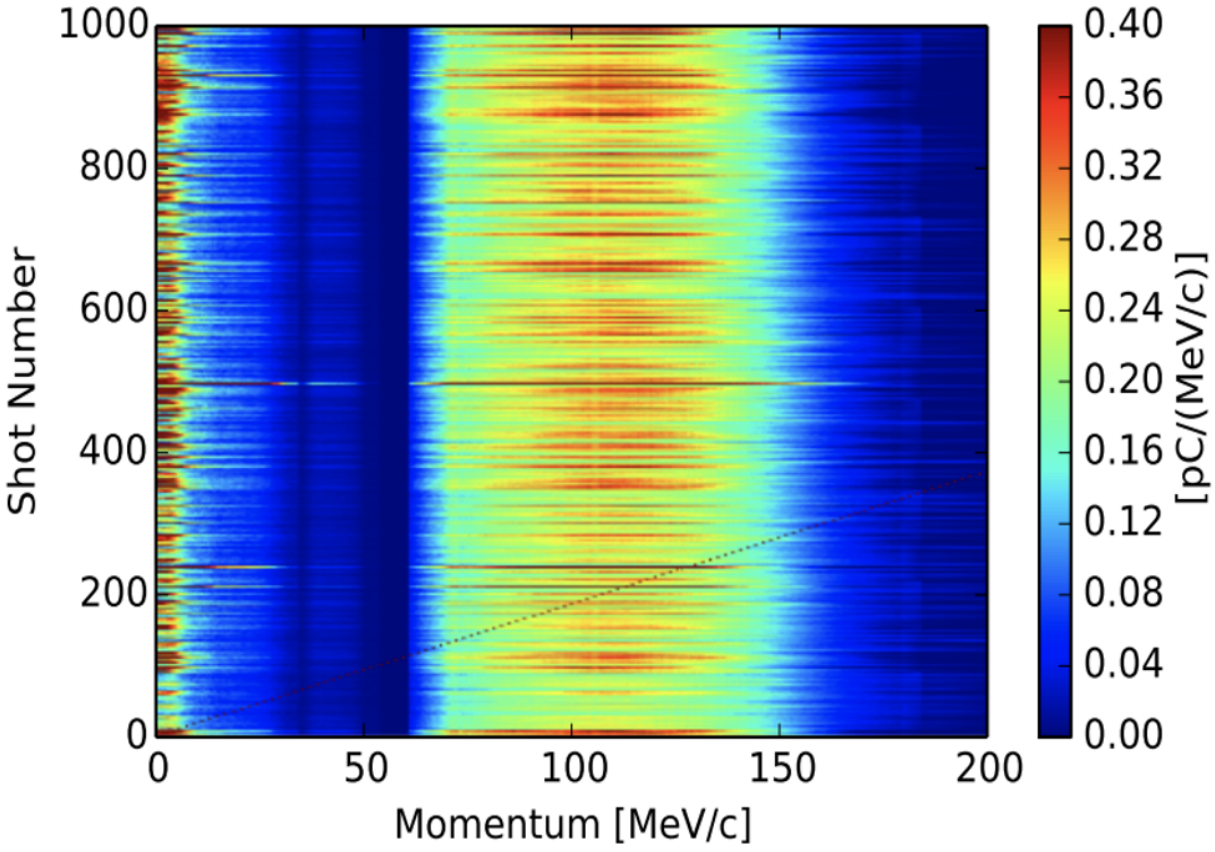

Figure 3.12: Long-term consecutive LPA electron beam spectrum data showing consistency over 1000 shots at 1 Hz.

Chapter 4

Isomer population in Bromine nuclei

4.1 Experimental motivation

A "proof-of-concept" experiment for isomer manipulation using laser-plasma accelerators was performed and is detailed in this Chapter. The ^{79}Br nucleus has an $9/2^+$ isomer at 207.6 keV with a half-life of 4.85 seconds [14]. The goal of the following experiment was to populate the ^{79m}Br state following irradiation in two discrete cases. In both cases, the radiation energy was planned to be > 10 MeV, which is sufficient for excitation into the quasicontinuum. One irradiation was performed using bremsstrahlung photons to photo-excite bromine nuclei, with some fraction populating the isomer state. The second irradiation case was performed using ultra-short electron bunches from the HTT LPA discussed in Chapter 3. The goal was to compare the isomer population rates for each case, with population rates predicted to be higher in the case of electron irradiation. Enhanced isomer population was predicted to occur as a result of enhanced spin-coupling in the quasicontinuum enabled by < 100 fs electron bunches, via nuclear-plasma interactions or electron-nuclear interactions. The ultra-short lifetime of quasicontinuum states requires that the beam source have a time signature on the femtosecond scale, which is a unique property of LPA sources. By modifying the spin-distribution of excited states, it is thought the excited nuclei would de-excite in a manner which may preferentially populate the ^{79m}Br spin isomer state, which has a $\Delta J = 3$ above the ground state. An abbreviated level scheme for ^{79}Br is given in Figure 4.1.

4.2 Experimental design

This experiment utilized an active target configuration, in which the detector contained the target nuclei for excitation. With this configuration, the active target can be irradiated and decay signal from isomer states can then be detected with great efficiency. The active target in this experiment was a 0.5" right cylinder $LaBr_3$ scintillator purchased from Saint-Gobain. This crystal was mounted to a Hamamatsu photo-multiplier tube, which output its signal to a digital multi-channel analyzer from CAEN.

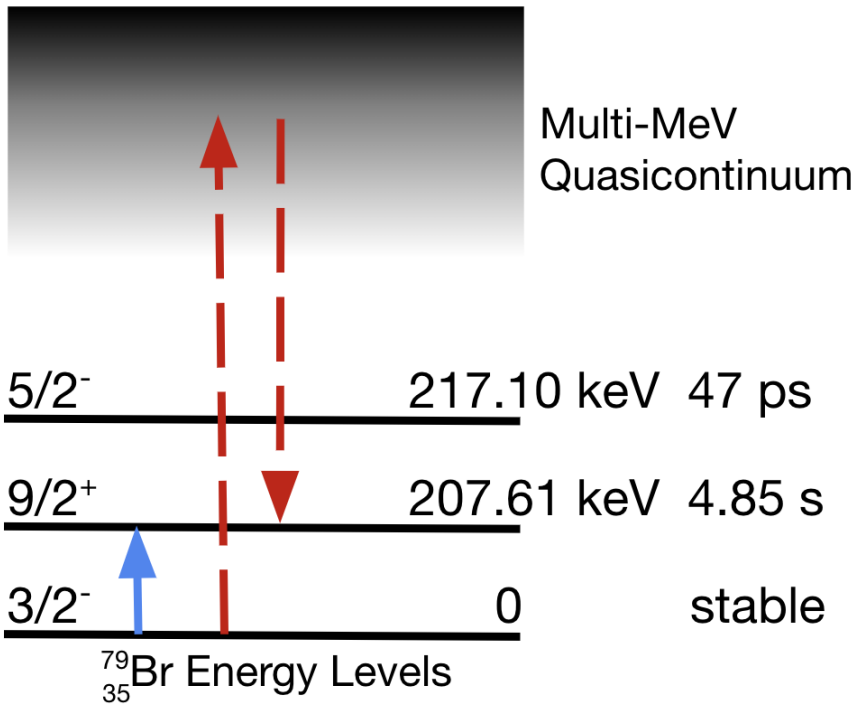

Figure 4.1: Abbreviated nuclear level scheme for ^{79}Br, with lifetimes, energies, and spin states given. The solid blue arrow represents a direction photo-excitation from the ground state into the isomer, while the dashed red arrows represent excitation into the quasicontinuum followed by de-excitation into the isomer state [14].

The $LaBr_3$ crystal is manufactured with natural Bromine which contains an abundance of 50.69% ^{79}Br, with the remainder composed of ^{81}Br [95]. With this isotopic make-up there are two possible long-lived isomers which can be populated, ^{79m}Br and ^{80m}Br. Population of the ^{79m}Br state is attributed to the ^{79}Br(γ,γ')^{79m}Br and ^{81}Br(γ,2nγ')^{79m}Br reactions. Given the approximately equal proportion of ^{79}Br and ^{81}Br nuclei in the active target, it is impossible to attribute observed experimental excitations of the ^{79m}Br state to a given parent nuclei. The ^{80m}Br state is primarily populated by the ^{81}Br(γ,nγ')^{80m}Br reaction, as the incoming photon energy well exceeds the S_n of ^{81}Br at 10.159 MeV [96]. Note the ^{80m}Br state has a half-life of 4.42 hours, which requires a separate treatment experimentally than the ^{79m}Br state, which will be detailed later.

Two experimental configurations were used, to account for the two irradiation cases. For photon irradiation, a 0.46 T dipole magnet is used to disperse the electron beam for energy selection with a movable bremsstrahlung converter. The converter consists of a 2 mm tall, 5 mm deep stainless steel bar. A 0.75 T bending dipole magnet was used to prevent electrons from reaching the active target. Bremsstrahlung photons up to 35 MeV excited the target into the nuclear quasicontinuum. For electron irradiation, the bremsstrahlung converter and

secondary bending dipole were removed from the experiment, allowing ≈ 35 MeV, <100 fs, electron bunches to excite nuclei into the quasicontinuum and promote electron-nuclear interactions in the target. Schematic figures of these experimental configurations are shown in Figures 4.2 and 4.3.

For each irradiation case, the sample was irradiated at 0.05 Hz. This repetition rate corresponds to 20 seconds between shots, which is ≈ 4 times the half-life of the ^{79m}Br state. Counting of de-excitations following each shot was performed, as near-full depletion of the isomer state occurred. This was performed using a rapid high-voltage switch synced to the laser clock. This allowed to the PMT to be biased immediately following each shot, preventing damage from over-exposure during the shot, and then switched off before the following shot. This switching behavior resulted in a changing detector energy response immediately following the shot, but the detector stabilized quickly. For measuring total activations of the ^{80m}Br state, the detector assembly was left operating for days after irradiation, allowing for full depletion of the 4.42 hour isomer [97].

This experiment was performed at the BELLA HTT laser system detailed in Chapter 3 [98, 99]. For this experiment, a 1.75 J, 40 fs laser pulse was focused to a waist size of $\approx$17 μm FWHM with a peak intensity of 7.25×10^{18} W/cm^2 in a high-density gas jet, which produces <100 fs electron beams through laser-plasma accelerator mechanisms discussed in Chapter 3. An electron spectrometer was implemented to characterize the electron energy spectrum. A movable LANEX rare-earth scintillating screen was placed behind the 0.46 T dispersion magnet, with the scintillating side imaged by a CCD camera equipped with an objective lens. A representative electron spectrum is shown in Figure 4.4, with the presence of the stainless steel bar included. This results in a suppressed spectrum at the electron energies which are striking the bar. Energy calibration was performed using the magnet design and particle tracking software RADIA [100].

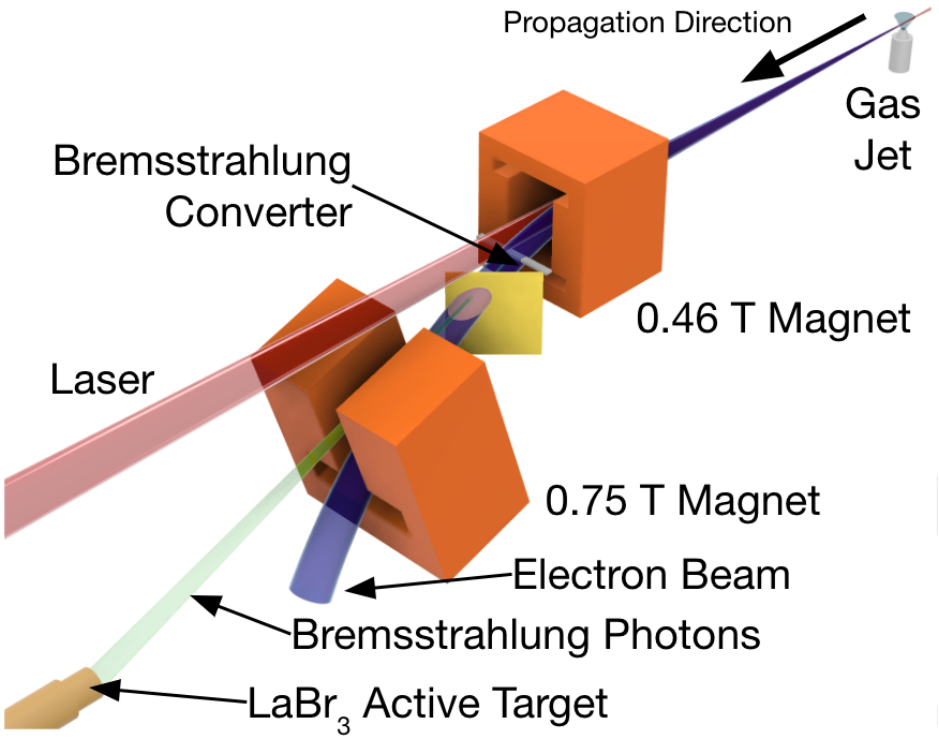

Figure 4.2: Schematic representation of the photon irradiation experimental configuration. The laser, shown in red, is focused in the gas jet, driving the LPA. The resulting electron beam, blue, co-propagates towards the magnet assembly. The 0.46 T dispersion magnet allows for geometric selection of the bremsstrahlung energy endpoints, while the 0.75 T secondary magnet bends the remaining electrons away from the detector, into a plastic shield not pictured. The LANEX screen located between the magnets is removable, providing a diagnostic tool for the electron beam energy.

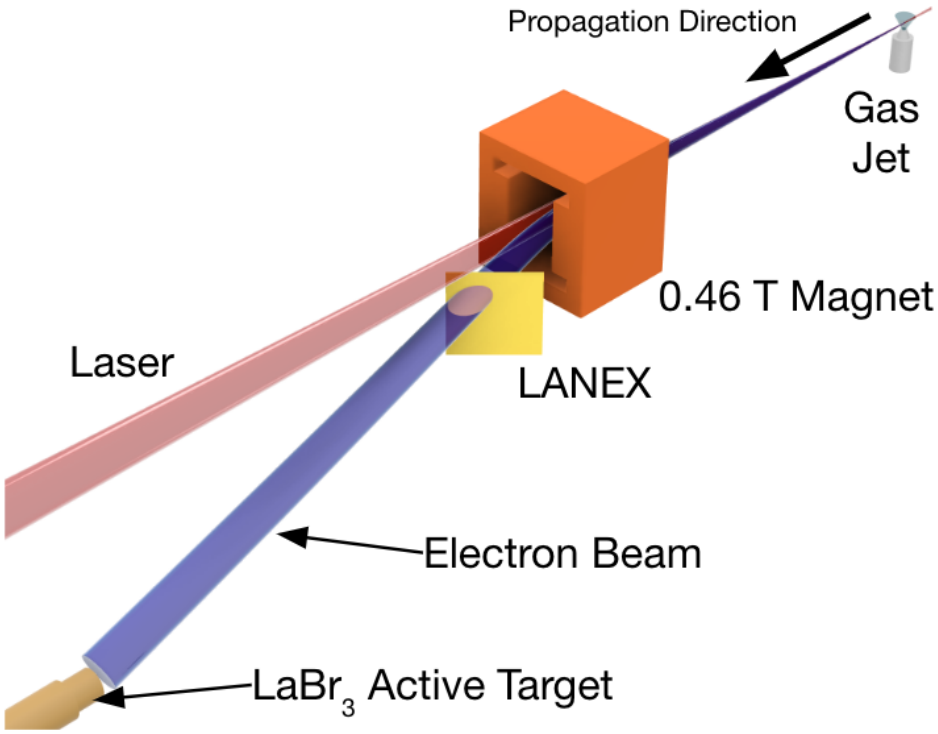

Figure 4.3: Schematic representation of the electron irradiation experimental configuration. The laser, red, is focused in the gas jet, driving the LPA. The resulting electron beam, blue, co-propagates towards the magnet assembly. The 0.46 T dispersion magnet allows for geometric selection of the electron energies which strike the target. The LANEX screen located downstream of the dispersion magnet is removable, providing a diagnostic tool for the electron beam energy.

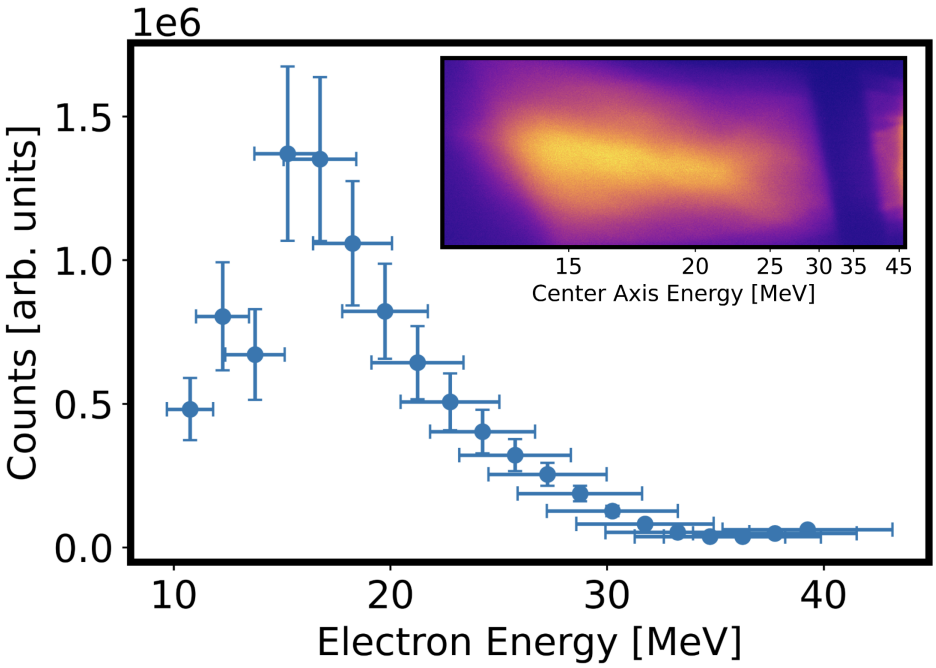

Figure 4.4: Electron energy spectrum showing the measured electron spectrum. The inset plot is an example CCD image with the center-line energy axis provided. As the screen was placed at 40° angle relative to the laser axis, the energy distribution across the image is warped and requires complex analysis. This angle offset is the cause of the diagonal shadow of the bremsstrahlung converter bar.

4.3 Experimental analysis

4.3.1 Identification of isomer signals

In experimentally identifying the isomer decay signal, the characteristic decay γ energy and half-life must be confirmed. Following calibration with a ^{137}Cs sealed source, decay signals from the ^{79m}Br and ^{80m}Br states were identified at the characteristic 207.6 keV and 85.8 keV, respectively [14, 97]. Time-series decay curves are given in Figures 4.5 and 4.6. Calculation of the experimental decay rates using a time-bin count exponential fit gives a $^{79m}t_{1/2} = 4.05 \pm 0.64$ s and $^{80m}t_{1/2} = 4.36 \pm 0.05$ hrs. For ^{79m}Br this calculation was performed using the post-shot accumulated time-series, while for ^{80m}Br the post-irradiation collection data was used.

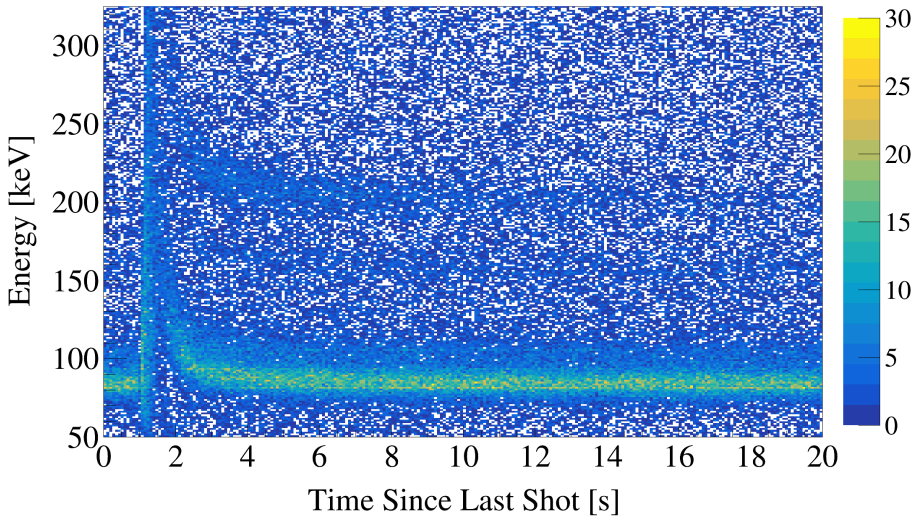

Figure 4.5: Shot-accumulated 2D histogram for the 20 seconds following each shot. The ^{79m}Br decay signal can be seen at 207.6 keV, which can be seen to decay away over the 20 second counting period. The ^{80m}Br decay signal can be seen as a constant background near 85.8 keV, as result of the significantly longer half-life. Note the curved detector response following rapid biasing after each shot.

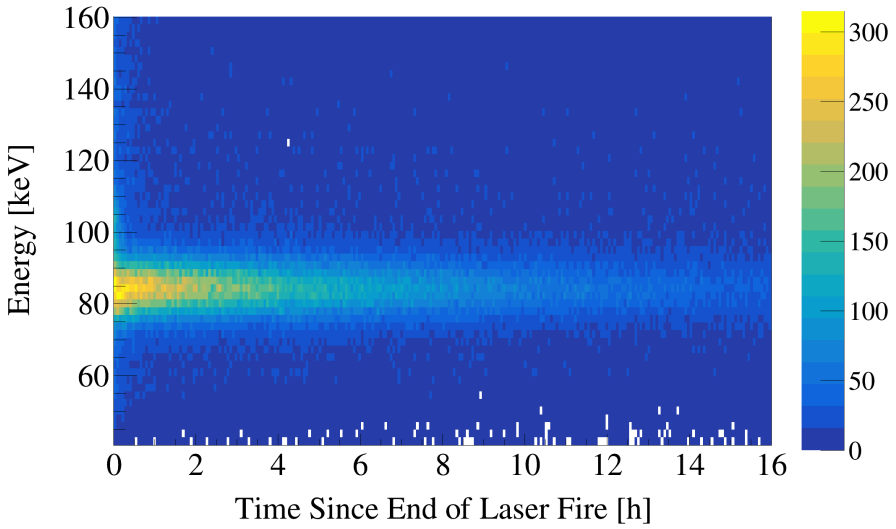

Figure 4.6: Post-irradiation continuous 2D histogram for many hours. The ^{80m}Br decay signal can be seen near 85.8 keV, which can be seen to decay away with the characteristic 4.42 hour half-life.

4.3.2 Calculation of populated nuclei

Following successful identification of the isomer decay signals, the total population of isomer states must be calculated. For ^{79m}Br, which is fully depleted between shots, this process was performed by calculating the original isomer population, N_0, by decay-correcting time-bin counts from the shot-accumulated time-series. Figure 4.7 provides a visual representation of this process, during which a projection across the energy axis (ADC channel) is taken for a given time-bin. Within this projection, the signal peak is identified and fit with a Gaussian plus linear model. This fit allows for subtraction of the counts below the linear background, giving the peak counts value. The peak counts is then decay corrected to determine $N_0^{t_{bin}}$ using Equation 4.2. The mean of the N_0^{tbin} values is taken using Equation 4.3, to calculate the total isomer population N_0. In this set of equations, λ is the decay constant for the isomer of interest, t_{bin} is the center of a time-bin, t_{LHS} and t_{RHS} are the time-bin limits, m is the number of peak bins corresponding to the bottom right plot in Figure 4.7, and n is the number of time-bins evaluated.

$$\text{Peak Counts} = \sum_{i=1}^{m} C_i - \text{BG}_i, \tag{4.1}$$

$$N_0^{t_{bin}} = \frac{\text{Peak Counts}}{\exp(-\lambda \cdot t_{LHS}) - \exp(-\lambda \cdot t_{RHS})}, \tag{4.2}$$

$$N_0 = \frac{\sum_{t_{bin}}^{n} N_0^{t_{bin}}}{n}. \tag{4.3}$$

Calculating the total population of the ^{80m}Br isomer requires separate treatment, due to the long half-life resulting in simultaneous pumping and decay during the experiment. For this case, a two step correction was necessary. First, N_0 was calculated using the method discussed above, with the exception that the post-irradiation long counting period data set was used, shown in Figure 4.6. The activity value at the end of irradiation, A_0, was calculated from N_0 using Equation 4.4. This A_0 was then used to determine an effective isomer pumping rate, P_{eff}, across the duration of the irradiation, t_{irrad}, with Equation 4.5. The calculated P_{eff} was integrated over t_{irrad} in Equation 4.6 to calculate how many ^{80m}Br states had been populated and decayed away before the long counting period, referred to as N_{Dec}. The total number of populated states, N_{total}, is the sum of N_{Dec} and N_0.

$$A_0 = N_0 \cdot \lambda, \tag{4.4}$$

$$P_{eff} = \frac{A_0}{1 - \exp(-\lambda \cdot t_{irrad})}, \tag{4.5}$$

$$N_{Dec} = \int_0^{t_{irrad}} P_{eff} \cdot (1 - \exp(-\lambda \cdot t))dt, \tag{4.6}$$

$$N_{\text{total}} = N_{Dec} + N_0 \tag{4.7}$$

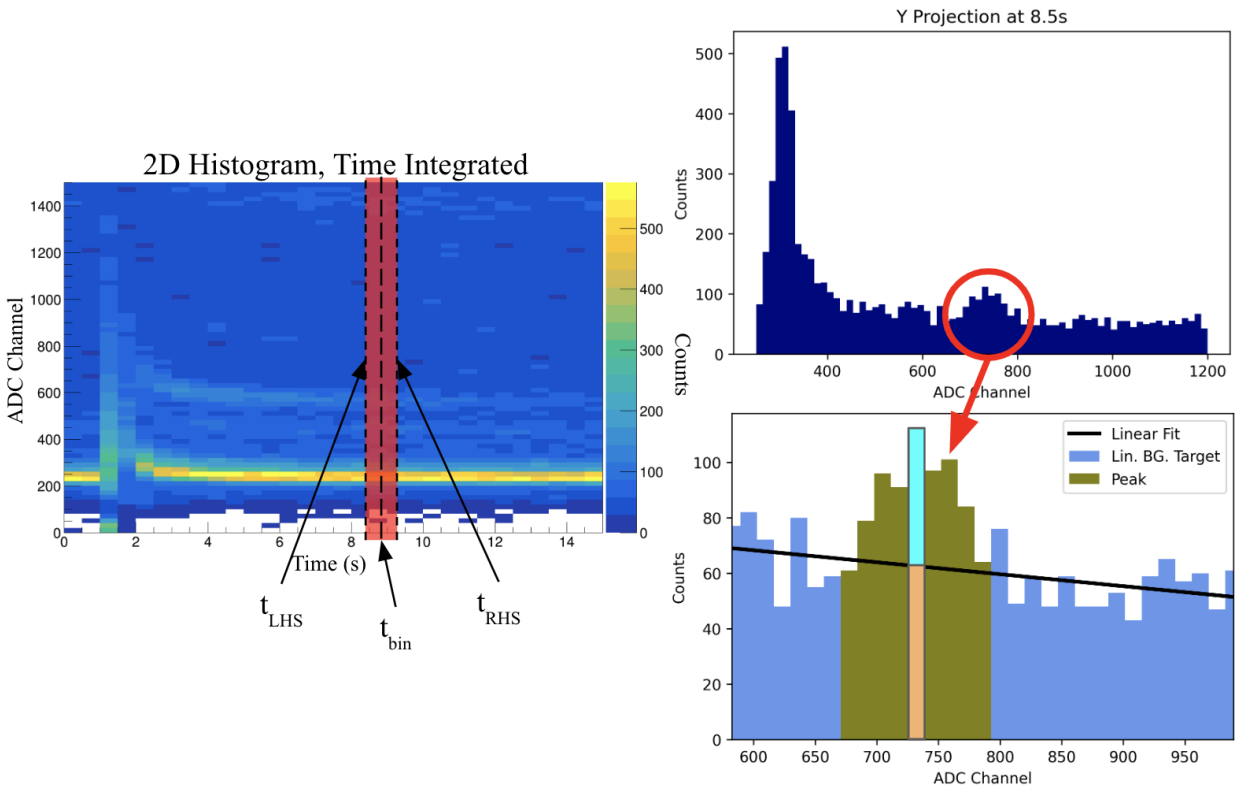

Figure 4.7: Example process for the calculation of total isomer population N_0. The left plot shows the time-selection from the 2D histogram to generate the y-axis projection shown in the top right. The isomer signal peak for ^{79m}Br is circled in red, and magnified on the bottom right. The number of beige-green bins, m, is iterated through to calculate the peak counts, light blue, above the background signal, orange. In Equation 4.1 the total bin value is referred to as C_i and the background signal is BG_i.

This calculation was performed for four data sets, yielding four total isomer activation populations; ^{79m}Br from photon irradiation, ^{80m}Br from photon irradiation, ^{79m}Br from electron irradiation, and ^{80m}Br from electron irradiation. The sum values were then divided by the total number of shots to yield average Activations/Shot per isomer, given in Table 4.1. The ratio of these Activation/Shot is taken for ^{79m}Br/^{80m}Br under both irradiation cases and will be referred to as the isomer activation ratio.

Case	^{79m}Br [#/Shot]	^{80m}Br [#/Shot]	^{79m}Br/^{80m}Br
Photon	13.21 ± 1.29	566.23 ± 17.48	0.023 ± 0.0024
Electron	26.25 ± 0.80	787.50 ± 26.10	0.033 ± 0.0015

Table 4.1: Activations/Shot for isomer decay peaks

4.3.3 TALYS calculations for photo-excitation

The nuclear reactions modelling code TALYS was used to calculate an isomer activation ratio (IAR) for comparison with the experimental value of 0.023±0.0024 for photo-excitation. For these calculations, a bremsstrahlung photon spectrum was calculated using FLUKA-FLAIR for a 35 MeV centered, 2 MeV wide flat electron spectrum incident on the stainless steel bar detailed prior [101, 102, 103]. This spectrum was used to generate energy bins fed into TALYS, which generates reaction cross sections for each of the energy bins. By multiplying the spectrum by the cross sections and integrating total reaction contributions to each isomer, an IAR was calculated. A broad grid search was performed using TALYS default settings for each nuclear level density model and gamma strength function, each of which are detailed in Chapter 2. This grid search is plotted in Figure 4.8, which indicates that the closest matches are found with NLD models 4, 5, and 6, and γSFs 2 and 5.

Following this broad grid search, the closest matches to the experimental ^{79m}Br/^{80m}Br isomer activation ratio were achieved with combinations of TALYS γSF models 1, 2, 3, and 5, the Kopecky-Uhl generalized Lorentzian, Brink-Axel, Skyrme-Hartree-Fock BCS model, and the Hybrid Lorentzian-microscopic model, respectively, and NLD models 4, 5, and 6, the Skyrme-Hartree-Fock-Bogoliubov, Gogny-Hartree-Fock-Bogoliubov, and temperature-dependent Gogny-Hartree-Fock-Bogoliubov tabulated values, respectively. The closest calculated value was ≈0.128, which is significantly higher than the 0.023 ± 0.0024 ratio observed experimentally. TALYS calculation parameters for NLDs 4, 5, and 6 were systematically adjusted in efforts to better match experimental data. These adjustments resulted in a decreased IAR by ≈ 20%, which still far exceeds the experimental value.

Modification of angular momentum distributions within the microscopic NLD models was explored in order to better match the experimental IAR. Given the ΔJ isomers populated in the experiment, shifting the angular momentum distributions used in TALYS calculations should affect the feeding into the high-spin isomer states. Manual shifts of level densities were performed as a function of nuclear spin state, J. The tables for TALYS NLD models 4, 5, and 6 were manually adjusted with intent of shifting level density at each energy bin, as a function of spin, J. This was performed with Equations 4.8 and 4.9:

$$\rho'_{E,i} = \left(\sum_{j=1+X}^{k} \delta_{i,j} \right) \rho_{E,i-X} + \frac{1}{k} \sum_{l=1+k-X}^{k} \rho_{E,l}, \tag{4.8}$$

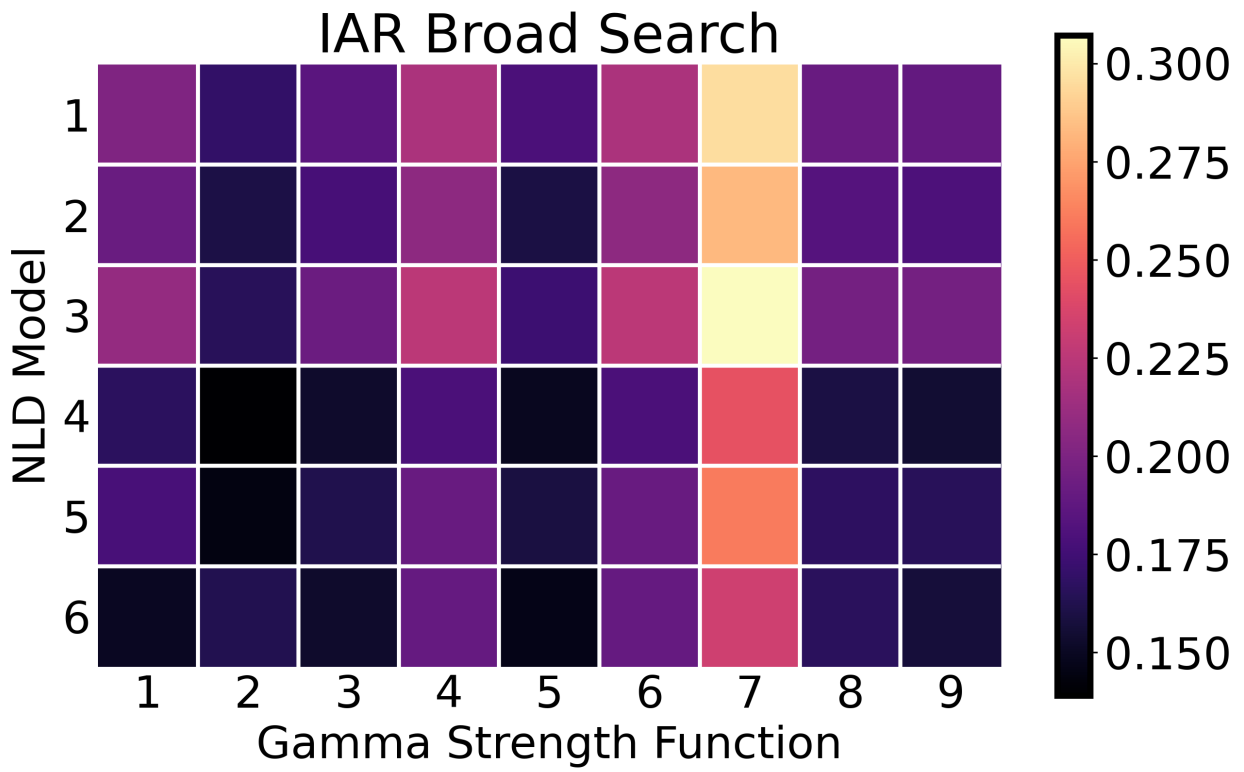

Figure 4.8: Grid of TALYS default NLDs and γSFs used to calculate isomer activation ratios for the photo-excitation case using the stainless steel bremsstrahlung converter.

$$\rho'_{E,i} = \left(\sum_{j=1}^{k-X} \delta_{i,j} \right) \rho_{E,i+X} + \frac{1}{k} \sum_{l=1}^{X} \rho_{E,l}, \tag{4.9}$$

which shift the level density $\rho(E, i)$ within each energy bin E by a positive integer X multiples of $\hbar$. In this form, i is the J bin iterator, $\rho'_{E,i}$ is the level density after the shift, and k is the number of J states with non-zero level density at E. Distinct equations are used for positive and negative direction shifts. For all nuclei, shifted distributions were calculated for $-10\hbar \leq X \leq +10\hbar$. Total level density, $\rho(E)$, is preserved as level density values shifted out of the table are summed and distributed evenly across the corresponding $\rho(E, J)$ space in locations where $\rho(E, J)$ contained non-zero values. Level density was not introduced into $\rho(E, J)$ components where level density was not present before modification. ^{79}Br and ^{81}Br NLD tables were shifted together, in order to prevent unintentional modification of neutron pairing interactions, while ^{80}Br was shifted independently. For these calculations, γSF models 1, 2, and 3 were used. An example of this shift is shown in Figure 4.9.

After performing this shift for TALYS NLD models 4, 5, and 6, the best match to experimental data was found with γSF model 2, NLD model 4, $+4\hbar$ shifts for ^{79}Br and ^{81}Br nuclei, and $+5\hbar$ for ^{80}Br nuclei. This combination produced a calculated IAR of 0.075 to

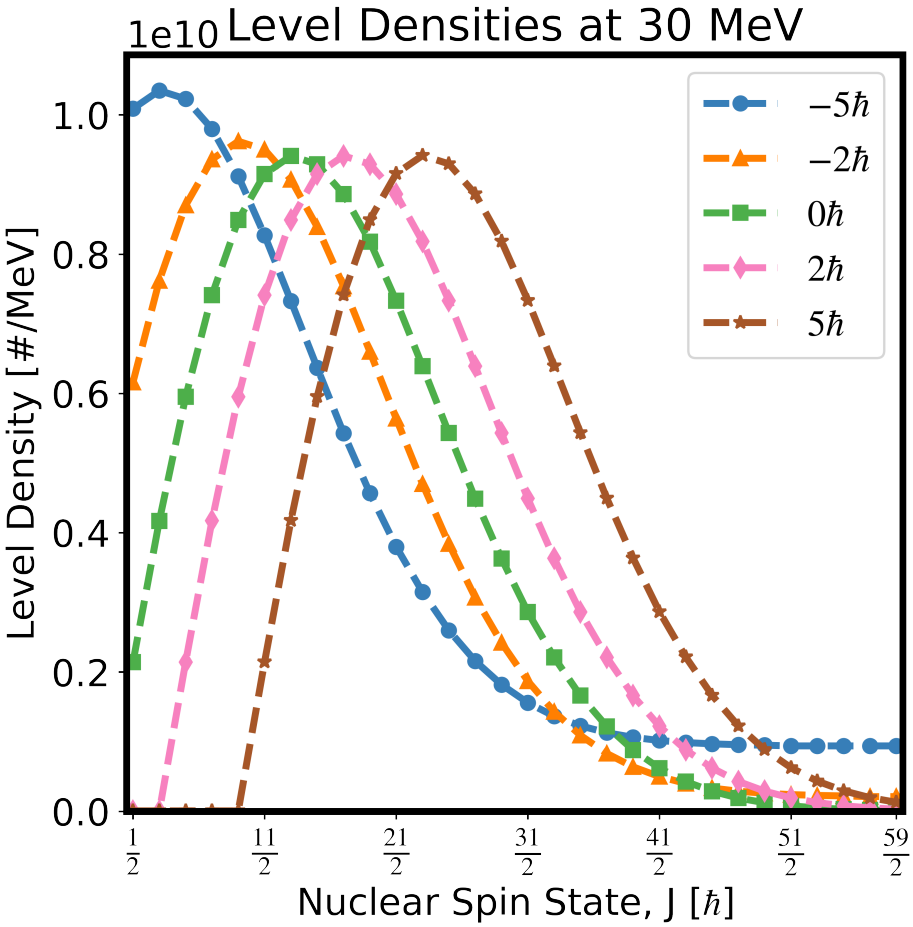

Figure 4.9: Shifted $\rho(E, J)$ distributions at 30 MeV in ^{79}Br.

compare with the experimentally observed 0.023 ± 0.0024. Modification of γSF models 1, 2, and 3 was performed within the parameters offered by TALYS, however, no appreciable changes to the calculated IAR were observed. NLD distribution modifications remained the dominant factor.

4.3.4 Comparison of electron and photon irradiation cases

Shown in Table 4.1, the observed IARs differ between the photon and electron irradiation case. In explaining this discrepancy, FLUKA simulations comparing the stainless steel bremsstrahlung spectrum and internally generated $LaBr_3$ bremsstrahlung spectrum were performed [101]. These spectra are plotted in Figure 4.10, with the internal electron spectrum resulting from the geometrically selected LPA electron beam interacting with the target included. These two distinct bremsstrahlung spectra were used in TALYS calcula-

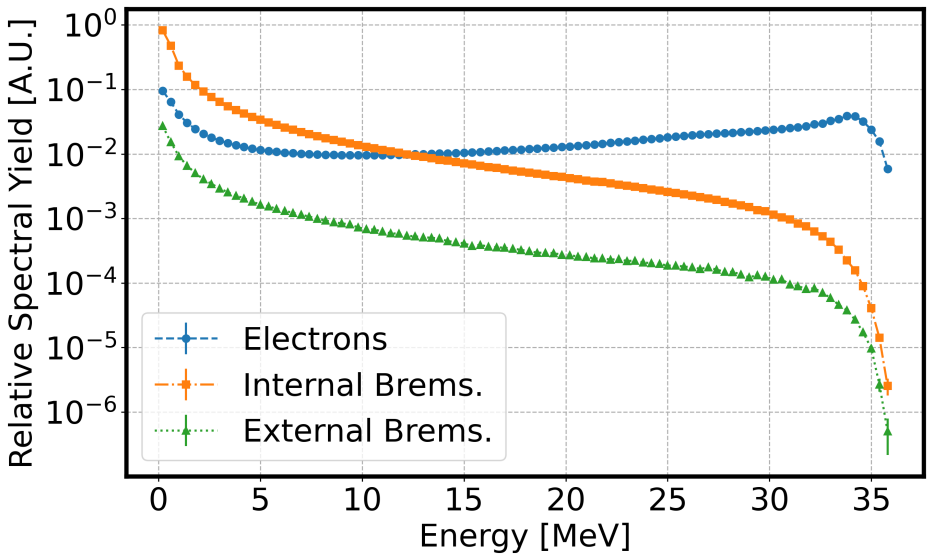

Figure 4.10: Simulated spectra at the $LaBr_3$ active target comparing the internally generated bremsstrahlung from the electron beam, bremsstrahlung from the stainless steel bar, and the internal electron scattering spectrum. All calculated with FLUKA for an electron beam centered at 35 MeV with a flat width of 2 MeV.

tions to calculate IARs for the TALYS default NLD Model 4, γSF model 2 case and the shifted NLD Model 4, γSF model 2 case [104]. The double ratios of the calculated internal $LaBr_3$ bremsstrahlung/stainless steel bremsstrahlung IARs were taken to compare with the experimentally observed electron/photon double ratio of 1.43. For the default and shifted distribution cases, the double ratios are 0.94 and 0.87, respectively. Neither match the experimentally observed double ratio of 1.43 and both are < 1, indicating that there are contributions which are not accounted for by photo-excitations. Contributions from (e,e') interactions may strongly contribute to isomer populations, but calculations for these contributions need to be developed.

Determining the potential for contributions from NPIs requires an understanding of the ionization states present in the crystal during exposure to the ultra-short electron beam. Electron beam energy deposition calculations performed with FLUKA do not suggest energy deposition sufficient for bulk plasma generation within the $LaBr_3$ crystal, making it difficult to attribute the discrepancy in double ratios to NEEC and NEET mechanisms. Figure 4.11 details the energy deposition within the crystal, and suggests that the energy deposited per Br nuclei per picocoulomb of charge is insufficient for bulk nuclear-plasma interactions to occur as ionization energies for outer-shell electrons are on the eV scale.

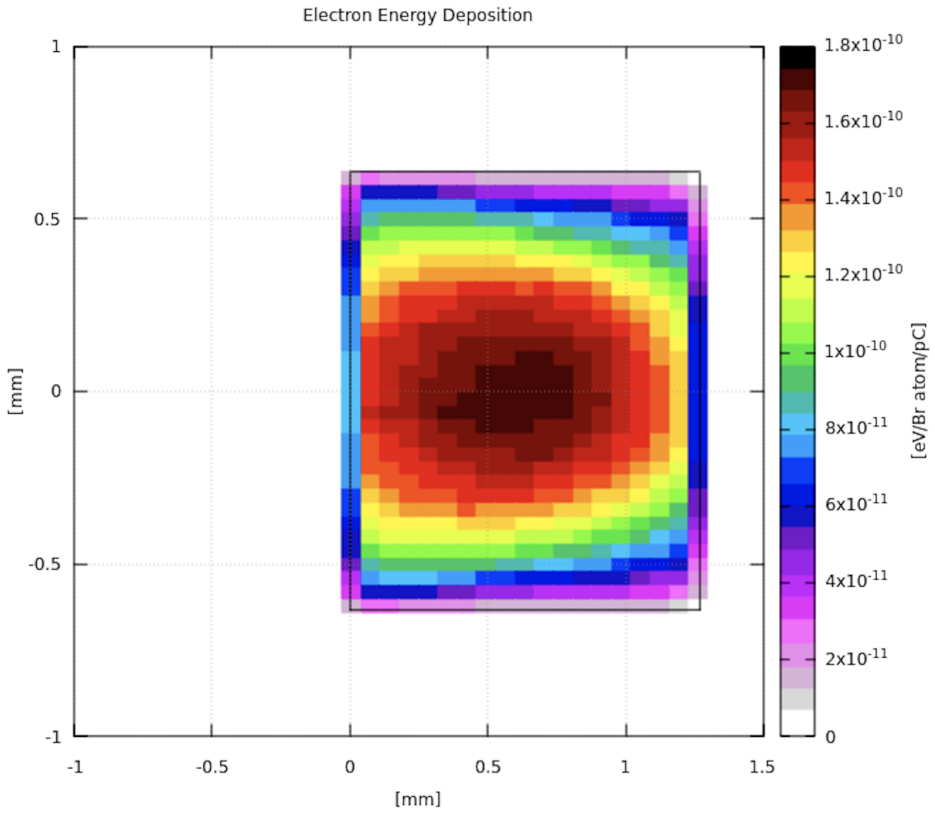

Figure 4.11: Simulated electron energy deposition for an electron beam centered at 35 MeV with a flat width of 2 MeV in the $LaBr_3$ active target. Color bar calibrated for eV/Br atom/pC of electron beam charge.

4.4 Discussion

There are two primary areas of discussion raised by the analysis performed. First, addressing the mismatch between the experimental and calculated IARs for the photo-excitation case requires discussion of methods used in TALYS calculations and nuclei-specific considerations which may be missing. The modified $+4\hbar/+5\hbar$ shift for odd/even nuclei may be attributed to population of the $g9/2^+$ orbital near the Fermi surface in Bromine nuclei. Nucleon occupation of this intruder orbital could result in a potential shift of $\rho(E, J)$ by $4.5\hbar$.

In TALYS, shifting the angular momentum distribution increased the ^{81}Br(γ,n)^{80m}Br reaction cross section by approximately 43%. In contrast, the ^{79m}Br population, which is overwhelmingly populated by the ^{81}Br(γ,2nγ')^{79m}Br reaction, decreased by less than 10%. Increased population of high spin states should inhibit neutron emission following excitation, due to an increased centrifugal barrier, which could explain the converging ^{79m}Br/^{80m}Br IAR as single neutron emission from ^{81}Br is less suppressed than double neutron emission into

^{79m}Br state. However, TALYS reaction modelling does not account for the shifted angular momentum distributions when determining neutron transmission coefficients. As such, the shifted distributions predominantly modify photon transitions between states. Further calculations are required in building a self-consistent explanation for the observed IAR. Experimental characterization of NLDs and γSFs for Br nuclei would provide needed validation for calculations.

Second, the discrepancy between the photon and electron irradiation IARs requires development of (e,e') reaction rate calculations. These interactions represent inelastic electron scattering (IES) off of the nucleus. There are two routes by which these interactions can excite nuclei and modify isomer activation rates. The first is direct excitement of the nucleus by the electron, which can impart more spin than pure photo-excitation. Evaluated nuclear data for these interactions are sparse. Second, inelastic electron scattering off nuclei already excited into the quasicontinuum must be considered, as the enhanced NLD may allow for significant energy-spin coupling into the nucleus. Frameworks for these calculations will need to be developed. As discussed in Chapter 2, Harston and Chemin have performed IES rate calculations for low lying states in ^{235}U, but the conditions evaluated are vastly different than those explored in the Br experiment documented here [63].

Conclusion

The development of laser-plasma accelerators as an experimental platform for probing nuclear properties, such as gamma strength functions and nuclear level densities, gives access to a new regime of interactions at the femtosecond timescale. These platforms enable pump-probe experiments exploring highly excited states in nuclei, previously inaccessible due to their ultra-short lifetimes. Additionally, < 100 femtosecond electron beams may enable excitation into the quasicontinuum followed by secondary energy-spin coupling into the nucleus mediated by electron-nuclear and nuclear-plasma interactions as a result of the enhanced nuclear level densities at quasicontinuum energies. These interactions can be utilized to explore novel isomer manipulation techniques in a broad range of nuclei, which have practical applications for energy storage, radio-medicine, spent-fuel mitigation, and space exploration. Developing an improved understanding of quasicontinuum properties and nuclear-plasma interactions will provide insight into heavy element stellar nucleosynthesis through the s-, p-, and r-processes.

Chapter 4 details a proof-of-concept experiment in exploring isomer manipulation in Br nuclei using a laser-plasma accelerator. By comparing populations of ^{79m}Br and ^{80m}Br following separate irradiation by bremsstrahlung photons and ultra-short electron beams, two notable results are found. For the photo-excitation only case, attempts to match the experimental ^{79m}Br/^{80m}Br isomer activation ratio with TALYS calculations led to significant modifications of nuclear level density angular momentum distributions. These shifts may be explained by population of the $g9/2^+$ intruder orbital near the Fermi surface in Br nuclei. However, TALYS calculations do not account for these shifted distributions when calculating neutron transmission coefficients. In better evaluating the experimental results with theory, there are several other parameters which can be explored. Parity balance of excited states may not be equal, and this could have significant impact on expected isomer activation ratios. Additionally, a self-consistent exploration of neutron optical model parameters with the shifted angular momentum distributions will provide better insight into the behavior of excited Br nuclei.

In comparing the electron and photon irradiation cases, a discrepancy between the isomer activation ratios was found that cannot be attributed to photo-excitation mechanisms. While simulations suggests that electron energy deposition was insufficient to foster ionization conditions conducive to NEEC and NEET reactions, calculations for inelastic electron scattering (e,e') reactions need to be developed to determine their contributions to isomer populations.

Calculation frameworks for ground-to-excited and quasicontinuum-coupled (e,e') interactions are lacking, but may explain the observed isomer activation ratio.

A follow-up experiment is planned to better characterize the isomer population reactions. A $LaBr_3$ bremsstrahlung converter would unify the external and internal photon spectrum, removing any potential for discrepancies to be attributed to photo-excitation mechanisms. Addition of an electron collimator coupled to an integrating current transformer following dispersion will give a quantified value of the charge on target, as well as allow for calculation of bremsstrahlung intensity. Also, lowering the radiation energy below the S_{2n} threshold in ^{81}Br will restrict the population of ^{79m}Br to the ^{79}Br$(\gamma,\gamma')^{79m}$Br reaction. By removing this second feeding channel, a direct measurement of the isomer population rate can be performed. This adjustment will make analysis of changes to TALYS calculation parameters and their impact more straightforward.

Moving beyond proof-of-concept, an experiment for irradiation of various Americium nuclei using ultra-short electron beams is planned. In addition to characterizing gamma strength functions and nuclear level densities for heavy nuclei, inclusion of ^{242m}Am as a target nuclei will provide a direct test for induced isomer depopulation through excitation into the quasicontinuum. Modification of spin distributions in the quasicontinuum may promote enhanced de-excitation into the ground state, as introduced in Chapter 1. If successful, this approach may be developed for application in spent-fuel mitigation and production of ^{238}Pu, an isotope valuable for space exploration.

In totality, the work presented establishes laser-plasma accelerators as a tool for probing nuclear level densities and γSF, as well demonstrates their capability for isomer manipulation experiments. With the unique capability of femtosecond scale pulses, laser-plasma accelerators provide a novel platform for characterizing nuclear properties and evaluating isomer manipulation techniques. Additional exploration of electron-nuclear and nuclear-plasma interactions will provide insight into stellar heavy element synthesis and inertial confinement fusion experiments.

Bibliography

[1] William C. Eckelman. "Unparalleled Contribution of Technetium-99m to Medicine Over 5 Decades". In: *JACC: Cardiovascular Imaging* 2.3 (2009), pp. 364–368. DOI: 10.1016/j.jcmg.2008.12.013. eprint: https://www.jacc.org/doi/pdf/10.1016/j.jcmg.2008.12.013. URL: https://www.jacc.org/doi/abs/10.1016/j.jcmg.2008.12.013.

[2] Odilon A. P. Tavares and Maria Letizia Terranova. "Physical viability for nuclear batteries". In: *Journal of Radioanalytical and Nuclear Chemistry* 332.10 (Oct. 2023), pp. 3933–3942. ISSN: 1588-2780. DOI: 10.1007/s10967-023-09034-9. URL: https://doi.org/10.1007/s10967-023-09034-9.

[3] Haowei Xu et al. "Two-Photon Interface of Nuclear Spins Based on the Optonuclear Quadrupolar Effect". In: *Phys. Rev. X* 13 (1 Feb. 2023), p. 011017. DOI: 10.1103/PhysRevX.13.011017. URL: https://link.aps.org/doi/10.1103/PhysRevX.13.011017.

[4] Giorgos Nicolau Akihiro Sasahara Tetsuo Matsumura and Dimitri Papaiounnou. "Neutron and Gamma Ray Source Evaluation of LWR High Burn-up UO2and MOX Spent Fuels". In: *Journal of Nuclear Science and Technology* 41.4 (2004), pp. 448–456. DOI: 10.1080/18811248.2004.9715507. eprint: https://doi.org/10.1080/18811248.2004.9715507. URL: https://doi.org/10.1080/18811248.2004.9715507.

[5] Malcolm Joyce. "Chapter 15 - Radioactive Waste Management and Disposal". In: *Nuclear Engineering*. Ed. by Malcolm Joyce. Butterworth-Heinemann, 2018, pp. 357–378. ISBN: 978-0-08-100962-8. DOI: https://doi.org/10.1016/B978-0-08-100962-8.00015-9. URL: https://www.sciencedirect.com/science/article/pii/B9780081009628000159.

[6] M. J. Martin and C. D. Nesaraja. In: *Nucl. Data Sheets 186, 261* (2022).

[7] E. Browne and J. K. Tuli. In: *Nucl. Data Sheets 127, 191* (2015).

[8] Oak Ridge National Laboratory. *PU-238 shipment quantity "opens the tap" for space missions: ORNL*. Sept. 2023. URL: https://www.ornl.gov/news/pu-238-shipment-quantity-opens-tap-space-missions.

[9] Richard A. Ward. "The Importance of Long-Lived Isomeric States in s-Process Branching". In: *The Astrophysical Journal* 216 (Sept. 1977), pp. 540–547.

[10] M. Busso, R. Gallino, and G. J. Wasserburg. "Nucleosynthesis in Asymptotic Giant Branch Stars: Relevance for Galactic Enrichment and Solar System Formation". In: *Annual Review of Astronomy and Astrophysics* 37.1 (1999), pp. 239–309. DOI: 10.1146/annurev.astro.37.1.239. eprint: https://doi.org/10.1146/annurev.astro.37.1.239. URL: https://doi.org/10.1146/annurev.astro.37.1.239.

[11] G. Wendell Misch et al. "Astromers: Nuclear Isomers in Astrophysics*". In: *The Astrophysical Journal Supplement Series* 252.1 (Dec. 2020), p. 2. DOI: 10.3847/1538-4365/abc41d. URL: https://dx.doi.org/10.3847/1538-4365/abc41d.

[12] Philip Walker and George Dracoulis. "Energy traps in atomic nuclei". In: *Nature* 399.6731 (May 1999), pp. 35–40. ISSN: 1476-4687. DOI: 10.1038/19911. URL: https://doi.org/10.1038/19911.

[13] Kenneth S Krane. *Introductory nuclear physics*. New York, NY: Wiley, 1988. URL: https://cds.cern.ch/record/359790.

[14] Balraj Singh. In: *Nucl. Data Sheets 135, 193* (2016).

[15] G D Dracoulis. "Isomers, nuclear structure and spectroscopy". In: *Physica Scripta* 2013.T152 (Jan. 2013), p. 014015. DOI: 10.1088/0031-8949/2013/T152/014015. URL: https://dx.doi.org/10.1088/0031-8949/2013/T152/014015.

[16] Leonid Mandelstam and IG Tamm. "The uncertainty relation between energy and time in non-relativistic quantum mechanics". In: *Selected papers*. Springer, 1991, pp. 115–123.

[17] Jan Hilgevoord. "The uncertainty principle for energy and time. II". In: *American Journal of Physics* 66.5 (May 1998), pp. 396–402. ISSN: 0002-9505. DOI: 10.1119/1.18880. eprint: https://pubs.aip.org/aapt/ajp/article-pdf/66/5/396/12000445/396_1_online.pdf. URL: https://doi.org/10.1119/1.18880.

[18] J. J. Carroll et al. "Photoexcitation of nuclear isomers by (γ,γ') reactions". In: *Phys. Rev. C* 43 (3 Mar. 1991), pp. 1238–1247. DOI: 10.1103/PhysRevC.43.1238. URL: https://link.aps.org/doi/10.1103/PhysRevC.43.1238.

[19] Sandro Kraemer et al. "Observation of the radiative decay of the 229Th nuclear clock isomer". In: *Nature* 617.7962 (May 2023), pp. 706–710. ISSN: 1476-4687. DOI: 10.1038/s41586-023-05894-z. URL: https://doi.org/10.1038/s41586-023-05894-z.

[20] Simon Stellmer et al. "Attempt to optically excite the nuclear isomer in ^{229}Th". In: *Phys. Rev. A* 97 (6 June 2018), p. 062506. DOI: 10.1103/PhysRevA.97.062506. URL: https://link.aps.org/doi/10.1103/PhysRevA.97.062506.

[21] L. von der Wense, B. Seiferle, and P. G. Thirolf. "Towards a 229Th-Based Nuclear Clock". In: *Measurement Techniques* 60.12 (Mar. 2018), pp. 1178–1192. ISSN: 1573-8906. DOI: 10.1007/s11018-018-1337-1. URL: https://doi.org/10.1007/s11018-018-1337-1.

[22] National Research Council (US) Committee on Medical Isotope Production Without Highly Enriched Uranium. "Medical Isotope Production Without Highly Enriched Uranium". In: Washingtion (DC): National Academies Press (US), 2009. Chap. 2, Molybdenum-99/Technetium-99m Production and Use. URL: https://www.ncbi.nlm.nih.gov/books/NBK215133/.

[23] National Research Council (US) Committee on Medical Isotope Production Without Highly Enriched Uranium. "Medical Isotope Production Without Highly Enriched Uranium". In: Washingtion (DC): National Academies Press (US), 2009. Chap. Appendix D: Alternative Molybdenum-99 Production Processes. URL: https://www.ncbi.nlm.nih.gov/books/NBK215133/.

[24] A.D. Roberts et al. "Measured bremsstrahlung photonuclear production of 99Mo (99mTc) with 34MeV to 1.7GeV electrons". In: *Applied Radiation and Isotopes* 96 (2015), pp. 122–128. ISSN: 0969-8043. DOI: https://doi.org/10.1016/j.apradiso.2014.11.008. URL: https://www.sciencedirect.com/science/article/pii/S0969804314003935.

[25] Arjan Koning, Stephane Hilaire, and Stephane Goriely. "TALYS: modeling of nuclear reactions". In: *The European Physical Journal A* 59.6 (June 2023), p. 131. ISSN: 1434-601X. DOI: 10.1140/epja/s10050-023-01034-3. URL: https://doi.org/10.1140/epja/s10050-023-01034-3.

[26] Guttormsen, M. et al. "Gamma-widths, lifetimes and fluctuations in the nuclear quasi-continuum". In: *EPJ Web Conf.* 178 (2018), p. 06001. DOI: 10.1051/epjconf/201817806001. URL: https://doi.org/10.1051/epjconf/201817806001.

[27] A.J. Koning, S. Hilaire, and S. Goriely. "Global and local level density models". In: *Nuclear Physics A* 810.1 (2008), pp. 13–76. ISSN: 0375-9474. DOI: https://doi.org/10.1016/j.nuclphysa.2008.06.005. URL: https://www.sciencedirect.com/science/article/pii/S0375947408005903.

[28] H. A. Bethe. "Nuclear Physics B. Nuclear Dynamics, Theoretical". In: *Rev. Mod. Phys.* 9 (2 Apr. 1937), pp. 69–244. DOI: 10.1103/RevModPhys.9.69. URL: https://link.aps.org/doi/10.1103/RevModPhys.9.69.

[29] A. G. W. Cameron. "NUCLEAR LEVEL SPACINGS". In: *Canadian Journal of Physics* 36.8 (1958), pp. 1040–1057. DOI: 10.1139/p58-112. eprint: https://doi.org/10.1139/p58-112. URL: https://doi.org/10.1139/p58-112.

[30] Edward V. Lee and James J. Griffin. "Even-Odd Effects in Precompound Emission". In: *Phys. Rev. C* 5 (5 May 1972), pp. 1713–1717. DOI: 10.1103/PhysRevC.5.1713. URL: https://link.aps.org/doi/10.1103/PhysRevC.5.1713.

[31] Torleif Ericson. "The statistical model and nuclear level densities". In: *Advances in Physics* 9.36 (1960), pp. 425–511. DOI: 10.1080/00018736000101239. eprint: https://doi.org/10.1080/00018736000101239. URL: https://doi.org/10.1080/00018736000101239.

[32] A. V. Ignatyuk, G. N. Smirenkin, and A. S. Tishin. "Phenomenological description of energy dependence of the level density parameter". In: *Yadernaya Fizika* 21.3 (1975), pp. 485–490. URL: http://inis.iaea.org/search/search.aspx?orig_q=RN:06208426.

[33] S. Goriely. "A new nuclear level density formula including shell and pairing correction in the light of a microscopic model calculation". In: *Nuclear Physics A* 605.1 (1996), pp. 28–60. ISSN: 0375-9474. DOI: https://doi.org/10.1016/0375-9474(96)00162-5. URL: https://www.sciencedirect.com/science/article/pii/0375947496001625.

[34] S. F. Mughabghab and C. Dunford. "Nuclear Level Density and the Effective Nucleon Mass". In: *Phys. Rev. Lett.* 81 (19 Nov. 1998), pp. 4083–4086. DOI: 10.1103/PhysRevLett.81.4083. URL: https://link.aps.org/doi/10.1103/PhysRevLett.81.4083.

[35] A. Gilbert and A. G. W. Cameron. "A COMPOSITE NUCLEAR-LEVEL DENSITY FORMULA WITH SHELL CORRECTIONS". In: *Canadian Journal of Physics* 43.8 (1965), pp. 1446–1496. DOI: 10.1139/p65-139. eprint: https://doi.org/10.1139/p65-139. URL: https://doi.org/10.1139/p65-139.

[36] W. Dilg et al. "Level density parameters for the back-shifted fermi gas model in the mass range 40 ¡ A ¡ 250". In: *Nuclear Physics A* 217.2 (1973), pp. 269–298. ISSN: 0375-9474. DOI: https://doi.org/10.1016/0375-9474(73)90196-6. URL: https://www.sciencedirect.com/science/article/pii/0375947473901966.

[37] M.K. Grossjean and H. Feldmeier. "Level density of a Fermi gas with pairing interactions". In: *Nuclear Physics A* 444.1 (1985), pp. 113–132. ISSN: 0375-9474. DOI: https://doi.org/10.1016/0375-9474(85)90294-5. URL: https://www.sciencedirect.com/science/article/pii/0375947485902945.

[38] P. Demetriou and S. Goriely. "Microscopic nuclear level densities for practical applications". In: *Nuclear Physics A* 695.1 (2001), pp. 95–108. ISSN: 0375-9474. DOI: https://doi.org/10.1016/S0375-9474(01)01095-8. URL: https://www.sciencedirect.com/science/article/pii/S0375947401010958.

[39] A V Ignatyuk, K K Istekov, and G N Smirenkin. "Role of collective effects in the systematics of nuclear level densities". In: *Sov. J. Nucl. Phys. (Engl. Transl.); (United States)* 29:4 (Apr. 1979). URL: https://www.osti.gov/biblio/5770504.

[40] A. V. Ignatyuk et al. "Density of discrete levels in ^{116}Sn". In: *Phys. Rev. C* 47 (4 Apr. 1993), pp. 1504–1513. DOI: 10.1103/PhysRevC.47.1504. URL: https://link.aps.org/doi/10.1103/PhysRevC.47.1504.

[41] L G Moretto et al. "Experimental First Order Pairing Phase Transition in Atomic Nuclei". In: *Journal of Physics: Conference Series* 580.1 (Feb. 2015), p. 012048. DOI: 10.1088/1742-6596/580/1/012048. URL: https://dx.doi.org/10.1088/1742-6596/580/1/012048.

[42] S. GORIELY, F. TONDEUR, and J.M. PEARSON. "A HARTREE–FOCK NUCLEAR MASS TABLE". In: *Atomic Data and Nuclear Data Tables* 77.2 (2001), pp. 311–381. ISSN: 0092-640X. DOI: https://doi.org/10.1006/adnd.2000.0857. URL: https://www.sciencedirect.com/science/article/pii/S0092640X0090857X.

[43] F. Tondeur et al. "Towards a Hartree-Fock mass formula". In: *Phys. Rev. C* 62 (2 July 2000), p. 024308. DOI: 10.1103/PhysRevC.62.024308. URL: https://link.aps.org/doi/10.1103/PhysRevC.62.024308.

[44] S. Goriely, S. Hilaire, and A. J. Koning. "Improved microscopic nuclear level densities within the Hartree-Fock-Bogoliubov plus combinatorial method". In: *Phys. Rev. C* 78 (6 Dec. 2008), p. 064307. DOI: 10.1103/PhysRevC.78.064307. URL: https://link.aps.org/doi/10.1103/PhysRevC.78.064307.

[45] S. Goriely et al. "First Gogny-Hartree-Fock-Bogoliubov Nuclear Mass Model". In: *Phys. Rev. Lett.* 102 (24 June 2009), p. 242501. DOI: 10.1103/PhysRevLett.102.242501. URL: https://link.aps.org/doi/10.1103/PhysRevLett.102.242501.

[46] S. Hilaire et al. "Temperature-dependent combinatorial level densities with the D1M Gogny force". In: *Phys. Rev. C* 86 (6 Dec. 2012), p. 064317. DOI: 10.1103/PhysRevC.86.064317. URL: https://link.aps.org/doi/10.1103/PhysRevC.86.064317.

[47] J. Kopecky and M. Uhl. "Test of gamma-ray strength functions in nuclear reaction model calculations". In: *Phys. Rev. C* 41 (5 May 1990), pp. 1941–1955. DOI: 10.1103/PhysRevC.41.1941. URL: https://link.aps.org/doi/10.1103/PhysRevC.41.1941.

[48] G. A. Bartholomew et al. "Gamma-Ray Strength Functions". In: *Advances in Nuclear Physics: Volume 7*. Ed. by Michel Baranger and Erich Vogt. Boston, MA: Springer US, 1973, pp. 229–324. ISBN: 978-1-4615-9044-6. DOI: 10.1007/978-1-4615-9044-6_4. URL: https://doi.org/10.1007/978-1-4615-9044-6_4.

[49] Walter Hauser and Herman Feshbach. "The Inelastic Scattering of Neutrons". In: *Phys. Rev.* 87 (2 July 1952), pp. 366–373. DOI: 10.1103/PhysRev.87.366. URL: https://link.aps.org/doi/10.1103/PhysRev.87.366.

[50] M. Guttormsen et al. *Is the generalized Brink-Axel hypothesis valid?* 2017. arXiv: 1701.07317 [nucl-ex].

[51] M. Guttormsen et al. "Validity of the Generalized Brink-Axel Hypothesis in ^{238}Np". In: *Phys. Rev. Lett.* 116 (1 Jan. 2016), p. 012502. DOI: 10.1103/PhysRevLett.116.012502. URL: https://link.aps.org/doi/10.1103/PhysRevLett.116.012502.

[52] M. Markova et al. "Comprehensive Test of the Brink-Axel Hypothesis in the Energy Region of the Pygmy Dipole Resonance". In: *Phys. Rev. Lett.* 127 (18 Oct. 2021), p. 182501. DOI: 10.1103/PhysRevLett.127.182501. URL: https://link.aps.org/doi/10.1103/PhysRevLett.127.182501.

[53] L. Crespo Campo et al. "Test of the generalized Brink-Axel hypothesis in ^{64,65}Ni". In: *Phys. Rev. C* 98 (5 Nov. 2018), p. 054303. DOI: 10.1103/PhysRevC.98.054303. URL: https://link.aps.org/doi/10.1103/PhysRevC.98.054303.

[54] D.M. Brink. "Individual particle and collective aspects of the nuclear photoeffect". In: *Nuclear Physics* 4 (1957), pp. 215–220. ISSN: 0029-5582. DOI: https://doi.org/10.1016/0029-5582(87)90021-6. URL: https://www.sciencedirect.com/science/article/pii/0029558287900216.

[55] Peter Axel. "Electric Dipole Ground-State Transition Width Strength Function and 7-Mev Photon Interactions". In: *Phys. Rev.* 126 (2 Apr. 1962), pp. 671–683. DOI: 10.1103/PhysRev.126.671. URL: https://link.aps.org/doi/10.1103/PhysRev.126.671.

[56] B. L. Berman and S. C. Fultz. "Measurements of the giant dipole resonance with monoenergetic photons". In: *Rev. Mod. Phys.* 47 (3 July 1975), pp. 713–761. DOI: 10.1103/RevModPhys.47.713. URL: https://link.aps.org/doi/10.1103/RevModPhys.47.713.

[57] J. Kopecky, M. Uhl, and R. E. Chrien. "Radiative strength in the compound nucleus ^{157}Gd". In: *Phys. Rev. C* 47 (1 Jan. 1993), pp. 312–322. DOI: 10.1103/PhysRevC.47.312. URL: https://link.aps.org/doi/10.1103/PhysRevC.47.312.

[58] S. Goriely. "Radiative neutron captures by neutron-rich nuclei and the r-process nucleosynthesis". In: *Physics Letters B* 436.1 (1998), pp. 10–18. ISSN: 0370-2693. DOI: https://doi.org/10.1016/S0370-2693(98)00907-1. URL: https://www.sciencedirect.com/science/article/pii/S0370269398009071.

[59] J. A. Maruhn et al. "Dipole giant resonances in deformed heavy nuclei". In: *Phys. Rev. C* 71 (6 June 2005), p. 064328. DOI: 10.1103/PhysRevC.71.064328. URL: https://link.aps.org/doi/10.1103/PhysRevC.71.064328.

[60] D. Savran, T. Aumann, and A. Zilges. "Experimental studies of the Pygmy Dipole Resonance". In: *Progress in Particle and Nuclear Physics* 70 (2013), pp. 210–245. ISSN: 0146-6410. DOI: https://doi.org/10.1016/j.ppnp.2013.02.003. URL: https://www.sciencedirect.com/science/article/pii/S0146641013000057.

[61] S. Goriely and E. Khan. "Large-scale QRPA calculation of E1-strength and its impact on the neutron capture cross section". In: *Nuclear Physics A* 706.1 (2002), pp. 217–232. ISSN: 0375-9474. DOI: https://doi.org/10.1016/S0375-9474(02)00860-6. URL: https://www.sciencedirect.com/science/article/pii/S0375947402008606.

[62] S Goriely, E Khan, and M Samyn. "Microscopic HFB + QRPA predictions of dipole strength for astrophysics applications". In: *Nuclear Physics A* 739.3 (2004), pp. 331–352. ISSN: 0375-9474. DOI: https://doi.org/10.1016/j.nuclphysa.2004.04.105. URL: https://www.sciencedirect.com/science/article/pii/S0375947404006578.

[63] M. R. Harston and J. F. Chemin. "Mechanisms of nuclear excitation in plasmas". In: *Phys. Rev. C* 59 (5 May 1999), pp. 2462–2473. DOI: 10.1103/PhysRevC.59.2462. URL: https://link.aps.org/doi/10.1103/PhysRevC.59.2462.

[64] Masato Morita. "Nuclear Excitation by Electron Transition and Its Application to Uranium 235 Separation". In: *Progress of Theoretical Physics* 49.5 (May 1973), pp. 1574–1586. ISSN: 0033-068X. DOI: 10.1143/PTP.49.1574. eprint: https://academic.oup.com/ptp/article-pdf/49/5/1574/5411690/49-5-1574.pdf. URL: https://doi.org/10.1143/PTP.49.1574.

[65] Yasukazu Izawa and Chiyoe Yamanaka. "Production of 235Um by nuclear excitation by electron transition in a laser produced uranium plasma". In: *Physics Letters B* 88.1 (1979), pp. 59–61. ISSN: 0370-2693. DOI: https://doi.org/10.1016/0370-2693(79)90113-8. URL: https://www.sciencedirect.com/science/article/pii/0370269379901138.

[66] RV Arutyunyan et al. "Excitation cross-section for 235U isomer in plasma created by beam of electrons". In: *Sov. J. Nucl. Phys.* 53 (1991), p. 23.

[67] JA Bounds and P Dyer. "Search for nuclear excitation by laser-driven electron motion". In: *Physical Review C* 46.3 (1992), p. 852.

[68] M.R. Harston. "Analysis of probabilities for nuclear excitation by near-resonant electronic transitions". In: *Nuclear Physics A* 690.4 (2001), pp. 447–455. ISSN: 0375-9474. DOI: https://doi.org/10.1016/S0375-9474(01)00358-X. URL: https://www.sciencedirect.com/science/article/pii/S037594740100358X.

[69] E. Browne and J. K. Tuli. In: *Nucl. Data Sheets 122, 205* (2014).

[70] V I Gol'danskii and V A Namiot. "Excitation of nuclear isomeric levels in a hot plasma by inverse internal electron conversion". In: *Sov. J. Nucl. Phys. (Engl. Transl.); (United States)* 33:2 (Feb. 1981). URL: https://www.osti.gov/biblio/5971212.

[71] N. Cue, J.-C. Poizat, and J. Remillieux. "Exciting the Nucleus by Target Electron Capture into Atomic Orbitals". In: *Europhysics Letters* 8.1 (Jan. 1989), p. 19. DOI: 10.1209/0295-5075/8/1/004. URL: https://dx.doi.org/10.1209/0295-5075/8/1/004.

[72] C. J. Chiara et al. "Isomer depletion as experimental evidence of nuclear excitation by electron capture". In: *Nature* 554.7691 (Feb. 2018), pp. 216–218. ISSN: 1476-4687. DOI: 10.1038/nature25483. URL: https://doi.org/10.1038/nature25483.

[73] Song Guo et al. "Possible overestimation of isomer depletion due to contamination". In: *Nature* 594.7861 (June 2021), E1–E2. ISSN: 1476-4687. DOI: 10.1038/s41586-021-03333-5. URL: https://doi.org/10.1038/s41586-021-03333-5.

[74] T William Donnelly and JD Walecka. "Electron scattering and nuclear structure". In: *Annual Review of Nuclear Science* 25.1 (1975), pp. 329–405.

[75] WC Barber. "Inelastic electron scattering". In: *Annual Review of Nuclear Science* 12.1 (1962), pp. 1–42.

[76] G. Gosselin and P. Morel. "Enhanced nuclear level decay in hot dense plasmas". In: *Phys. Rev. C* 70 (6 Dec. 2004), p. 064603. DOI: 10.1103/PhysRevC.70.064603. URL: https://link.aps.org/doi/10.1103/PhysRevC.70.064603.

[77] G. Gosselin, V. Méot, and P. Morel. "Modified nuclear level lifetime in hot dense plasmas". In: *Phys. Rev. C* 76 (4 Oct. 2007), p. 044611. DOI: 10.1103/PhysRevC.76.044611. URL: https://link.aps.org/doi/10.1103/PhysRevC.76.044611.

[78] Ch J Cerjan et al. "Dynamic high energy density plasma environments at the National Ignition Facility for nuclear science research". In: *Journal of Physics G: Nuclear and Particle Physics* 45.3 (Feb. 2018), p. 033003. DOI: 10.1088/1361-6471/aa8693. URL: https://dx.doi.org/10.1088/1361-6471/aa8693.

[79] T. Døssing and E. Vigezzi. "Cooling and diffusion in the -decay of rotating nuclei". In: *Nuclear Physics A* 587.1 (1995), pp. 13–35. ISSN: 0375-9474. DOI: https://doi.org/10.1016/0375-9474(94)00813-3. URL: https://www.sciencedirect.com/science/article/pii/0375947494008133.

[80] Frank Träger. *Springer Handbook of Lasers and Optics*. Springer, 2007.

[81] E. Esarey, C. B. Schroeder, and W. P. Leemans. "Physics of laser-driven plasma-based electron accelerators". In: *Rev. Mod. Phys.* 81 (3 Aug. 2009), pp. 1229–1285. DOI: 10.1103/RevModPhys.81.1229. URL: https://link.aps.org/doi/10.1103/RevModPhys.81.1229.

[82] WILLIAM KRUER. *Physics of laser plasma interactions*. CRC Press, 2019.

[83] Richard Fitzpatrick. *Plasma Physics: An Introduction*. CRC Press, 2022.

[84] C. B. Schroeder and E. Esarey. "Relativistic warm plasma theory of nonlinear laser-driven electron plasma waves". In: *Phys. Rev. E* 81 (5 May 2010), p. 056403. DOI: 10.1103/PhysRevE.81.056403. URL: https://link.aps.org/doi/10.1103/PhysRevE.81.056403.

[85] T. Tajima and J. M. Dawson. "Laser Electron Accelerator". In: *Phys. Rev. Lett.* 43 (4 July 1979), pp. 267–270. DOI: 10.1103/PhysRevLett.43.267. URL: https://link.aps.org/doi/10.1103/PhysRevLett.43.267.

[86] Eiji Tanabe et al. "Breakdown in high-gradient accelerator cavities". In: *Proceedings of the 1984 Linear Accelerator Conference, Seeheim/Darmstadt, West Germany*. 1984, p. 403.

[87] Walter Wuensch. "A Review of Vacuum Breakdown in High-Gradient Accelerators". In: *2018 28th International Symposium on Discharges and Electrical Insulation in Vacuum (ISDEIV)*. Vol. 2. 2018, pp. 747–752. DOI: 10.1109/DEIV.2018.8537005.

[88] John M. Dawson. "Nonlinear Electron Oscillations in a Cold Plasma". In: *Phys. Rev.* 113 (2 Jan. 1959), pp. 383–387. DOI: 10.1103/PhysRev.113.383. URL: https://link.aps.org/doi/10.1103/PhysRev.113.383.

[89] P. Sprangle et al. "Laser wakefield acceleration and relativistic optical guiding". In: *Applied Physics Letters* 53.22 (Nov. 1988), pp. 2146–2148. ISSN: 0003-6951. DOI: 10.1063/1.100300. eprint: https://pubs.aip.org/aip/apl/article-pdf/53/22/2146/18468511/2146_1_online.pdf. URL: https://doi.org/10.1063/1.100300.

[90] E. Esarey et al. "The laser wakefield accelerator". In: *Comments on Plasma Physics and Controlled Fusion* 12.4 (1989), pp. 191–204. ISSN: 0374-2806. URL: http://inis.iaea.org/search/search.aspx?orig_q=RN:21090425.

[91] WKH Panofsky and WA Wenzel. "Some considerations concerning the transverse deflection of charged particles in radio-frequency fields". In: *Review of Scientific Instruments* 27.11 (1956), pp. 967–967.

[92] Rhon Keinigs and Michael E Jones. "Two-dimensional dynamics of the plasma wakefield accelerator". In: *The Physics of fluids* 30.1 (1987), pp. 252–263.

[93] P. Sprangle, E. Esarey, and A. Ting. "Nonlinear interaction of intense laser pulses in plasmas". In: *Phys. Rev. A* 41 (8 Apr. 1990), pp. 4463–4469. DOI: 10.1103/PhysRevA.41.4463. URL: https://link.aps.org/doi/10.1103/PhysRevA.41.4463.

[94] P. Sprangle, E. Esarey, and A. Ting. "Nonlinear theory of intense laser-plasma interactions". In: *Phys. Rev. Lett.* 64 (17 Apr. 1990), pp. 2011–2014. DOI: 10.1103/PhysRevLett.64.2011. URL: https://link.aps.org/doi/10.1103/PhysRevLett.64.2011.

[95] John R. de Laeter et al. "Atomic weights of the elements. Review 2000 (IUPAC Technical Report)". In: *Pure and Applied Chemistry* 75.6 (2003), pp. 683–800. DOI: doi:10.1351/pac200375060683. URL: https://doi.org/10.1351/pac200375060683.

[96] Brookhaven National Laboratory National Nuclear Data Center. *NuDat (Nuclear Structure and Decay Data)*. Mar. 2008.

[97] Balraj Singh. In: *Nucl. Data Sheets 105, 223* (2005).

[98] Hai-En Tsai et al. "Control of quasi-monoenergetic electron beams from laser-plasma accelerators with adjustable shock density profile". In: *Physics of Plasmas* 25.4 (Apr. 2018), p. 043107. ISSN: 1070-664X. DOI: 10.1063/1.5023694. eprint: https://pubs.aip.org/aip/pop/article-pdf/doi/10.1063/1.5023694/13778085/043107_1_online.pdf. URL: https://doi.org/10.1063/1.5023694.

[99] Qiang Chen et al. "Development of the MeV Thomson-scattered gamma ray source using laser plasma accelerators at the BELLA Center". In: *Compact Radiation Sources from EUV to Gamma-rays: Development and Applications*. Ed. by Carmen S. Menoni and Jaroslav Nejdl. Vol. PC12582. International Society for Optics and Photonics. SPIE, 2023, PC125820C. DOI: 10.1117/12.2665755. URL: https://doi.org/10.1117/12.2665755.

[100] P. Elleaume, O. Chubar, and J. Chavanne. "Computing 3D magnetic fields from insertion devices". In: *Proceedings of the 1997 Particle Accelerator Conference (Cat. No.97CH36167)*. Vol. 3. 1997, 3509–3511 vol.3. DOI: 10.1109/PAC.1997.753258.

[101] C. Ahdida et al. "New Capabilities of the FLUKA Multi-Purpose Code". In: *Frontiers in Physics* 9 (2022). ISSN: 2296-424X. DOI: 10.3389/fphy.2021.788253. URL: https://www.frontiersin.org/articles/10.3389/fphy.2021.788253.

[102] Giuseppe Battistoni et al. "Overview of the FLUKA code". In: *Annals of Nuclear Energy* 82 (2015). Joint International Conference on Supercomputing in Nuclear Applications and Monte Carlo 2013, SNA + MC 2013. Pluri- and Trans-disciplinarity, Towards New Modeling and Numerical Simulation Paradigms, pp. 10–18. ISSN: 0306-4549. DOI: https://doi.org/10.1016/j.anucene.2014.11.007. URL: https://www.sciencedirect.com/science/article/pii/S0306454914005878.

[103] Vasilis Vlachoudis. "Flair: A powerful but user friendly graphical interface for FLUKA". In: (2009), pp. 790–800. URL: https://cds.cern.ch/record/2749540.

[104] A. J. Koning, S. Hilaire, and M. C. Duijvestijn. "TALYS: Comprehensive Nuclear Reaction Modeling". In: *AIP Conference Proceedings* 769.1 (May 2005), pp. 1154–1159. ISSN: 0094-243X. DOI: 10.1063/1.1945212. eprint: https://pubs.aip.org/aip/acp/article-pdf/769/1/1154/12138013/1154_1_online.pdf. URL: https://doi.org/10.1063/1.1945212.